Computational and Experimental Modeling of the Bioheat Transfer Process of Perfusion in Tissue Applied to Burn Wounds

Abdusalam Imhmed K. Al-Khwaji

Dissertation submitted to the faculty of the Virginia Polytechnic Institute and State University in partial fulfillment of the requirements for the degree of

Doctor of Philosophy
In
Mechanical Engineering

Thomas E. Diller, Chair
Brian Vick
J. Wally Grant
Scott T. Huxtable
Marissa Nichole Rylander

11th of April 2013
Blacksburg, Virginia

Keywords: burn severity, blood perfusion, thermal resistance, thermal measurement, parameter estimation, inflammation

Computational and Experimental Modeling of the Bioheat Transfer Process of Perfusion in Tissue Applied to Burn Wounds

Abdusalam Imhmed K. Al-Khwaji

ABSTRACT

A new mathematical model has been developed along with a new parameter estimation routine using surface temperature and heat flux measurements to estimate blood perfusion and thermal resistance in living tissue. Dynamic thermal measurements collected at the surface of the sensor before and after imposing a dynamic thermal cooling event are used with the model to estimate the blood perfusion, thermal resistance and core temperature. The Green's function based analytical solution does not require calculation of the whole tissue temperature distribution, which was not the case for the previous models. The result from the new model was proved to have better and more consistent results than previous models. The new model was validated to solve one of the unsolved biomedical problems which is the ability of detecting burn severity. The method was tested with a phantom perfusion system. The results matched known blood perfusion and thermal resistance values. The method was also tested with burns on animal models. Inflammation effects associated with the burns were studied using a newly developed term called the Burn Factor. This correlated with the severity of imposed burns.

This work consists of three journal papers. The first paper introduces the mathematical model and its validation with finite-difference solutions. The second paper validates the physical aspects of the usage of the model with thermal measurement in detecting simulated burned layers and the associated perfusion. The third paper demonstrates the ability of the model to use thermal measurements to detect different burn severity of an animal model and to study the healing process.

This work received support from Libyan-North American Scholarship.

Acknowledgment

I would like to express my respects and acknowledgments to

- My research advisor Dr. Tom Diller for his support and patience
- My dissertation committee member: Dr. Brian Vick, Dr. Wally Grant, Dr. Scott T. Huxtable, Dr. Marissa Nichole Rylander
- Joe Molnar and Stan Gordon at Wake Forest School of Medicine for their support in providing us with the pig experimental animal model.
- Support of Wake Forest University & the Translational Science Institute with the animal experiments
- Support of Omar Almukthar University, and the Libyan-North America Scholarship program (CBIE)
- All Faculty and staff members of the ME Department at Virginia Tech
- To my family and friends

Table of contents

List of Figures

List of Tables

Chapter 1 – Introduction

Computational modeling of the bioheat process of perfusion in tissue has great medical significance for quantifying many tissue disorders. Any abnormal perfusion indicates disruption along the path from which heat, nutrition and oxygen are carried. Possible disruptions could be inflammation, cancer or a burn. A perfusion and thermal resistance probe has been developed to measure temperature and heat flux to detect any disorder in the process of transferring heat to the surface by perfusion.

Detecting burn severity is the main application investigated. Burns are one of the largest daily risks which could result from any contact with any medium with higher temperature or harming chemical material. To model the burn mathematically, perfusion and thermal resistance express tissue condition in response to any change in the environment. Providing a thermal event provides increased information about the perfusion in the tissue. Perfusion in a burned tissue is not the same as in normal tissue, which makes thermal measurements useful in detecting burns. The time of burn duration and the strength of either the chemical concentration or temperature dictate the burn severities. Burns have being classified based on the depth of damages. It is important to be able to classify the burn immediately during the emergency. That will avoid needless surgery or extra hospitalization costs.

Thermal measurements were collected using a combined temperature-heat flux sensor. A new parameter estimation routine was developed that insures consistency and repeatability of the estimated parameters. Initial temperatures were used from the steady-state solution and they were matched with steady-state heat flux measurements to estimate the core temperature. There was no thermal model has been published before this work which search for burn detection, the previous work was developed to detect perfusion. The new model uses the right temperature distribution throughout the tissue and uses only surface temperature-heat flux calculation. Moreover, reducing the dimension of the problem to 1D was proved which helps to optimize the searching time.

This dissertation consists of three published papers [1.1-1.3]. The first paper introduces the new mathematical model and demonstrates that by reducing the complexity of the problem from 2D to 1D does not cost the accuracy of the results [1.4-1.6]. The second was to prove the repeatability and accuracy of the model in representing the burnt tissue using phantom tissue. The third paper demonstrates the process of estimated burn severity using the model along with thermal measurements on two pigs.

A parameter estimation routine was developed in this thesis, which works efficiently to search for three optimal parameters, blood perfusion, thermal resistance and core temperature. The Green's function technique is an efficient for the transient developed step changes in both heat flux and temperature measurements. The time required to get the solution is very optimal because the Green's function analytical solutions does not require the full calculation of the tissue temperature distribution. The Green's function solution which is developed in this research work needs just surface calculation and estimation, instead of estimation the optimal perfusion and thermal resistance of all finite difference nodes.

In the second paper, the validation of model in predicting different simulating burn severity was proved. The burn was modeled as a thermal resistance while thermal capacitance was neglected. The model still gives an accurate estimation of the burn depth without thermal capacitance effect. The tests were collected from phantom tissue using different plastic thicknesses. Results from simulated burn depth demonstrate the ability of the thermal measurement in detecting each thickness was used and the corresponding blood perfusion.

The third paper uses data from pig experiments to evaluate the ability of the thermal measurement to detect third degree burns. Burn factor was developed in this research work to monitor the healing process from the two estimated parameters, perfusion and thermal resistance. Burn factor reflect very clearly any inflammation processes related to a burn wound. Three appendixes were created to describe codes, instrumentation and parameters during this work. The experimental result was analyzed using the statistical method called the T-student methods.

INTRODUCTORY REFERENCES

[1.1] Alkhwaji, Abdusalam., Vick, B., and Diller, T., "New mathematical model to estimate tissue blood perfusion, thermal contact resistance and core temperature," *Journal of Biomechanical Engineering*, Vol.134, 2012, 081004, pp. 1-8.

[1.2] Abdusalam Alkhwaji, Brian Vick, Tom Diller, "Modeling and Estimating Simulated Burn Depth Using the Perfusion and Thermal Resistance Probe," Journal of Medical Device, under review.

[1.3] Abdusalam Alkhwaji, Brian Vick, Tom Diller, "Monitoring and quantifying burn wounds on pig skin using thermal measurements," In submission process.

[1.4] Ricketts, P. L., Mudaliar, A. V., Ellis, B. E., Pullins, C. A., Meyers, L. A., Lanz, O. I., Scott, E. P., and Diller, T. E., 2008, "Non-invasive blood perfusion measurements using a combined temperature and heat flux probe," International Journal of Heat and Mass Transfer, **51**, pp. 5740-5748.

[1.5] Mudaliar, A. V., Ellis, B. E., Ricketts, P. L., Lanz, O. I., Scott, E. P., and Diller, T. E., 2008, "A phantom tissue system for the calibration of perfusion measurements," ASME Journal of Biomechanical Engineering, **130**, 051002.

[1.6] Mudalier, A.V., Ellis, B. E., Ricketts, P. L., Lanz, O. I., Lee, C. Y, Diller, T. E., and Scott, E. P., 2008, "Noninvasive Blood Perfusion Measurements in an Isolated Rat Liver and an Anesthetized Rat Kidney," ASME Journal of Biomechanical engineering, **130**, 061013.

Chapter 2

New Mathematical Model to Estimate Tissue Blood Perfusion, Thermal Contact Resistance and Core Temperature

This chapter comprises sections from the Biomechanical Engineering Journal Paper, Vol.134, 2012, 081004, pp. 1-8. The full-length is reprinted here with permission of Beth Darchi, ASME 2013.

2.1 Abstract

Analytical solutions were developed based on the Green's function method to describe heat transfer in tissue including the effects of blood perfusion. These one-dimensional transient solutions were used with a simple parameter estimation technique and experimental measurements of temperature and heat flux at the surface of simulated tissue. It was demonstrated how such surface measurements can be used during step changes in the surface thermal conditions to estimate the value of three important parameters: blood perfusion (w_b), thermal contact resistance (R''), and core temperature of the tissue (T_{core}). The new models were tested against finite-difference solutions of thermal events on the surface to show the validity of the analytical solution. Simulated data was used to demonstrate the response of the model in predicting optimal parameters from noisy temperature and heat flux measurements. Finally, the analytical model and simple parameter estimation routine were used with actual experimental data from perfusion in phantom tissue. The model was shown to provide a very good match with the data curves. This demonstrated the first time that all three of these important parameters (w_b, R'', and T_{core}) have simultaneously been estimated from a single set of thermal measurements at the surface of tissue.

Keywords: heat flux sensor; parameter estimation; convective cooling

2.2 INTRODUCTION

Heat transfer in the human body can be used to monitor important biological processes. One example is to use the thermal energy transported by fluids as a tracer for blood perfusion in the tissue. Perfusion is the volumetric flow rate of the blood into a tissue, which delivers oxygen and nutrients to the cells while rejecting wastes. The knowledge of local blood perfusion is important in many medical situations, such as, healing of skin grafts, the extent of burn damage, and microcirculation problems in diabetes.

Previous research has demonstrated that thermal measurements of the temperature and heat flux during a thermal event at the surface of tissue can be used to measure the local blood perfusion. The goal of the present research is to develop a practical system for clinical applications based on this concept. A new analytical model is presented to simplify the data processing and provide the correct initial conditions for the bioheat equation. In addition, a robust parameter estimation method is developed to simultaneously solve for local core temperature, thermal contact resistance and blood perfusion values.

2.3 BACKGROUND ON PERFUSION MEASUREMENT

Blood perfusion measurements can be generally categorized in two groups (1) for in-depth applications or (2) for surface applications. The techniques are very different and mutually exclusive.

In-Depth Measurement Methods

Several scanning methods can be used to determine blood perfusion from the resulting two-dimensional images. Positron Emission Tomography (PET) is a molecular imaging technique that uses a radioactive tracer injected into the blood stream. Activity curves are extracted from a dynamic scan and perfusion is determined from an arterial input function [2.1]. A closely related method is Single-Photon Emission Computer Tomography (SPECT). The tracer emits gamma rays with longer decay times [2.2]. Magnetic Resonance Imaging is often used with arterial spin labeling (ASL) The ASL is a noninvasive technique to measure directly blood perfusion by using the arterial blood itself as an indicator. This is done by magnetically tagging the blood near the imaging site and then observing the changes that occur in the magnetic signal as the blood flows through the volume of tissue [2.3, 2. 4].

A thermal technique for deep-tissue perfusion measurement uses a Thermal Diffusion Probe (TDP), which measures the clearance of thermal energy from the tissue by the blood [2.5, 2.6]. The probe consists of a self-heated thermistor to measure the power required to keep the probe temperature at a set temperature offset above the tissue temperature. Perfusion values are obtained using solutions of the transient thermal energy equation.

Surface measurement methods

Laser Doppler Imaging is a non-invasive surface measurement technique that optically measures the motion of red blood cells within tissue. The output is a two-dimensional array of measurements represented in a color-coded map [2.7]. Because the motion of red blood cells is measured by the Doppler shift, there is no reliable method of calibration for perfusion. Comparison of results between different patients and interpretation of the results is difficult.

A thermal convective probe was developed for measuring perfusion near the surface of tissue [2.8]. The probe was made by combining a heat flux sensor and thermocouple. The operational key is the measured heat flux response of the tissue to an imposed thermal event at the surface provided by an array of air jets using room temperature air. The system is inherently safe because the tissue cannot be damaged by temperature excursions. There were a number of operational problems, however. The model [2.9] used a 2-D cylindrical finite-difference solution method (alternating direction implicit) of the Pennes [2.10] bioheat equation with an assumed initial linear temperature distribution in the tissue. The parameter estimation routine did not always converge. The core temperature had to be measured independently somewhere else in the body and assumed to be applicable in the tissue being measured. One of the consequences of these issues was that most of the blood perfusion values were negative, which required an offset of the results to correct. In this article, a new mathematical model and procedure is developed to address all of these problems.

2.4 EXPERIMENTAL METHODS

A combined heat flux and temperature sensor (CHFT) is the key sensor of the blood perfusion measurement system. The heat flux measurement is made using a BF-02 heat flux gage by Vatell, Corp with a direct sensitivity of 2.1 mV/(W/cm^2). This is a thermopile-based heat flux sensor that is only 0.25-mm thick. A foil thermocouple 0.0127-mm thick (RDF Corporation, Hudson, NH) is laminated to the 10 mm x 10-mm-square heat flux sensor using layers of thin

plastic (0.005-mm thick) and a heat activated epoxy. A layer of thin plastic is placed over one side of the sensor using a layer of heat activated epoxy. On the "tissue" side of the sensor, a layer of epoxy is applied, then a thin layer of plastic, another layer of epoxy, the foil thermocouple, a layer of epoxy and a thin layer of plastic. This entire layered structure is placed in a hot press at 160℃ for three hours. The result is a completely sealed sensor (0.28-mm thick) with a thin-film thermocouple next to the test material, as illustrated in Fig. 2.1. Together, it provides a direct measurement of heat flux and temperature between the tissue and sensor, as well as a water tight seal to protect the sensor from moisture present in tissue.

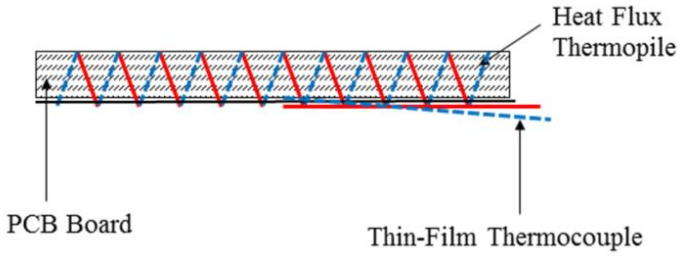

Figure 2.1 Combination Heat Flux/Temperature Sensor

The thermal event is provided by nine jets of room temperature air impinging onto the top side of the CHFT sensor. The jets are created with a compressed air supply through 0.37 mm holes. When the jets are turned on, the sudden increase in convection gives a corresponding increase in heat transfer from the tissue surface through the CHFT sensor and the thermal contact resistance, as illustrated physically in Fig. 2.2.

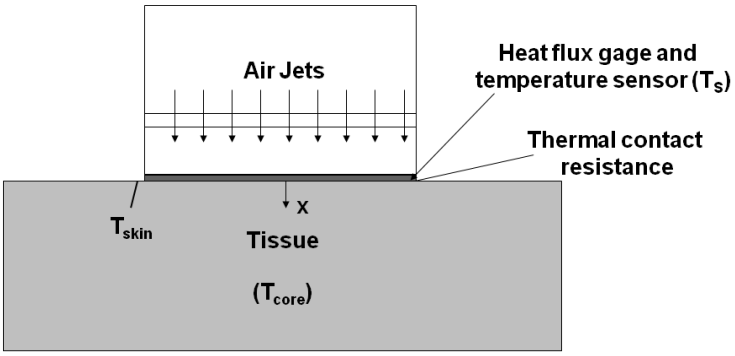

Figure 2.2 System model

The experimental temperature and heat flux values are recorded as a series of digital data points recorded with a 24-bit DAQ at one-second intervals.

Experimental measurements were obtained with the CHFT using the Phantom Tissue System of Mudalier et al. [2.9]. This test stand is designed to supply perfusate into the tissue simulator at a controlled temperature and flow rate. The bottom area of the tank stores water maintained at a constant 37 ℃ temperature (core body temperature) by a temperature controller in conjunction with a cartridge heater. The perfusate flow is provided by a small centrifugal pump from the water bath directly through a flowmeter into the porous matrix which acts as the tissue simulator.

2.5 SYSTEM MODEL

When modeling thermal events in tissue, the bioheat equation in general includes transient conduction, metabolism, and the effects of blood perfusion in tissue. Because the penetration depth over the time of the measurement (typically 1 to 2 mm) is small compared to the lateral

size of the sensor during the thermal event, it is assumed that transfer only occurs in the x direction. In addition, the effects of metabolism are neglected as small compared to the typical heat flux of over one kilowatt per square meter of the thermal event. The Pennes equation [10] therefore reduces to

$$\rho C \frac{\partial T}{\partial t} = k \frac{\partial^2 T}{\partial x^2} - (\rho C w)_b (T - T_{core}) \tag{2.1}$$

The measured sensor temperature profile is modeled as a series of steps

$$\theta_S(t) = \theta_S(0) + \sum_{n=1}^{N_{max}} \Delta\theta_{S,n} . H(t - t_n) \tag{2.2}$$

where $\theta = T - T_{core}$ and H(t) is the step function. The visual representation of the temperature input is shown in Fig. 2.3.

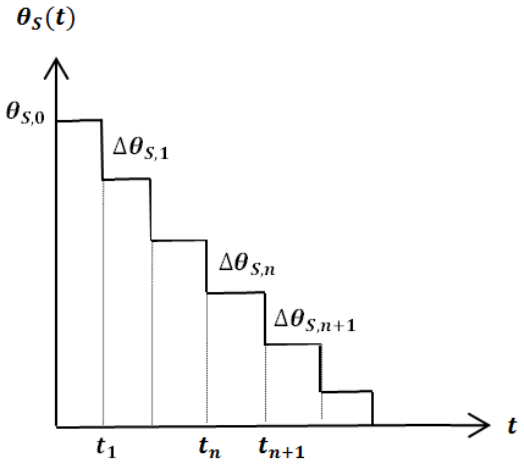

Figure 2.3 Measured temperatures from a thermal event

In terms of the variable $\theta(x,t) = T(x,t) - T_{core}$ the bio-heat equation is

$$\rho C \frac{\partial \theta}{\partial t} = k \frac{\partial^2 \theta}{\partial x^2} - (\rho C w)_b \theta \tag{2.3}$$

The tissue is assumed to be semi-infinite in extent, giving the far boundary condition as

$$\frac{\partial \theta}{\partial x}|_{x\to\infty} = 0 \tag{2.4}$$

At the surface of the tissue (x=0) the heat flux must match that through the thermal contact resistance. This with the measured surface temperature of the CHFT (θ_s) gives the second boundary condition

$$-k \frac{\partial \theta}{\partial x}|_{x=0} = \frac{1}{R''} \left(\theta_S(t) - \theta(0,t)\right) \tag{2.5}$$

Before the thermal event is initiated by turning on the air jets, the temperature distribution in the tissue is assumed to be at steady state.

$$\theta(x,0) = \theta_i(x) \tag{2.6}$$

For this case the heat flux at the surface is balanced by the warming effects of the blood perfusion in the tissue. The properties of tissue and blood are assumed to be equal with values of

k = 0.5 W/m-K, ρ = 1050 kg/m^3, and C = 3800 J/kg-K. The Pennes equation and the corresponding initial boundary conditions reduce to

$$0 = \alpha \frac{\partial^2 \theta_i}{\partial x^2} - w_b . \theta_i \tag{2.7}$$

$$-k \frac{\partial \theta_i}{\partial x}|_{x=0} = \frac{1}{R''} \left(\theta_{S,0} - \theta_i(0) \right) \tag{2.8}$$

$$\frac{\partial \theta_i}{\partial x}|_{x \to \infty} = 0 \tag{2.9}$$

where $\theta_{S,0}$ represents the steady-state temperature difference between the sensor and core before the thermal event is initiated.

2.6 MATHEMATICAL SOLUTION

The solution of equations (2.7–2.9) for the initial tissue temperature distribution is

$$\theta_i(x) = \theta_{S,0} \left[\frac{1}{1 + R'' k \sqrt{w_b/\alpha}} \right] e^{-\sqrt{w_b/\alpha}\, x} \tag{2.10}$$

The corresponding initial tissue heat flux is

$$q_i(x = 0) = -k\, \theta_{S,0} \left[\frac{\sqrt{w_b/\alpha}}{1 + R'' k \sqrt{w_b/\alpha}} \right] \tag{2.11}$$

which is defined as positive from the tissue to the sensor. Figure 2.4 illustrates the initial steady temperature distribution in the tissue from equation (2.10) for several different perfusion values. As the blood perfusion w_b increases, the temperature in the tissue becomes closer to the core temperature of 37°C and the slope at the surface increases, indicating greater heat flux.

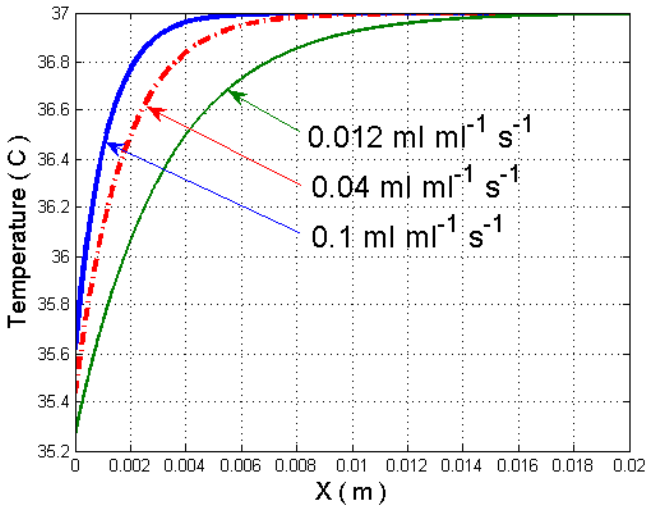

Figure 2.4 Initial steady-state temperature distributions

The second part of the solution is for the transient case, which starts with implementation of the thermal event. Using superposition, the temperature solution is sought in the form $\theta(x,t)=\theta_i(x)+\theta_T(x,t)$. When substituted into equations (2.3-2.6), the following equations are obtained governing the transient function, θ_T.

$$\frac{\partial \theta_T}{\partial t} = \alpha \frac{\partial^2 \theta_T}{\partial x^2} - w_b \theta_T \tag{2.12}$$

$$-k \frac{\partial \theta_T}{\partial x}|_{x=0} = \frac{1}{R''} \left(\theta_S(t) - \theta_{S,0} - \theta_T(0,t) \right) \tag{2.13}$$

$$\frac{\partial \theta_T}{\partial x}|_{x \to \infty} = 0 \tag{2.14}$$

$$\theta_T = 0 \quad \text{at} \quad t = t_1 \tag{2.15}$$

The transient solution (θ_T) describes the response to all step changes in temperature starting from t_1 until t_{max}**.** It is accomplished by using the Green's function method to solve the transient governing equation and its boundary and initial conditions.

The Green's function formulation of the transient state is

$$\frac{\partial G}{\partial t} = \alpha \frac{\partial^2 G}{\partial x^2} - w_b . G + \delta(x - x_0)\delta(t - t_0) \tag{2.16}$$

$$-k \frac{\partial G}{\partial x}|_{x=0} = \frac{1}{R''} (-G) \tag{2.17}$$

$$\frac{\partial G}{\partial x}|_{x \to \infty} = 0 \tag{2.18}$$

$$G = 0 \quad \text{at} \quad t \le t_0 \tag{2.19}$$

The solution in terms of the Green's function is derived according to the usual method [2.11].

$$\theta_T(x,t) = \frac{1}{\rho C} \int_{t_0=0}^{t} \frac{1}{R''} \left(\theta_S(t_0) - \theta_{S,0} \right) G(x,t|0,t_0) dt_0 \tag{2.20}$$

The solution of equations (2.16-2.19) for the required Green's function is

$$G(x,t|x_0,t_0) = G_1 - G_2 \times G_3 \tag{2.21}$$

where

$$G_1 = \frac{e^{-w_b(t-t_0)}}{\sqrt{4\pi\alpha(t-t_0)}} \left[e^{-\frac{(x-x_0)^2}{4\alpha(t-t_0)}} + e^{-\frac{(x+x_0)^2}{4\alpha(t-t_0)}} \right]$$

$$G_2 = \frac{erfc\left(\frac{(x+x_0)}{\sqrt{4\alpha(t-t_0)}} + \frac{\sqrt{\alpha(t-t_0)}}{k R''} \right)}{k R''}$$

$$G_3 = e^{\left(\frac{1}{(k R'')^2} \alpha - w_b \right)(t-t_0) + \frac{1}{kR''}(x+x_0)}$$

Evaluating at the skin surface (x = 0) gives

$$G(0,t|0,t_0) = \frac{2\, e^{-w_b(t-t_0)}}{\sqrt{4\pi\alpha(t-t_0)}} - \frac{erfc\left(\frac{\sqrt{\alpha(t-t_0)}}{k R''} \right) e^{\left(\frac{1}{(k R'')^2} \alpha - w_b \right)(t-t_0)}}{k R''} \tag{2.22}$$

The required integration in equation (2.20) was performed using Mathematica to give the needed surface temperature as a function of time.

$$\theta_T(0,t) = \frac{1}{\rho C} (I_1 + I_2) \tag{2.23}$$

where

$$I_1 = \frac{kR''\sqrt{\alpha}\left(-1 + e^{-w_b(t-t_n)} e^{\frac{\alpha(t-t_n)}{k^2R''^2}} Erfc\left[\frac{\sqrt{(t-t_n)\alpha}}{kR''}\right]\right)}{\sqrt{\alpha}(-\alpha + k^2 R''^2 w_b)}$$

$$I_2 = \frac{(kR'')^2 \sqrt{w_b}\, Erf\left[\sqrt{(t-t_n)w_b}\right]}{\sqrt{\alpha}\,(-\alpha + k^2 R''^2 w_b)}$$

The complete solution is the sum of the initial temperature plus the transient response to all of the surface temperature steps, $\theta(x,t)=\theta_i(x)+\theta_T(x,t)$. The corresponding total heat flux from equation (2.5) is

$$q_S = \frac{\theta(0,t) - \theta_S(t)}{R''} \qquad \textbf{(2.24)}$$

when defined as positive from the tissue for convenience.

During the evaluation and coding of the Green's function integral equation (2.23) into Matlab, it was difficult to evaluate the term $\{erfc(z) \cdot e^{z^2}\}$ for values of z greater than 750, which sometimes occurs for small values of thermal contact resistance R''. To solve the problem a special function was used that combined the exponential and complementary error functions

$$erfcx(z) = erfc(z) \cdot e^{z^2} \qquad \textbf{(2.25)}$$

To test the analytical solution a finite difference model was created to match the conditions imposed on the tissue. It was solved with the Crank Nicolson method [2.12] using 1500 nodes in the x direction with a spacing of Δx = 0.013 mm. The time step was Δt = 0.01 s. The finite-difference solution matches very well with the analytical solution for a wide range of blood perfusion, contact resistance, and core temperature values. An example is shown in Figure 5 and for the parameters given in Table 2.1. For representative temperature steps in time, the tissue surface (skin) temperature is shown first. The analytical and finite-difference curves are indistinguishable. The corresponding surface heat flux values are also nearly identical, as seen in the second part of Fig. 2.5.

Table 2.1 Parameters for Figure 2.5

w_b (ml ml^{-1} s^{-1})	R'' (m^2-K/W)	T_{core} (°C)
0.04	0.002	37

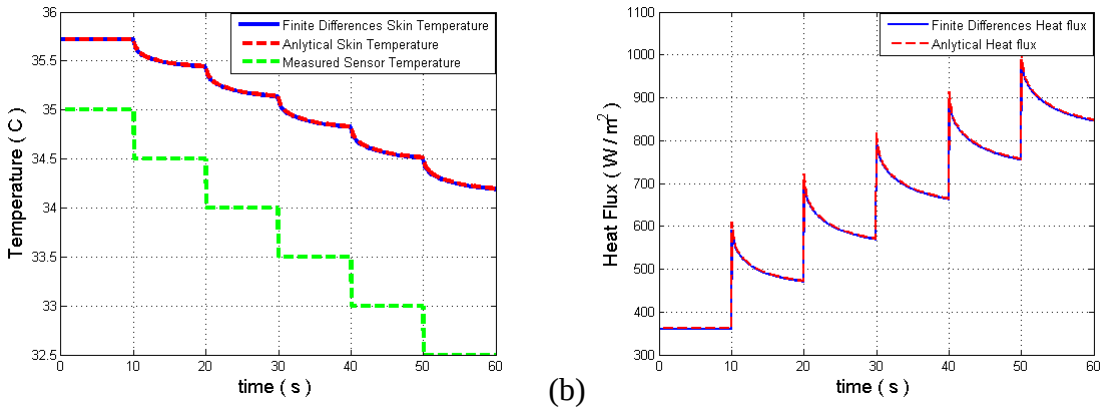

(a) (b)

Figure 2.5 Simulated temperature (a) and heat flux (b) for the analytical and finite-difference models

As a further check of the analytical model, two-dimensional effects were evaluated using an explicit finite-difference solution of the transient Pennes [2.10] bio-heat equation in

cylindrical coordinates (r and x). The radial direction was added with a uniform temperature over the sensor and an insulated boundary condition over the surrounding tissue. Seventy-two nodes were used in both the r- and x-directions with 341 time steps. Grid independence was successfully tested with larger numbers of nodes and time steps. The same initial tissue temperature distribution was used as for the one-dimensional case for direct comparison of results. Figure 2.6 shows the corresponding centerline temperature and the average heat flux for the sensing area (approximately the inner 75% of the cooled radius). The average heat flux over the sensing area is at most 3.1% higher than the one-dimensional case. The centerline heat flux exhibits almost no edge effects. The two-dimensional effects for larger sensors would be even smaller.

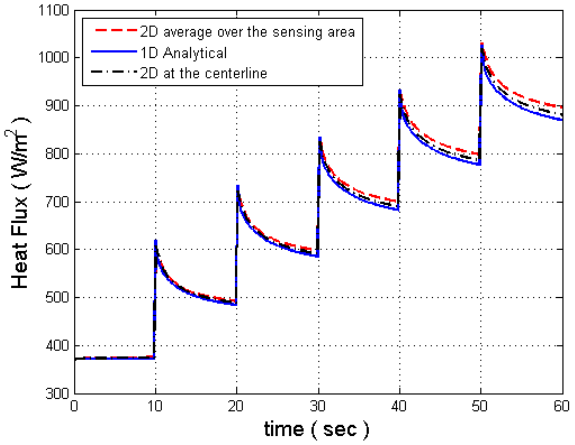

Figure 2.6 Simulated two-dimensional effects on the sensor heat flux

2.7 PARAMETER ESTIMATION

Three parameters are treated as unknown in this problem and consequently need to be determined from the experimental measurements of temperature and heat flux, the core temperature of the blood, the thermal contact resistance between the sensor and tissue surface, and the blood perfusion in the tissue. The estimated values of these parameters are all dependent on each other, which makes their estimation a highly iterative process.

The first to consider is the core temperature of the blood, T_{core}. This can be determined using equation (2.11) with steady-state data taken before the thermal event is initiated. The average heat flux and sensor temperature ($\boldsymbol{T_{S,0}}$) for this initial time period ($\boldsymbol{q_{S,0}}$) with the estimated values of R'' and w_b specify the value of T_{core}

$$\boldsymbol{T_{core} = T_{S,0} + \frac{q_{S,0}}{\left[\frac{k\sqrt{w_b/\alpha}}{1 + R'' k\sqrt{w_b/\alpha}}\right]}} \qquad \textbf{(2.26)}$$

The values of R'' and w_b are obtained during the thermal event where the heat flux and temperatures are changing dramatically. Over this time the analytical model results are matched with the experimental data. The sensor temperature is the input for the model and the heat flux is the output. The fit between the model and data is quantified using the average square root of the squared residual values

$$S = \sqrt{\frac{1}{N_{max}} \sum_{n=1}^{Nmax} r_n^2} \tag{2.27}$$

Where the residual

$$r_n = q_{S,n} - q_{Analytical,n} \tag{2.28}$$

The best fit of the analytical model is when the value of S is the minimum value. To minimize S the parameters are varied one at a time over a range of values to iteratively arrive at the minimum. First the contact resistance is held constant while varying the blood perfusion. The best value of w_b is then used while varying the contact resistance. This is repeated over finer ranges of values until sufficient resolution has been achieved. For each new parameter value tested a new core temperature is calculated and used. An example of the search process is demonstrated in Fig. 2.7.

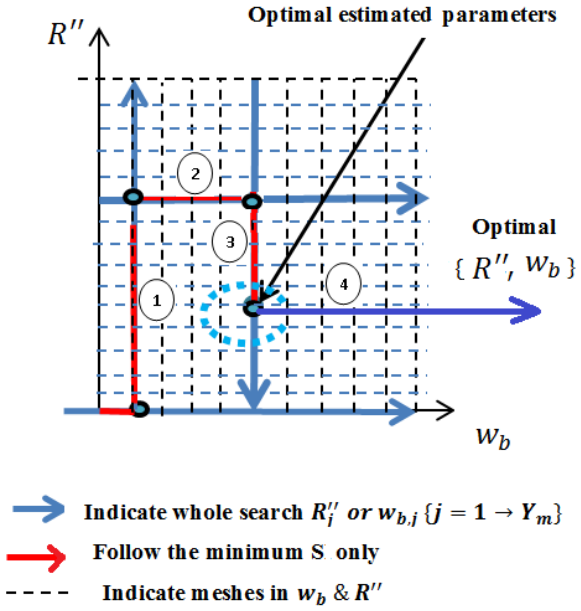

Figure 2.7 Search process for the optimal estimated parameters.

An example of one set of iterations for the thermal contact resistance and blood perfusion is shown in Fig. 2.8. For the first curve R'' is kept constant while w_b is varied as shown in Fig. 2.7 as paths 2 or 4. In similar fashion the second curve is for constant w_b with a varying R'' indicative of paths 1 or 3 in Fig. 2.7. The minimum value of each curve is then used for the next set of iterations.

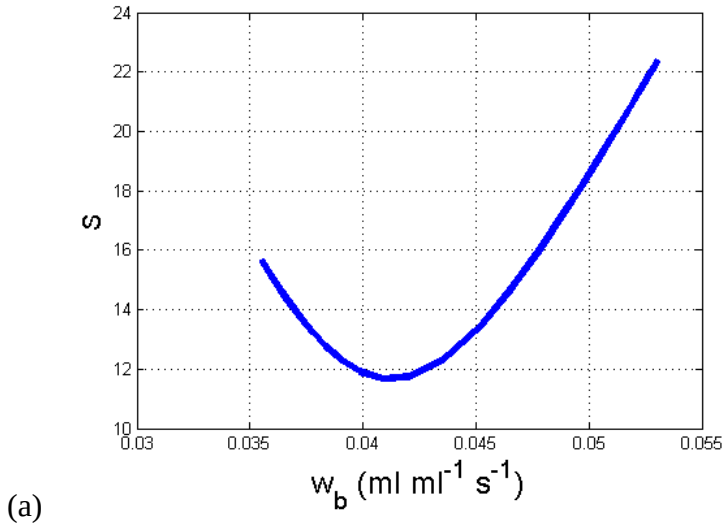

(a)

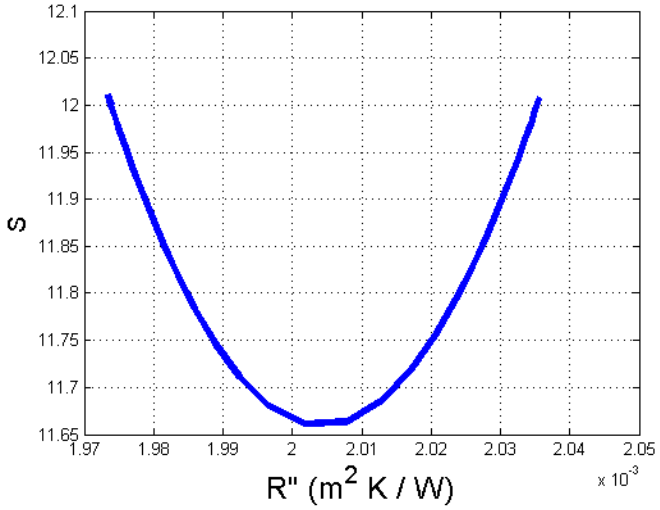

(b)

Figure 2.8 Illustration of one sequence of iterations for optimal parameters (a) Blood perfusion (b) Thermal contact resistance

A visualization of the entire parameter estimation field is illustrated in Figure 2.9. Here the value of S is displayed for a range of w_b and R'' values. The goal of the parameter estimation process is to find the minimum value of S at the bottom of the bowl. This requires the sequential optimization of one and then the other parameter to ever more finely hone in on the values that give the best match to the experimental data.

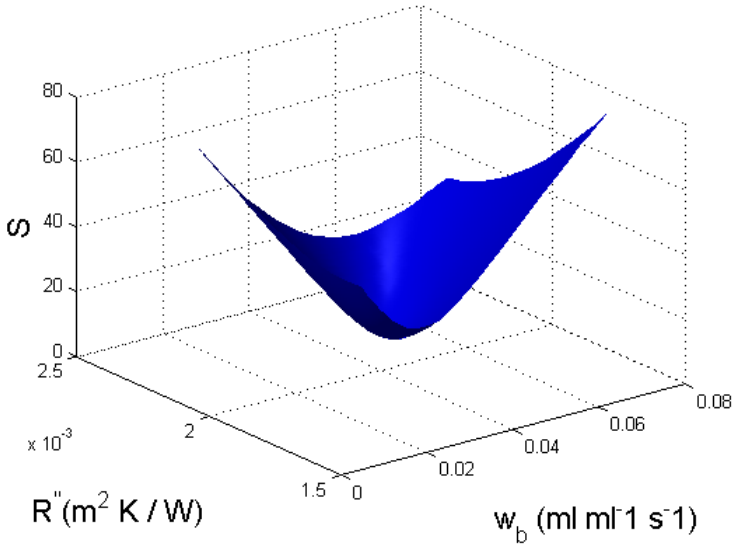

Figure 2.9 Visualization of the Two-Dimensional Optimization Problem

2.8 PARAMETER ESTIMATION WITH SIMULATED DATA

As a test of the parameter estimation, simulated sensor data was generated with different levels of random noise added to both the temperature and heat flux signals. An initial section of ten seconds at steady-state conditions was followed by a single step of the sensor temperature to simulate the thermal event produced by turning on the cooling air jets. The cooling lasted 60 seconds with data points at one second intervals, which gives a total of 71 values of simulated temperature and heat flux data. Table 2.2 shows a summary of the results of the five different sets of data with increasing random noise from 0% to 4%. The three estimated parameters from the output of the parameter estimation code are listed along with the average of the square root of the square of the residuals. The parameter estimation matches the original parameters within expected error for the 1% and 2% cases very well. The results for the 3% and 4% cases are farther from the original parameters. It will be seen later that the noise in the experimental data is typically below the one-percent level.

Table 2.2 Summary of Simulated Data Results

Level of noise	w_b (ml/ml/s)	R'' (m^2-K/W)	T_{core} (°C)	S (W/m^2)
Actual Parameters	0.04	0.002	37	0
0%	0.0399	0.00200	37.00	0.22
1%	0.0410	0.00200	36.96	11.67
2%	0.0388	0.00204	37.09	26.51
3%	0.0457	0.00211	36.89	29.62
4%	0.0519	0.00232	36.91	50.15

The corresponding input temperature curve is shown in the top portion of Fig. 2.10 for the one-percent noise case. The matching skin temperature is also shown for

comparison. The difference between the sensor and skin temperatures is a result of the thermal contact resistance and is consequently proportional to the instantaneous heat flux. Even though a step function is assumed for the sensor temperature, the skin temperature has the expected time lag, which smooths out the abrupt temperature change. The lower portion of the figure shows the match of the heat flux measurement and analytical result from the parameter estimation. The change in heat flux follows the step change of temperature. The two heat flux curves align very well except for the random noise that has been imposed on both signals. The analytical curve noise comes from the noise on the measured temperature signal that is the input driver for it.

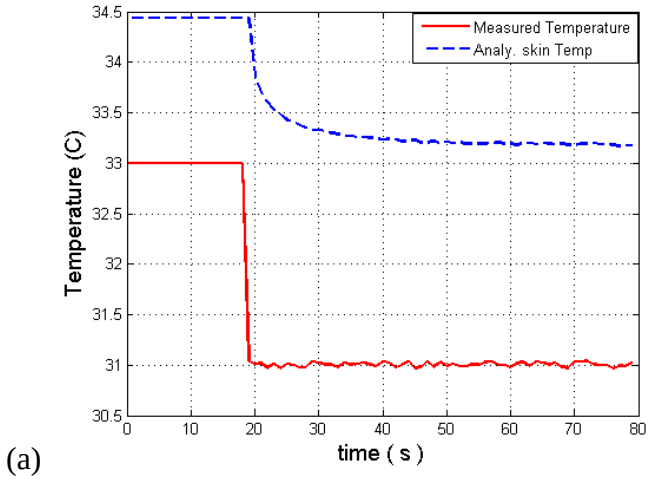

(a)

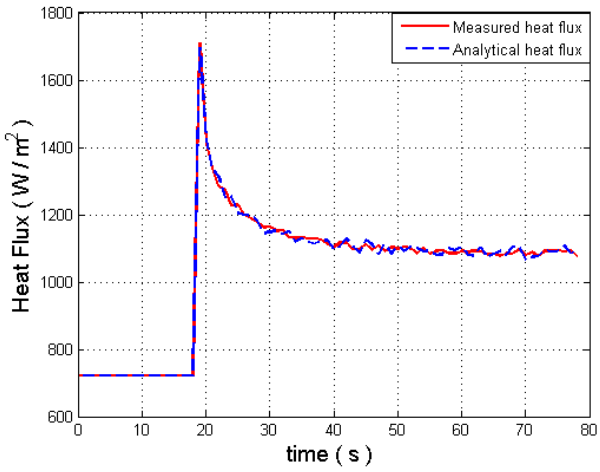

(b)

Figure 2.10 Analytical results for 1% noise added to measured temperature (a) and heat flux (b)

2.9 PARAMETER ESTIMATION WITH EXPERIMENTAL DATA

To test the validity of the mathematical model and the parameter estimation method a sample of experimental data was obtained with the CHFT sensor as shown in Figs. 2.1 and 2.2 using the Phantom Tissue System. Results are shown in Fig. 2.11 for a 15 cc/min perfusate flow rate, which gives a blood perfusion value close to that used for Figure 2.10. The measured temperature curves are similar in shape to those of the simulated data, but the initial temperature change is not as sharp as that in Fig. 2.10 and there is less

noise in the signal. The measured temperature and heat flux signals from the sensor were used with the parameter estimation program to obtain the core temperature, blood perfusion, and thermal contact resistance values listed in Table 2.3. The match between the analytical and experimental curves is quite good, as quantified by the low S value relative to the measured heat flux level.

The estimated blood perfusion is somewhat higher than the value of 0.035 ml ml^{-1} s^{-1} found by Mudalier et al. [2.9] for the same conditions with the phantom perfusion system. Their values, however, were determined with a different model that did not include the surface temperature measurements and the initial temperature distribution. Their model was shown to underestimate blood perfusion values [2.13] by an offset of almost 0.01 ml ml^{-1} s^{-1}. Including this offset brings their values to within better than ten percent of those in Table 2.3.

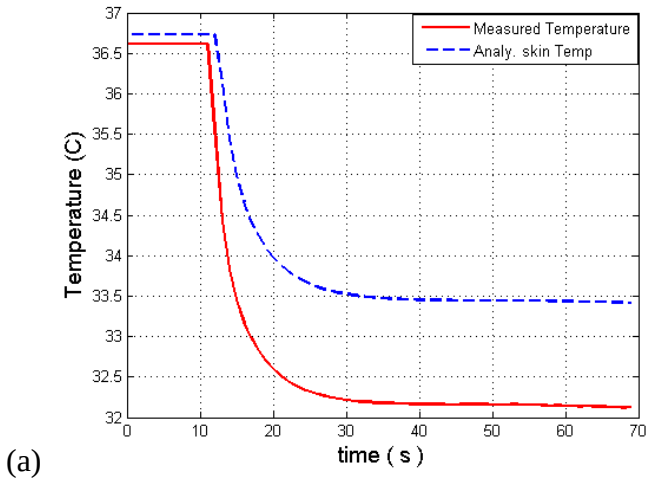

(a)

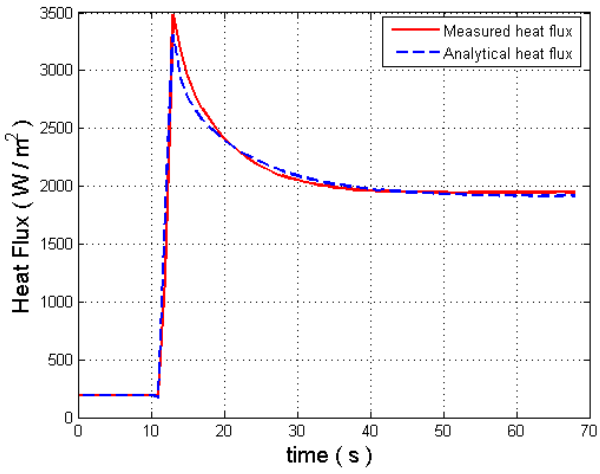

(b)

Figure 2.11 Measured and analytical skin temperature (a) and heat flux (b) from the experiment for 15 cc/min flow rate.

Table 2.3 Estimated Parameter Values for Figure 2.11

w_b (ml ml^{-1} s^{-1})	R'' (m^2-K/W)	T_{core} (°C)	S (W/m^2)
0.048	0.00099	37.45	89

2.10 DISCUSSION

The new mathematical model and analytical solutions for the CHFT blood perfusion measurement system were successfully tested against 1D and 2D finite-difference solutions. Simulated and experimental temperature and heat flux data were analyzed by combining the solutions with a parameter estimation routine. Optimum values of the core temperature, blood perfusion and thermal contact resistance were determined by minimizing the difference between the analytical and experimental heat flux values. The initial range of parameters that is tried covers the entire domain of possible values for the human system, although the initial range can always be extended for special circumstances. Because this is a non-linear problem, the search range is slowly narrowed to optimize the targeted parameters. This creates a robust method that can almost always find the correct optimum parameters for realistic data sets.

The addition of noise to the simulated data affected the estimated parameters, but only when the noise was larger than that from typical experimental results. It's clear that the experimental noise in Fig. 2.11 is less than the one-percent noise added for Fig. 2.10. The parameter estimation appeared to be true to the data, with values of the average square root of the square of the residuals that were actually slightly smaller than when the original parameters were used. This means that the noise affected the temperature and heat flux curves sufficiently to alter the parameters that they represented. It is, therefore, important to minimize the noise sources in the data or provide more dense data in time to minimize the effect of noise.

Other methods can also be used with these analytical solutions to create the thermal event, such as thermoelectric coolers or electric heaters. Heating, however, has the potential for burning the tissue and consequently would require a safety circuit. Cooling is therefore much safer. Moreover, different sensors can be used as long as both the surface heat flux and temperature of the tissue are measured. The heat flux signal is required because it is much more sensitive to the blood perfusion than the temperature alone.

2.11 CONCLUSIONS

A new mathematical model was derived for simulating experimental temperature and heat flux data from the surface of living tissue. It is an exact and efficient method to model the effects of blood perfusion, thermal contact resistance and core temperature on the tissue response to thermal events imposed on the surface. When an appropriate parameter estimation routine is combined with the analytical solution, it provides an efficient method to determine the values of these parameters from a single thermal event. The model was successfully tested with both simulated and experimental data for the dynamic process of cooling the tissue surface for a realistic measurement system. These results indicate the repeatability and stability of the mathematical model and associated parameter estimation.

2.12 ACKNOWLEDGMENTS

Words are not enough to stand and thank, the Libyan-North American (CBIE) scholarship program, Omar Almukthar University EL Beide-Libya for their grant to the first author.

2.13 REFERENCES

[2.1] Boellaard, R., Knaapen, P., Rijbroek, A., Lutersema, G. J. J., and Lammertsma, A. A. 2005, "Evaluation of basis function and linear least squares methods for generating parametric blood flow images using ^{15}O-water and positron emission tomography," *Molecular* Imaging and Biology, **7**, pp. 273-285.

[2.2] Petersson, J., Sanchez-Crespo, A., Rohdin, M., Montmerle, S., Nyren, S., Jacobsson, H., Larsson, S. S., Lindahl, S. G. E., Linnarsson, D., Glenny, R. W., Mure, M., 2004, "Physiological evaluation of a new quantitative SPECT method measuring regional ventilation and perfusion," Journal of Applied Physiology, **96**, pp. 1127-1136.

[2.3] Montet, X. Ivancevic, M. K.., Belenger, J., Jorge-Costa, M., Pochon, S., Pechér, A., Terrier, F., and Vallé, J.-P., 2003, "Noninvasive measurement of absolute renal perfusion by contrast medium enhanced magnetic resonance imaging," Investigative Radiology, **38**, pp. 584-592.

[2.4] Detre, J. A., Wang, J., Wang, Z., and Rao, H., 2009, "Arterial spin-labeled perfusion MRI in basic and clinical neuroscience," Current Opinion in Neurology, **22**, pp. 348-355.

[2.5] Valvano, J. W., Allen, J. T., and Bowman, H. F., 1984, "The simultaneous measurement of thermal conductivity, thermal diffusivity, and perfusion in small volumes of tissue," ASME Journal of Biomechanical Engineering, **106**, pp. 192-197.

[2.6] Khot, M. B., Maitz, P. K. M., Phillips, B. R., Bowman, H. F., Pribaz, J. J., and Orgill, D. P., 2005, "Thermal diffusion probe analysis of perfusion changes in vascular occlusions of rabbit pedicle flaps," Plastic Reconstructive Surgery, **115**, pp. 1103-1109.

[2.7] Khan, F., and Newton, D. J., 2003, "Laser Doppler imaging in the investigation of lower limb wounds," Journal of Lower Extremity Wounds, **2**, pp. 74-86.

[2.8] Ricketts, P. L., Mudaliar, A. V., Ellis, B. E., Pullins, C. A., Meyers, L. A., Lanz, O. I., Scott, E. P., and Diller, T. E., 2008, "Non-invasive blood perfusion measurements using a combined temperature and heat flux probe," International Journal of Heat and Mass Transfer, **51**, pp. 5740-5748.

[2.9] Mudaliar, A. V., Ellis, B. E., Ricketts, P. L., Lanz, O. I., Scott, E. P., and Diller, T. E., 2008, "A phantom tissue system for the calibration of perfusion measurements," ASME Journal of Biomechanical Engineering, **130**, 051002.

[2.10] Pennes, H. H., 1948, "Analysis of tissue and arterial blood temperatures in the resting human forearm," J. Appl. Physiol., **1**, pp. 93-122.

[2.11] Butkovskiy, A. G., 1982, *Green's Functions and Transfer Functions Handbook*, Ellis Horwood Limited.

[2.12] Von Rosenberg, D. U., 1969, *Methods for the Numerical Solution of Partial Differential Equations*, American Elsevier Publishing Company, Inc.

[2.13] Mudalier, A.V., Ellis, B. E., Ricketts, P. L., Lanz, O. I., Lee, C. Y, Diller, T. E., and Scott, E. P., 2008, "Noninvasive Blood Perfusion Measurements in an Isolated Rat Liver and an Anesthetized Rat Kidney," ASME Journal of Biomechanical engineering, **130**, 061013.

Chapter 3

Modeling and Estimating Simulated Burn Depth Using the Perfusion and Thermal Resistance Probe

The material in this chapter in press on the 15th of April 2013 in the Medical Devices

3.1 ABSTRACT

A new thermal perfusion probe operates by imposing a thermal event on the tissue surface and directly measuring the temperature and heat flux response of the tissue with a small sensor. The thermal event is created by convectively cooling the surface with a small group of impinging jets using room temperature air. The hypothesis of this research is that this sensor can be used to provide practical burn characterization of depth and severity by determining the thickness of non-perfused tissue. To demonstrate this capability the measurement system was tested with a phantom tissue that simulates the blood perfusion of tissue. Different thicknesses of plastic were used at the surface to mimic layers of dead tissue. A mathematical model [2.1] is used to determine the effective values of blood perfusion, core temperature, and thermal resistance from the thermal measurements. The analytical solutions of the Pennes bio-heat equation using the Green's function method is coupled with an efficient parameter estimation procedure to minimize the error between measured and analytical heat flux. Seven different thicknesses of plastic were used along with three different flow rates of perfusate to simulate burned skin of the phantom perfusion system. The resulting values of thermal resistance are a combination of the plastic resistance and thermal contact resistance between the sensor and plastic surface. Even with the uncertainty of sensor placement on the surface, the complete set of thermal resistance measurements correlate well with the layer thickness. The values are also nearly independent of the flow rate of the perfusate, which shows that the parameter estimation can successfully separate these two parameters. These results with simulated burns show the value of this minimally invasive technique to measure the thickness of non-perfused layers. This will encourage further work with this method on actual tissue burns.

Keywords: blood perfusion, thermal contact resistance, parameter estimation, heat flux measurement

3.2 INTRODUCTION

Early excision and grafting of burn wounds is more effective than any other intervention in decreasing morbidity and mortality, but is complicated by the challenge of accurately assessing burn depth and severity. Consequently, it is important to have the correct evaluation (whether skin grafting is required or not) as early as possible after the initial injury. The prediction of the ability of the body to heal the tissue and skin is critical. This is based on assessment of burn severity or burn depth, which is a qualitative judgment of the surgeon. Even experienced physicians seek additional means to help in these evaluations because of the difficulty and major ramifications of the decision.

Jaskille et al. [3.2] have reviewed techniques used to help the clinical decision making. Most are based on the change in blood perfusion that is caused by the burn.

Blood perfusion, defined as the fluid exchange rate through a given volume or mass of tissue (in units of ml/ml/s or ml/100g/min), represents the local, multi-directional blood flow through capillaries and intracellular spaces of living tissue. Several non-invasive methods have been developed that give varying success. Infra-red thermography measures tissue temperature distribution over a surface region in response to the heat transfer to the environment. Dynamic thermography provides a controlled heat flux to the tissue and records the transient response of the tissue surface temperature. Interpretation is still a challenge because a direct correlation with blood perfusion has not been developed. Renkielska et al. [3.3] identify an exponential time constant of the cooling after the heating is removed. The average value for severe burns was reported to be 9 seconds and that for burns that could heal without grafting was 12 seconds. The difference was supposedly due to greater blood perfusion for the latter case. The problems with any of the surface temperature methods are that the heat flux is not measured and the surface thermal conditions are not controlled. Simply measuring surface temperature is not sufficient to reliably indicate the tissue condition and blood perfusion. Surface heat flux and temperature are needed simultaneously to uniquely solve the heat transfer equation. Moreover, perfusion has a more profound effect on the heat flux (which isn't measured) than the temperature.

Although there are other imaging techniques that have been tried for burn assessment, by far the most successful has been Laser Doppler Imaging (LDI). A laser light is directed at the tissue and the reflection is collected with a video camera. The phase shift of the light is measured and correlated with the motion of red blood cells in the tissue. Because the depth and direction of the cell motion affect the signal, there is no method to calibrate the signal directly in terms of blood perfusion. Commercial units are available that output a qualitative color map of the perfusion that is indicative of the burn severity [3.4, 3.5]. Laser speckle imaging is another variation of the method with comparable results [3.6]. There are a number of factors that are not included with either method, however, that makes providing definitive guidelines for evaluating burn condition difficult [3.7]. In addition, the systems are large and expensive.

An alternative method for measuring blood perfusion is to use thermal clearance. This entails modeling of the conduction and convection heat transfer in living tissue. The most widely used approximation was developed by Pennes [3.8]. The energy loss due to blood flow is accounted for by including a perfusion term in the following conduction heat transfer equation.

$$(\rho c)_t \frac{\partial T}{\partial t} = k_t \nabla^2 T - (\rho c w)_b (T - T_{core}) \tag{3.1}$$

Here, the properties ρ, c, and k, are the local density, specific heat and thermal conductivity; T is the local temperature, T_{core} is the arterial temperature, t is time, w is the local perfusion, and the subscripts t and b refer to tissue and blood. Metabolic heat generation is assumed negligible.

The most common thermal method for invasively measuring blood perfusion is the Thermal Diffusion Probe [3.9-3.11]. A thermistor bead is situated at the end of a hypodermic needle that is inserted into the tissue, where it is used to both deposit thermal energy into the tissue and measure the temperature response. The drawbacks to this

method are that it is limited to applications in deep tissue (greater than 5 mm) and requires insertion into the tissue, which rules out applications for burns.

A thermal system was developed at Virginia Tech to measure perfusion from the surface of tissue, using convective air cooling to provide the thermal event [3.12]. Perfusion is estimated from sensor heat flux and temperature measurements using solutions of the two-dimensional Pennes equation and a parameter estimation routine. A tissue phantom test bed was also developed to calibrate and evaluate perfusion measurement devices [3.13]. The volumetric flow rate into the phantom tissue can be adjusted and quantified relative to perfusion through independent measurements and analysis. Animal tissue experiments using rat kidney and rat liver models illustrated the ability of the probe to track changes of perfusion in animal tissue [3.12, 3.14]. Although the sensor is in light contact with the tissue, it is encased in a thin layer of plastic and can easily be sterilized. Because it operates by cooling rather than heating, it is inherently safe for any patient application and is simple and easy to use.

The present hypothesis is that severely burned tissue does not have any blood perfusion. Consequently, the tissue has lower effective perfusion and an increased thermal resistance to the perfused tissue. If true, the perfusion and thermal resistance probe would provide a useful method for practical burn characterization of depth and severity. The probes are designed to be very portable, which offers the possibility for application in a wide variety of clinical environments, from the surgical suite to emergency response vehicles and military mobile units. The current paper is designed to test the accuracy of the mathematical model [3.1] to quantitatively measure the effects of non-perfused tissue on the measured blood perfusion and thermal contact resistance using the phantom tissue system [3.13].

3.3 EXPERIMENTAL METHODS

The phantom tissue system was developed to provide an easy-to-use method to test the blood perfusion probe [3.13]. In this paper, we extend the use of the phantom tissue model in quantifying and characterizing simulated burn depths. A simulated burn is modeled by replacing part of the perfused layer by a non-perfused layer. The non-perfused layer is simulated using plastic sheets. Six difference thicknesses of plastic are used to simulate different burn depths. The perfusion and thermal resistance probe provides surface temperature and heat flux measurements to the mathematical model [3.1]. The model is used to estimate three parameters, which are blood perfusion, core temperature and contact resistance. These are used to characterize the simulated burn.

3.3.1 The phantom tissue system

The phantom system provides a repeatable and known flow rate for perfusion studies. When the jets are activated, the sudden increase in convection gives a corresponding increase in heat transfer from the tissue surface through the combined heat flux and temperature sensor (CHFT) from the perfused tissue, as illustrated in Fig. 3.1. The phantom tissue system is designed to provide calibration for blood perfusion with controlled fluid flow rates using a small pump and flow control valve. The phantom tissue provides repeatability of perfusion through tissue in response to a surface thermal event. Another advantage of the use of phantom tissue is to minimize the use of an animal model. Controlling phantom flow rates prevents the need for surgery when animal

models are used; moreover, quantifying a burn depth using an imposed simulated burn minimizes the need for applying a burn to an animal.

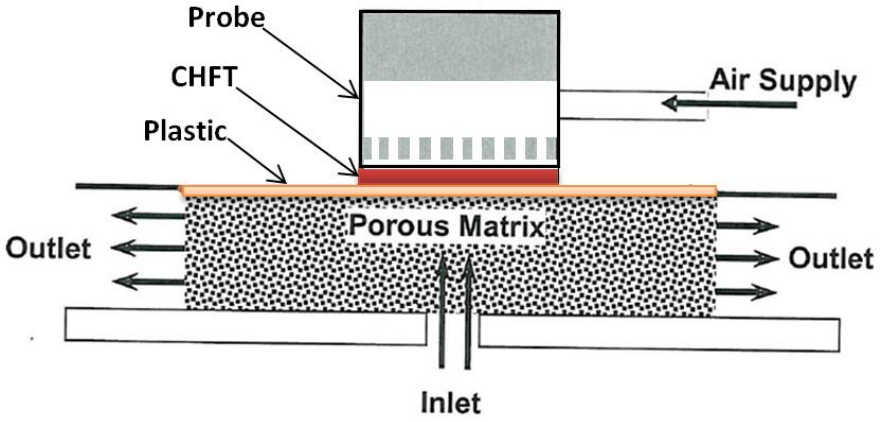

Figure 3.1 Perfusion probe situated on simulated tissue.

3.3.2 The perfusion and thermal resistance probe

The main component of the perfusion and thermal resistance probe is a combined heat flux and thermocouple sensor (CHFT). Its size is 10 mm^2 with a thickness of 0.25 mm [3.12]. The resulting surface temperature and heat flux signals are input as a function of time directly into a DAQ USB-2416 and then to a standard laptop computer. The sampling rate is one sample per second for each of the two channels required. TracerDaq software was used to record temperature and heat flux measurements. The thermal event is provided by nine jets of air at room temperature impinging onto the top side of the CHFT sensor. The sensor is first put on the tissue and allowed to equilibrate thermally. The perfusion probe required a couple of seconds to record the steady state temperature and heat flux measurements. Ten seconds were used to record ten samples of ten measured temperatures and heat fluxes. Then the thermal event is initiated and the TracerDaq records the temperature and heat flux. The measurements are saved as a text format file for each test and used in the mathematical model [3.1], which is encoded into MATLAB.

3.3.3 Burn simulation

When a burn is imposed on a tissue, the depth of the burn will influence the value of the predicted blood perfusion because a severe burn will eliminate most of the network vessels from being perfusion suppliers to burnt region. The phantom tissue model assumes that the perfused tissue is a completely non-perfused tissue. Consequently, there are two regions: 1) normal perfused tissue which is beneath 2) the non-perfused layer. Even if the burn is not completely non-perfused tissue, this model can simulate the situation with an equivalent non-perfused layer.

The phantom tissue system controls both blood perfusion and core temperature. The phantom tissue simulates the processes of convection heat transfer caused by a controlled perfusion. Different thicknesses of two kinds of plastic (Kapton and Lexan) were used to simulate different possible burn depths. Plastic materials were used because of the available range of thicknesses and thermal resistances. Thicknesses of the Kapton used were 1, 2, 3, and 5 mils (0.025 - 0.127 mm) while the Lexan thicknesses were 5, 10, and 15 mils (0.127 – 0.381 mm). The mathematical model is used to estimate blood perfusion, thermal contact resistance, and core temperature. The plastic thermal conductivity, the thermal contact resistance due to sensor-tissue contact, and the simulated burn depth (plastic thickness) are the results from this study at three different phantom flow rates.

3.4 MODELING OF PERFUSION EFFECTS

The general model of the perfusion effects on temperature and heat transfer is built from the Pennes equation (3.1). For this work the Pennes equation (3.1) is considered in one dimension and simplified by the assumption of the equality of tissue and blood properties with average values [3.15, 3.16] of k = 0.5 W/m-K, ρ = 1050 kg/m^3, and c = 3800 J/kg-K. The thermal diffusivity is defined as $\alpha = (k/\rho c)_t = (k/\rho c)_b$

$$\frac{\partial T}{\partial t} = \alpha \frac{\partial^2 T}{\partial x^2} - w_b(T - T_{core}) \tag{3.2}$$

Figure 3.2 illustrates the simulated burn model with the corresponding boundary conditions. The simulated burn is a sheet of plastic, while the tissue region represents no burn effects or “healthy tissue”. A general analytical solution was developed previously for healthy tissue using the Green’s function method [3.1]. The 1D model was compared with a 2D cylindrical finite difference solution of the Pennes equation with only 3% error [3.1] for the size of the probe and time of testing considered. The thermal contact resistance between the sensor and plastic layer is represented by R''_0, while the thermal resistance of the plastic layer is $R''_p = L/k_p$. L and k_p are thickness and thermal conductivity of the plastic layer, respectively.

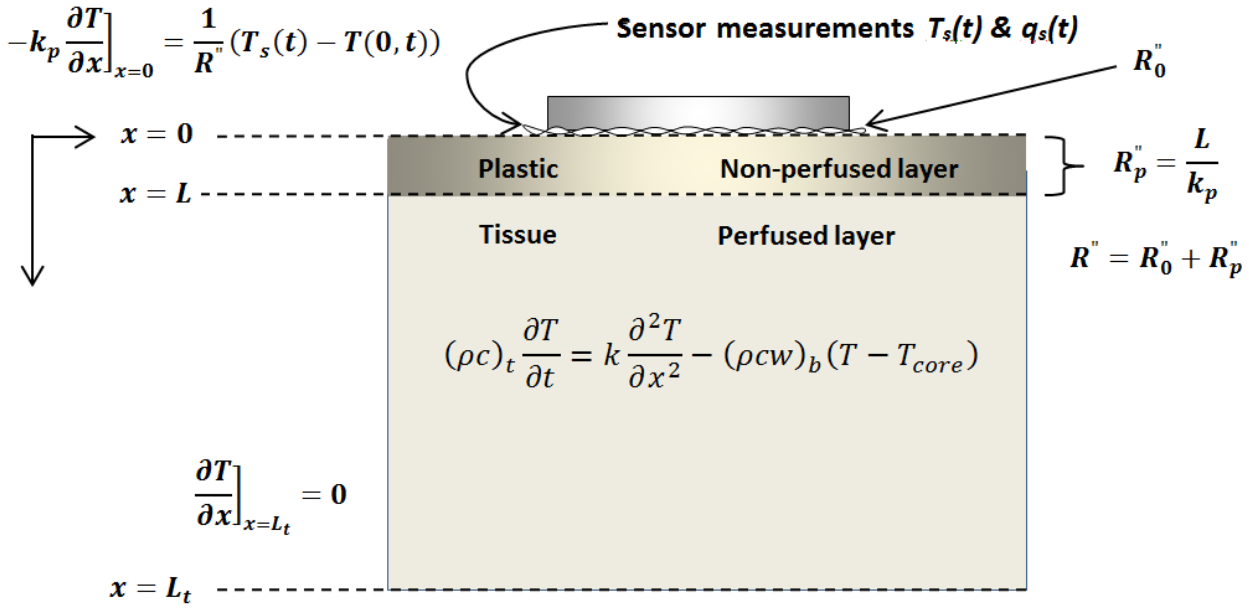

Figure 3.2 Modeling a simulated burn depth.

To validate the predicted perfusion during an imposed simulated burn, two finite-difference models were used. The simulated burned layer is either expressed as an additional thermal resistance neglecting its thermal capacitance or as an additional layer with all of the plastic properties. The two models are used to validate the ability of the general model in predicting the perfusion accomplished by a simulated burn. This is summarized in Fig. 3.3. The analytical solution treats the problem as one layer with an added thermal resistance. The finite-difference solutions use both a one-layer and two-layer model to compare the solution results. The one-layer model lumps the two thermal resistances R''_0 and R''_p together and only solves the full transport equation in the tissue compartment. The two-layer model solves equation 3.2 in both layers, using zero perfusion and appropriate thermal properties in the plastic layer. The details of the solution techniques and results are given in the following sub-sections.

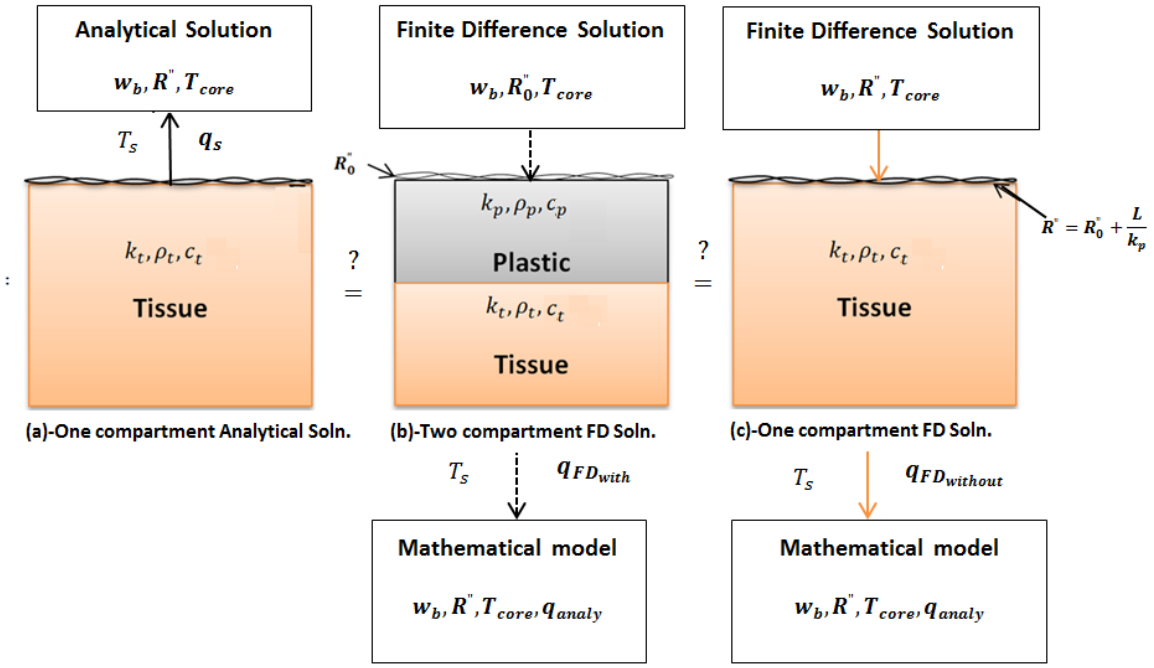

Figure 3.3 Validation of the two models in predicting blood perfusion of a simulated burn

3.4.1 One compartment analytical model

The arterial temperature is assumed to be equal to the core temperature of the tissue, T_{core}. The perfused tissue is assumed to be semi-infinite in extent, giving the far boundary condition as

$$\frac{\partial \theta}{\partial x}|_{x\to\infty} = 0 \tag{3.3}$$

where $\theta = T - T_{core}$. At the surface of the tissue (x=0) the heat flux must match the heat flux through the thermal contact resistance. This along with the measured surface temperature of the CHFT (θ_s) gives the second boundary condition

$$-k\frac{\partial \theta}{\partial x}|_{x=0} = \frac{1}{R''}\left(\theta_S(t) - \theta(0,t)\right) \tag{3.4}$$

Before the thermal event is initiated by turning on the air jets, the heat flux at the surface is balanced by the warming effects of the blood perfusion in the tissue. The initial steady-state temperature distribution in the tissue θ_i(x) is obtained by solving the steady-state version of equation 3.2 along with the boundary conditions from equation 3.3 and 3.4 [3.1]

$$\theta_i(x) = \theta(x,0) = \frac{\theta_{S,0}}{\left[k\,R^{"}\sqrt{\frac{w_b}{\alpha}}+1\right]}\, e^{-\sqrt{\frac{w_b}{\alpha}}x} \tag{3.5}$$

Where the initial sensor temperature is $\boldsymbol{\theta_{S,0}}$. The measured sensor temperature profile is modeled as a series of steps

$$\boldsymbol{\theta_S(t) = \theta_{S,0} + \sum_{n=1}^{N_{max}} \Delta\theta_{S,n} \, . \, H(t - t_n)} \quad \textbf{(3.6)}$$

where $H(t)$ is the step function and $\theta_{S,n}$ is sensor temperature at time $t(n)$. The visual representation of the sensor temperature response of a thermal event is shown in Fig. 3.4.

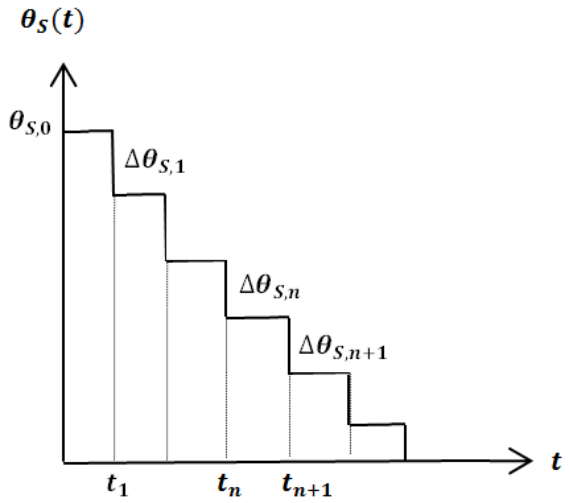

Figure 3.4 Measured temperature from a thermal event

The analytical model makes use of two solutions, which are the transient and steady-state solutions of equation (3.2). The initial heat flux is calculated from the first derivative of equation (3.5).

$$\boldsymbol{q_i(x = 0) = -k\,\theta_{S,0}\left[\frac{\sqrt{w_b/\alpha}}{1 + R''k\sqrt{w_b/\alpha}}\right]} \quad (3.7)$$

where the initial sensor temperature minus the core temperature is $\boldsymbol{\theta_{S,0}}$. The heat flux in equation (3.7) is defined as positive from the tissue and averaged for the initial ten seconds in the absence of the thermal event. The core temperature is related to the average sensor temperature T_s and heat flux q_i for this time prior to the thermal event using equation (3.7).

The transient heat flux describes the response to the thermal event. Using superposition, the temperature is constructed as $\theta(x,t) = \theta_i(x) + \theta_T(x,t)$). The Green's function formulation [3.1] was used to determine the corresponding solution.

$$\boldsymbol{\theta_T(x,t) = \frac{1}{\rho c}\int_{t_0=0}^{t} \frac{1}{R''}\left(\theta_S(t_0) - \theta_{S,0}\right)\, G(x,t|0,t_0)dt_0} \quad (3.8)$$

where the Green's function is

$$G(0,t|0,t_0) = \frac{2\,e^{-w_b(t-t_0)}}{\sqrt{4\pi\alpha(t-t_0)}} - \frac{erfc\left(\frac{\sqrt{\alpha(t-t_0)}}{k\,R''}\right) e^{\left(\frac{\alpha}{(k\,R'')^2}-w_b\right)(t-t_0)}}{k\,R''} \qquad (3.9)$$

The transient heat flux (defined as positive from the tissue to the sensor) is found directly from the surface temperature of the tissue and the sensor temperature

$$q_T(x=0,t) = \frac{\theta_T(0,t) - \theta_S(t)}{R''} \qquad (3.10)$$

The total heat flux from the tissue is the superposition of the steady and transient solutions

$$q(x=0,t) = q_i(x=0) + q_T(x=0,t) \qquad (3.11)$$

Figure 3.5 illustrates a typical set of temperature and heat flux curves for the measured and analytical data (5 mils of Kapton with a flow rate of 30 cc/min). The beginning of the thermal event is evident when both the heat flux increases and the sensor temperature drop abruptly. The difference between the measured temperature on the sensor and the calculated skin temperature in Fig. 3.5a represents the effect of the thermal resistance between the sensor and the perfused tissue. The measured sensor temperature is used as the input to the analytical model to generate the corresponding heat flux shown in Fig. 3.5b, using the optimal estimated parameters of blood perfusion, thermal resistance and core temperature. When using the correct parameter values for each set of data, the measured and calculated heat flux curves typically match very well.

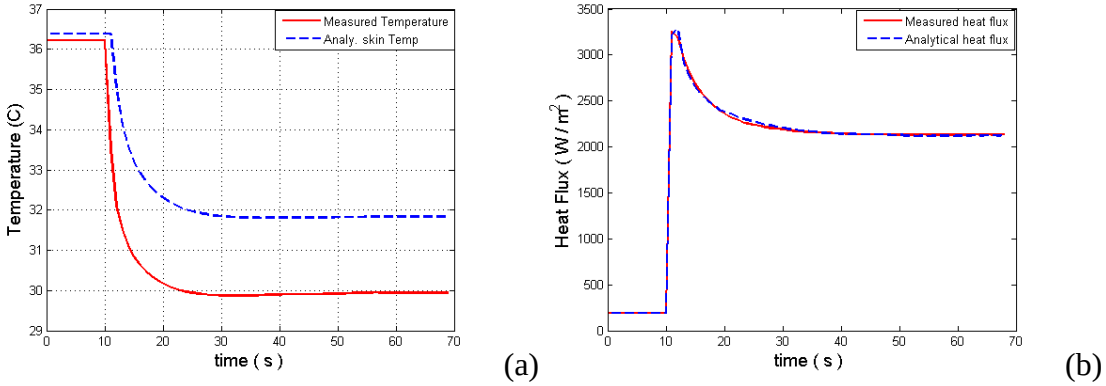

(a) (b)

Figure 3.5 Sample surface temperature (a) and heat flux signals (b) (5 mils Kapton with 30 cc/min flow rate).

A parameter estimation code is used to search for the three desired parameters from the measured data. The nonlinearity of the Green's function based analytical solution makes it difficult for parameter estimation techniques to converge reliably to the correct answers.. The parameter estimation code is coupled with both transient and steady state analytical solutions to estimate the core temperature, the blood perfusion, and the contact resistance between the tissue surface and the sensor, as illustrated by chart in Fig. 3.6. The initial measured heat flux is used with each set of estimated thermal resistance and blood perfusion values to calculate the value of $\boldsymbol{\theta_{S,0}}$ from equation (3.7). This specifies the core temperature as $T_{core} = T_s - \boldsymbol{\theta_{S,0}}$, where T_s is measured sensor temperature. The calculated transient heat flux (using the experimental temperatures) is compared with the experimental heat flux using the sum of the squares of difference of the values. This process is repeated for different values of the parameters: first over a range of blood perfusion values followed by a range of thermal resistance values. The ranges are then slowly narrowed until optimum values are achieved. The parameter estimation is highly iterative because of the non-linear relationships and the interdependence of the three parameters that are being estimated.

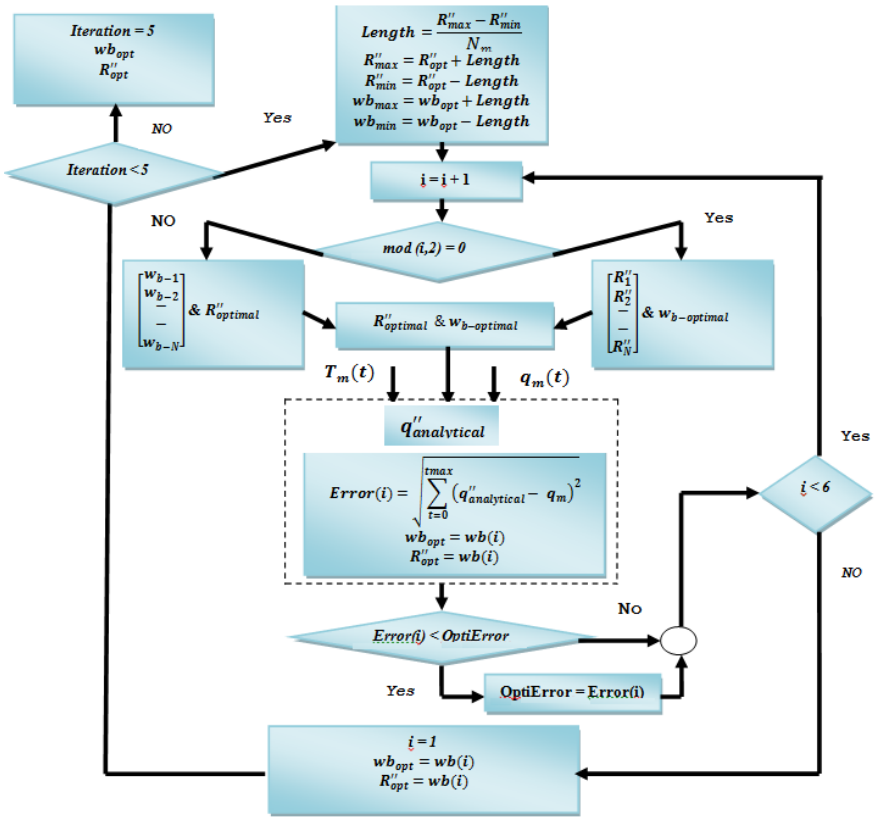

Figure 3.6 Search process for the optimal estimated parameters.

3.4.2 Numerical finite-difference model (two compartments)

Finite-difference solutions were generated for both the one-compartment and two-compartment models. The one compartment model has the same overall thermal resistance, but no thermal capacitance. The two-compartment model includes the thermal contact resistance with capacitance in the plastic layer. Consequently, the first two

boundary conditions for the two-compartment model are the same as for the one-compartment model. The last two are specific to the added plastic layer.

$$\frac{\partial \theta_t}{\partial x}|_{x \to L_t} = 0 \tag{3.12}$$

$$-k_p \frac{\partial \theta_p}{\partial x}|_{x=0} = \frac{1}{R''}\left(\theta_S(0) - \theta_p(0,0)\right) \tag{3.13}$$

$$k_p \frac{\partial \theta_p}{\partial x}|_{x=L} = k_t \frac{\partial \theta_t}{\partial x}|_{x=L} \tag{3.14}$$

$$\theta_p|_{x=L} = \theta_t|_{x=L} \tag{3.15}$$

where subscript *t* is for tissue and subscript *p* is for plastic (*wb* = 0). Because the tissue has blood perfusion, there is a non-linear temperature gradient in the tissue at steady-state conditions. Therefore, the proper steady-state solution of equation (3.2) is required to initiate the finite-difference solutions for the two models. For the one-compartment model the initial temperature distribution is given by equation (3.5). For the two-compartment model the initial temperature distribution is derived by solving the steady-state version of equation (3.2) with the boundary conditions in equations (3.12-3.15). The steady-state form of equation (3.2) is

$$\frac{\partial^2 \theta}{\partial x^2} - m\,\theta = 0 \tag{3.16}$$

where $m = \sqrt{\rho c w_b / k_t}$. The corresponding solution for the perfused compartment (tissue) is

$$\theta_t(x) = A_1 \sinh(m\,x) + A_2 \cosh(m\,x) \tag{3.17}$$

$$A_2 = \frac{\left[1 + \frac{L}{k_p R''}\right] C_2 - \frac{L}{k_p R''}\theta_s(0)}{\cosh(m\,L) - \tanh\big(m(L + L_t)\big)\sinh(m\,L)} \tag{3.18}$$

$$A_1 = -A_2 \tanh\big(m(L + L_t)\big) \tag{3.19}$$

For the plastic compartment (non-perfused layer) the solution is linear and matched with the heat flux and temperature at the intersection between the two compartments.

$$\theta_p(x) = C_1 x + C_2 \tag{3.20}$$

$$C_1 = -\frac{1}{k_p R''}(\theta_s(0) - C_2) \tag{3.21}$$

$$C_2 = \frac{\theta_s(0)\, a_1 - \frac{L}{k_p R''}\theta_s(0)\, b_1}{a_1 - \left[1 + \frac{L}{k_p R''}\right] b_1} \tag{3.22}$$

$$a_1 = \frac{\frac{1}{R'' m\, k_t}}{\left[sinh(mL) - tanh\big(m(L + L_t)\big)\ cosh(mL)\right]} \tag{3.23}$$

$$b_1 = \frac{1}{cosh(mL) - tanh\big(m(L + L_t)\big)\, sinh(mL)} \tag{3.24}$$

The initial solution is the combination of the solutions for the two-compartments.

$$\theta_i(x) = \begin{Bmatrix} \theta_p(x) & x \le L \\ \theta_t(x) & L < x \le L_t \end{Bmatrix} \tag{3.25}$$

Figure 3.7 illustrates the initial temperature distribution of the two finite-difference models for an example of plastic layer of Lexan with a 15 Mil thickness. The initial temperature distribution in the plastic is linear since the blood perfusion term is zero, while the tissue region has blood perfusion. The coordinate x is from the surface of the model. The added thermal resistance of the plastic layer lowers the surface temperature.

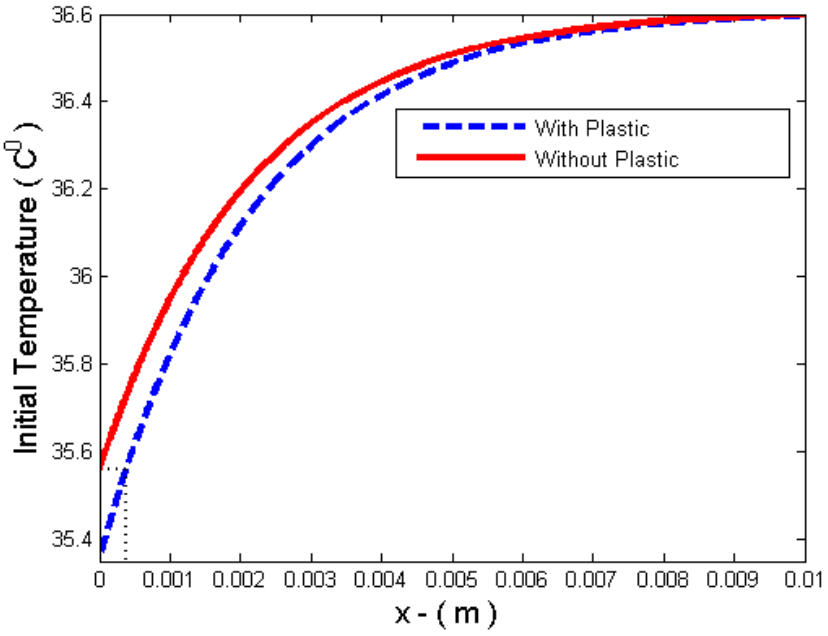

Figure 3.7 Initial temperatures for one compartment and two compartments models of 15 mils of plastic

The transient finite-difference scheme uses the Crank Nicolson solution method [3.12]. We tested the stability of space and time meshing for the 15 mils Lexan example. A total

of 20,000 nodes were used in the x direction with a uniform spacing for both plastic and tissue. The tissue thickness was set at $L_t = 2\ cm$, which is twice thermal penetration depth even at the steady-state condition, as shown in Fig. 3.7. The time step was Δt =1 s. The results were unaffected when the size of Δt and Δx were varied by a factor of ten.

3.4.3 Thermal Capacitance Effects

The analytical solution includes the thermal resistance effect of the plastic but neglects the thermal capacity effect of the plastic layer. To evaluate the effect of this assumption on the estimated parameters an example was solved with 15 mils of simulated burn of Lexan layer. The phantom flow rate was adjusted to 15 cc/min. The analytical model was first used with this set of experimental temperature and heat flux values to estimate blood perfusion, thermal resistance and core temperature for this test. The properties such as plastic thermal conductivity and thermal contact resistance were obtained by averaging the estimated values from measurements. Thermal contact resistance of Lexan is approximately $R"_o$ = 6.3 x 10^{-4} m^2-K/W and the thermal conductivity of the Lexan is k_{Lexan}=0.596 W/m-K. The Lexan specific heat is estimated as 1260 J/kg-K and the density is 1200 kg/m^3 [3.17].

Table 3.1 illustrates the ability of each model in predicting the blood perfusion, core temperature and thermal resistance. The original values from the analytical model and experiments are shown in the 1st column. These values were used along with the temperature measurements in the finite-difference programs as input to generate a new set of heat flux values. These heat flux and temperature profiles were used in the parameter estimation routine to generate new values of blood perfusion and the thermal contact resistance. Consequently, the important comparison is between the results from the two finite-difference models. The 2nd column shows the estimated parameters for the two-compartment finite-difference model, which includes the effect of the plastic thermal capacitance. The 3nd column is for the one-compartment finite-difference model, which like the analytical model does not include the thermal capacitance of the plastic layer. Note that the thermal resistance used in the one-compartment model is $R_0^" + \frac{L}{k}$ and for the two-compartment model is $R_0^"$. Both the estimated blood perfusion and the thermal contact resistance are slightly higher by a maximum of about 20% for the one-compartment model than for the two-compartment model which includes the thermal capacitance. Therefore, the one-compartment and analytical models, which don't include the thermal capacitance in the plastic layer, appear to have higher values of perfusion and thermal resistance for thick layers of plastic. The effect is smaller for thinner layers of plastic.

Table 3.1 The estimated T_{core}, w_b, and R" Values

Method	Analytical Solution Case (a)	Finite Difference Solution Case (b) - (Plastic)	Finite Difference Solution Case (c) - (no Plastic)
model	Analytical one compartment without capacity effect	Two compartment model with plastic capacity effect	One compartment model without capacity effect
$R^"$	0.00138	0.0013169	0.0016119
w_b	0.051	0.0554913	0.0704159
T_{core}	36.61	36.599	36.59

The effect of the thermal capacitance on the heat flux can be seen in Figure 3.8. The original measured heat flux is plotted along with the values calculated with the two finite-difference programs based on the measured sensor temperature curve and the parameter values in column 1 of Table 3.1. The effect of the thermal capacitance in the plastic layer is to increase the heat flux during the initial transient portion of the curve. As indicated in Table 3.1, this makes the one-dimensional model appear to have higher thermal resistance and higher blood perfusion. Consequently, lower values must be used to match the measured data. The resulting parameter estimation using the analytical model will consequently give slightly lower values of blood perfusion and thermal contact resistance. This effect will be largest for the thickest plastic layers, decreasing to no effect for the thinnest layers. The core temperature appears to be unaffected by these approximations. Because of the increased simplicity and speed of calculations during the parameter estimation process, the analytical model is preferred over the two-compartment finite-difference solution. Understanding the small effects of the approximations should allow the analytical model to discriminate the burn characteristics at least as well.

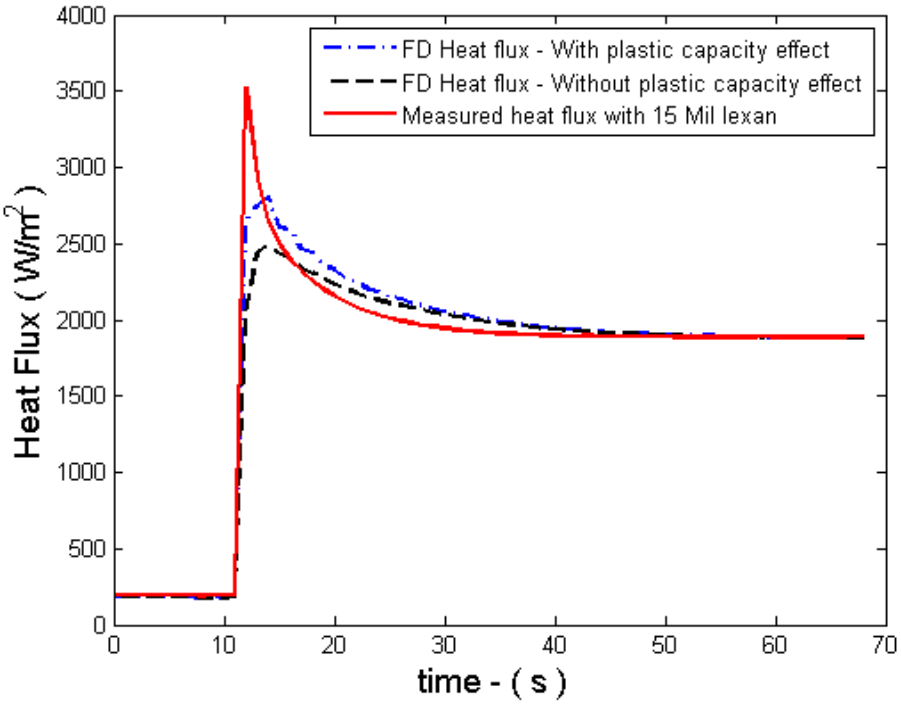

Figure 3.8 Heat fluxes for two models versus measured heat flux for 15 mils of plastic

3.5 EXPERIMENTAL RESULTS

Two types of plastic (Kapton & Lexan) with a total of six different thicknesses were used with the phantom tissue system to simulate six possible burn depths. Measurements were done at three phantom tissue flow rates of 5, 15, and 30 cc/min to test the ability of the analytical model to respond to different perfusion values. Five separate tests were performed with each of the plastic layers. To simulate actual conditions the sensor was removed after testing the three flow rates for each plastic layer and then re-applied.

Experiments were performed on all of the plastic layers before beginning the next round of tests. This includes the thermal contact resistance uncertainty of placing the sensor on the tissue for each measurement.

Figure 3.9 shows the average values of the estimated blood perfusion for each simulated burn depth. The perfusion values for all three different flow rates show a consistent decrease for increased thickness of the non-perfused layer. This is up to a 50 per cent decrease in perfusion for the thickest layers tested. As discussed in the previous section, less than half of this apparent decrease is due to approximations of the analytical model. The remainder is due to the presence of the non-perfused layer, which acts to shield the thermal effects of the perfusion from the sensor. The actual perfusion in the underlying tissue remains the same. Therefore, this acts as an important indicator for the presence of the non-perfused layer. The assumptions in the analytical model actually are beneficial because they act to augment this signal.

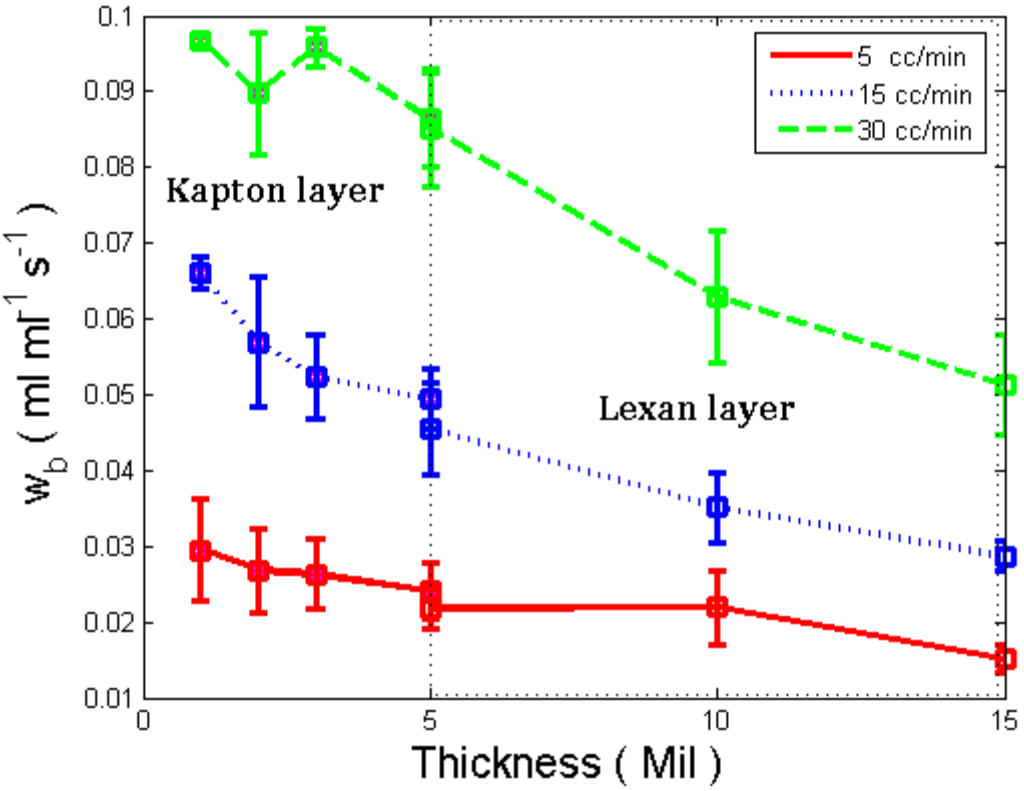

Figure 3.9 Measured blood perfusion values with 95% confidence integrals

Figures 3.10, 3.11 and 3.12 illustrate averaged values of thermal resistance at each of the imposed thicknesses along with the 95% confidence intervals around the averages. Figure 3.10 is made using a flow rate of 5 cc/min, with Fig. 3.11 at 15 cc/min and Fig. 3.12 at 30 cc/min. Two different sensor settings were used. The first sensor setting is indicated as 5 measurements, the same as in Fig. 3.9. Because of the relatively large confidence intervals, another ten measurements were done on the Kapton layers without removing the sensor between tests. It is assumed that the thermal contact resistance is the same for all of the tests for each layer and does not change with application, as in the original five tests. The difference between the confidence intervals between the sets of 5

and 10 measurements indicates that the differences of the thermal contact resistance are likely the cause of the higher confidence interval of the 5 measurement tests. The value of the contact resistance is almost independent of the change in the sensor's setting. That provides powerful repeatability to the model in predicting the burn depth.

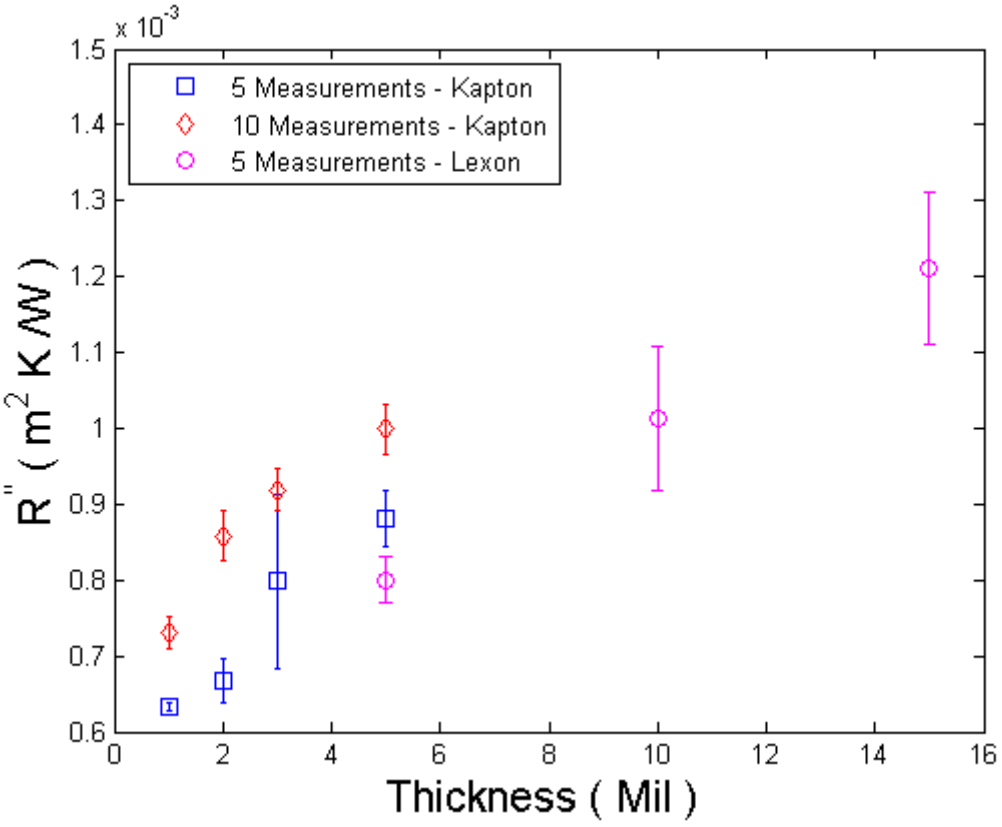

Figure 3.10 Estimated contact resistances with confidence integrals at 5 cc/min flow rate

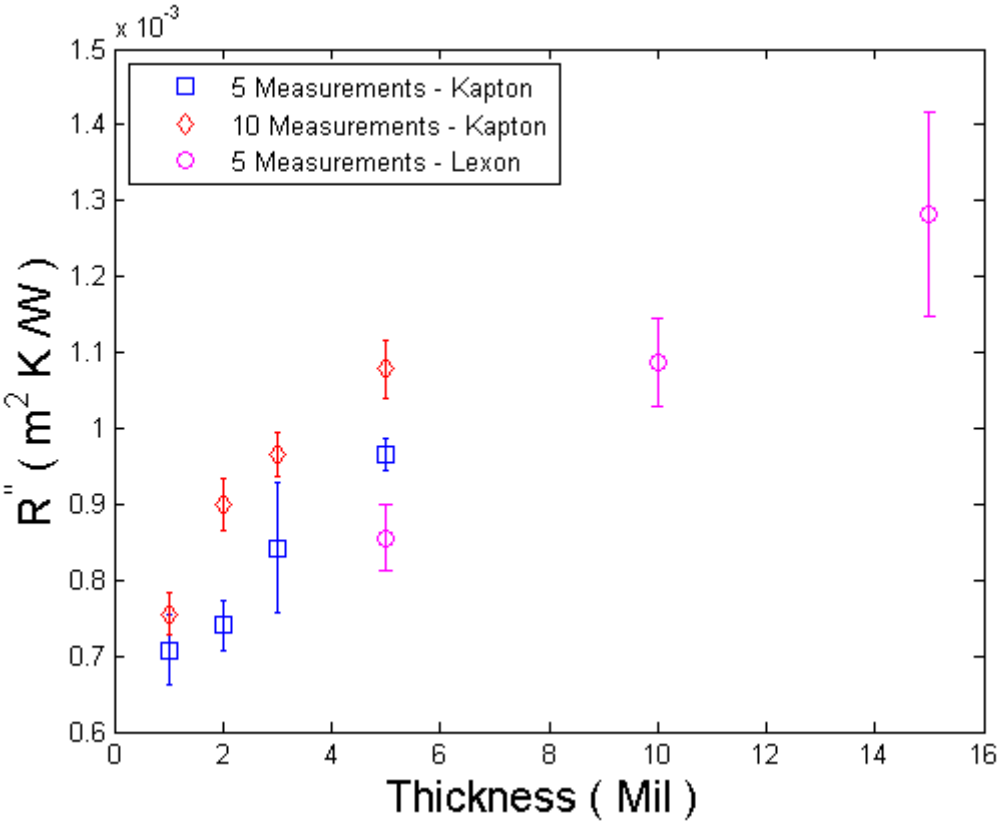

Figure 3.11 Estimated contact resistances with confidence integrals at 15 cc/min flow rate

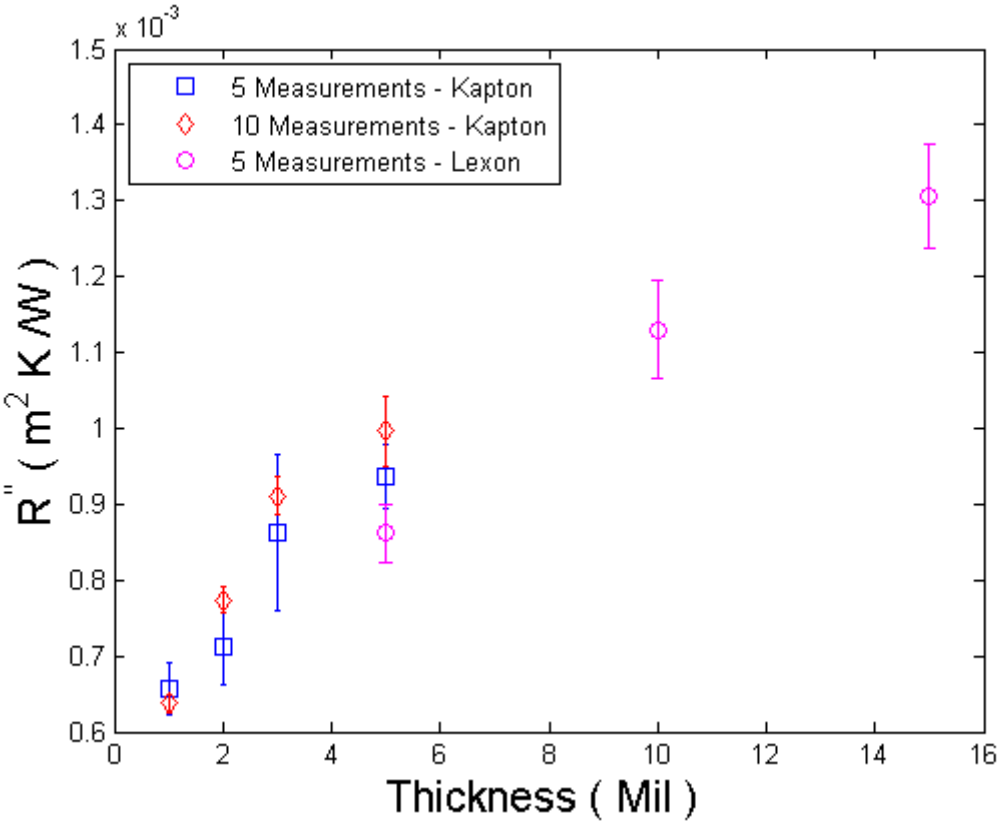

Figure 3.12 Estimated contact resistances with confidence integrals at 30 cc/min flow rate

To further analyze the data in these figures the model for the thermal resistance in Fig. 3.2 was used

$$R''(L) = R_0'' + \frac{L}{k} = C_1 + C_2 L \qquad \textbf{(3.26)}$$

where L is the plastic thickness and k is the plastic thermal conductivity. A linear interpolation on the averaged contact resistances as a function of thickness was done for each material at each flow rate.. The first term of equation (3.26) provides the thermal contact resistance between the sensor and the surface of the simulated burn. The second term gives the inverse of the thermal conductivity. This was done for each of the data sets in Figures 3.10 to 3.12. The resulting six values from the Kapton were averaged together and the three from the Lexan were averaged together. This gives a thermal conductivity of the Kapton of k = 0.354 W/ m-K and a thermal conductivity value for Lexan of k = 0.596 W/m-K. The thermal contact resistance for both materials was the same, R_o" = 0.00063 m^2-K/W. The best published thermal conductivity values for Kapton appear to be k = 0.28 W/m-K [3.18] and k = 0.32 W/m-K [3.19]. This is a reasonable match with the value currently obtained for Kapton. The value for Lexan is higher than the typical values quoted, . There are several possible reasons, k = 0.2 W/m-K [3.17]. There are several possible reason for this. First, the surface of the Lexan next to the simulated tissue was quite rough and would provide a much larger surface area for heat transfer than the

assumed smooth surface. Second, as indicated in the previous section the thermal resistance values for the large thicknesses of Lexan used were estimated low because of the thermal capacitance effect. This would give artificially high values of thermal conductivity.

The ultimate goal of this research is to be able to predict the thickness of the non-perfused layer. The analytical model is designed to estimate the burn depths from thermal resistance, which is one of the three estimated parameters. The thermal properties of the plastic layers used were taken from the previously determined values, and averaged thermal resistance values are shown in Figures 3.10 to 3.12. The results for each thickness and flow rate were used to find the effective thickness of material as calculated by

$$\boldsymbol{L = k * \left(R'' - R_0''\right)} \qquad \textbf{(3.27)}$$

Figure 3.13 presents the results as the estimated thickness from equation (3.27) versus the known thickness of the plastic. This represents the measured burn depth versus the actual. The values are nearly the same for each of the three flow rates. As would be expected, the estimated values increase linearly with the imposed thicknesses. To quantify the ability of an individual measurement to match the actual thickness of plastic, standard deviation where calculated of each measured value relative to the known plastic thickness. Because much of the overall thermal resistance (R") is due to the thermal contact resistance (R_0''), the standard deviation of measured thicknesses ranged from 30% to 75%. With better control and repeatability of sensor placement, it is anticipated that this number could be substantially decreased. One possibility would be to place a thin layer of liquid between the sensor and tissue (plastic).

Figures 3.9 and 3.13 together describe the causes and effects of six different simulated burns on phantom tissue at three different flow rates. Although the thickness is given directly from the thermal resistance measurement as shown in Figure 3.13, the blood perfusion also decreases as the thickness increases as shown in Figure 3.9. The combination of these two signals clearly indicates the presence of a non-perfused layer and its thickness. The two figures illustrate the ability of the analytical model to explain the physical condition accompanied to burning a tissue.

The analytical model shows stability and repeatability in predicting the right thickness of seven different simulated burned layers. The results have been shown to be useful in predicting simulated burn severity and the status of perfusion in damaged tissue. Unlike previous system for burn identification, the present method has multiple measures (thermal resistance and blood perfusion) to quantify the effect of burns on tissue. In addition, these measures can be calibrated relative to known values of the parameters. We will look forward to using the model for living tissue to demonstrate these measurements for actual burns.

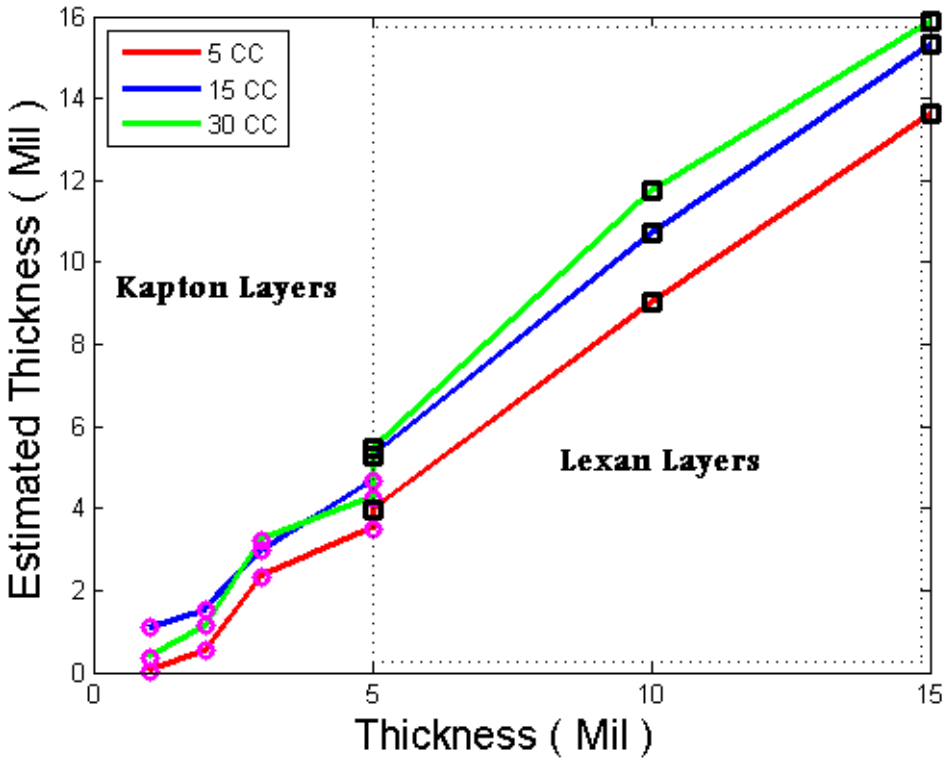

Figure 3.13 Measured burn depth

3.6 CONCLUSIONS

The experimental thermal measurements on phantom tissue support the ability of the perfusion and thermal resistance probe to predict burn depth. A non-perfused layer at the surface, which simulated a fully non-perfused burned layer of skin, was successfully characterized by interpolating the slope and the y-intersection of a line from measured thermal resistance values. Averaged thermal conductivity and the offset of thermal resistance for each of seven plastic layers were used to obtain the corresponding thicknesses of the simulated burn depth. In addition, three different flow rates were used to demonstrate effects on blood perfusion values. Measurements using multiple placements of the sensor were done to conclude the repeatability of the results, which showed that the method of placing the sensor on the skin can be an important factor for clinical applications. The values of thermal resistance and blood perfusion clearly indicated that the model is sensitive to the simulated burn severity. The blood perfusion values decreased and the thermal resistance values increased with increasing thickness of the non-perfused layer, which is as expected. The effect of the imposed simulated burns should translate directly to clinical burns to determine the right treatment. Based on these encouraging results, further study will be done with burned skin of living tissue in continuing work to test this new diagnostic tool for medical applications.

3.7 REFERENCES

[3.1] Alkhwaji, A., Vick, B., and Diller, T., "New mathematical model to estimate tissue blood perfusion, thermal contact resistance and core temperature," *Journal of Biomechanical Engineering*, Vol.134, 2012, 081004, pp. 1-8.

[3.2] Jaskille, A. D., Shupp, J., Jordan, M., and Jeng, J. C., "Critical Review of Burn depth Assessment Techniques: Part I. Historical Review," 2009, *Journal of Burn Care & Research*, Vol. 30, pp. 937-947.

[3.3] Renkelska, A., Nowakowski, A., Kaczmarek, M., and Ruminski, J., 2006, "Burn Depths Evaluation Based on Active Dynamic IR Thermal Imaging – A Preliminary Study," *Burns*, Vol. 32, pp. 867-878.

[3.4] Mileski, W. J. L. Atiles, G. Purdue, R. Kagan, J. R. Saffle, D. N. Herndon, D. Heimbach, A. Luterman, R. Yurt, C. Goodwin, J. L. Hunt, 2003, "Serial Measurements Increase the Accuracy of Laser Doppler Assessment of Burn Wounds," *Journal of Burn Care & Rehabilitation*, Vol. 24, pp. 187-191.

[3.5] Jeng, J. C., Bridgeman, A., Shivnan, L, Thornton, P., Alam, H., Clarke, T., Jablonski, K., and Jordan, M., 2003, "Laser Doppler Imaging Determines Need for Excision and Grafting in Advance of Clinical Judgment: A Prospective Blinded Trial," *Burns*, Vol. 29, pp. 665-670.

[3.6] Stewart, C. J., R. Frank, K.R. Forrester, J. Tulip, R. Lindsay, R.C. Bray, 2005, "A comparison of two laser-based methods for determination of burn scar perfusion: Laser Doppler versus laser speckle imaging." *Journal of Burns*, Vol. 31, pp. 744-752.

[3.7] Jaskille, A. D., Ramella-Roman, J., Shupp, J., Jordan, M., and Jeng, J. C., "Critical Review of Burn Depth Assessment Techniques: Part II. Review of Laser Doppler Technology," 2010, Vol. 31, pp. 151-157.

[3.8] Pennes, H. H., 1948, "Analysis of Tissue and Arterial Blood Temperatures in the Resting Human Forearm," J. Appl. Physiol., Vol. 1, pp. 93-122.

[3.9] Vajkoczy, P., H. Roth, P. Horn, T. Lucke, C. Taumé, U. Hubner, G.T. Martin, C. Zappletal, E. Klar, L. Schilling, P. Schmiedek, 2000, "Continuous Monitoring of Regional Cerebral Blood Flow: Experimental and Clinical Validation of a Novel Thermal Diffusion Microprobe," *Journal of Neurosurgery*," Vol. 93, pp. 265-274.

[3.10] Khot. M. B., P. K. M. Maitz, B. R. Phillips, H. F. Bowman, J. J. Pribaz, D. P. Orgill, 2005, "Thermal Diffusion Probe Analysis of Perfusion Changes in Vascular Occlusions of Rabbit Pedicle Flaps," *Plastic Reconstructive Surgery.*, Vol. 115, No. 4, pp. 1103-1109.

[3.11] Maitz, P. K. M, M. B. Khot, H. F. Mayer, G. T. Martin, J. J. Pribaz, H. F. Bowman, D. P. Orgill, 2005, "Continuous and Real-Time Blood Perfusion Monitoring in Prefabricated Flaps," *Journal of Reconstructive Microsurgery.* Vol. 20, No. 1, pp. 35-41.

[3.12] Ricketts, P. L., Mudaliar, A. V., Ellis, B. E., Pullins, C. A., Meyers, L. A., Lanz, O. I., Scott, E. P., and Diller, T. E., 2008, "Non-Invasive Blood Perfusion Measurements Using a Combined Temperature and Heat Flux Probe," *International Journal of Heat and Mass Transfer*, Vol. 51, pp. 5740-5748.

[3.13] Mudaliar, A. V., Ellis, B. E., Ricketts, P. L., Lanz, O. I., Scott, E. P., and Diller, T. E., 2008, "A Phantom Tissue System for the Calibration of Perfusion

Measurements," *ASME Journal of Biomechanical Engineering*, Vol. 130, No. 051002.

[3.14] Mudaliar, A. V., Ellis, B. E., Ricketts, P. L., Lanz, O. I., Lee, C. Y., Diller, T. E., and Scott, E. P., 2008, "Non-invasive Blood Perfusion Measurements of an Isolated Rat Liver and Anesthetized Rat Kidney," *ASME Journal of Biomechanical Engineering*, Vol. 130, No. 061013.

[3.15] Mudaliar, A. V., Ellis, B. E., Ricketts, P. L., Lanz, O. I., Lee, C. Y., Diller, T. E., and Scott, E. P., 2008, "Non-invasive Blood Perfusion Measurements of an Isolated Rat Liver and Anesthetized Rat Kidney," *ASME Journal of Biomechanical Engineering*, Vol. 130, No. 061013.

[3.15] Diller, K. R., "Modeling of Bioheat Transfer Processes at High and Low Temperatures," *Advances in Heat Transfer*, Vol. 22, 1992, 157-357.

[3.16] Wissler, E. H, "Pennes' 1948 Paper Revisited," *Journal of Applied Physiology*, Vol. 85, 1998, pp. 35-41.

[3.17] GE Structured Products, LEXAN 9034 Product Data Sheet, http://www.associatedplastics.com/forms/pc_lexan_9034.pdf

[3.18] Ewing, J., Gifford, A., Hubble, D., Vlachos, P., Wicks, A., and Diller, T., "A Direct-Measurement Thin-Film Heat Flux Sensor Array," *Measurement Science and Technology*, Vol. 21, 2010, 105201, pp. 1-8.

[3.19] Jacquot, A., Lenoir, B., Dauscher, A., Stölzer, M., and Meusel J. , "Numerical simulation of the 3w method for measuring the thermal conductivity," *Journal of Applied Physics*, Vol. 91, 2002, pp. 4733-38.

Chapter 4

Monitoring and quantifying burn wounds on pig skin using thermal measurements

4.1 Abstract

A new thermal method for detecting burn severity or monitoring burn wound healing is presented. The thermal measurement method avoids the need for introducing any substance or radiation to monitor blood perfusion or detect the depth of burnt tissue. The method of predicting and monitoring burns was tested experimentally by implementing four different burn severities on two pigs and monitoring the burns over five days. Averaged estimated thermal resistance and blood perfusion values were used to detect burn depth from thermal measurements. A damage function was introduced to illustrate thus burns which cause third degree burns. The 20 and 75 seconds burns were quantified as third degree burns. The laboratory measured non-perfused layers calibrates very well with the estimated burn depth from the perfusion-thermal resistance probe. This paper has demonstrated the ability of a perfusion-thermal resistance probe to characterize burn severity.

4.2 Introduction

Treating burn wounds requires sufficient knowledge about the burn severity. A burn wound is categorized as first, superficial second, deep second or third degree [4.5]. The healing process is reported to be between 14 to 21 days after which an excision and grafting surgery is required [4.5]. A false prediction of the burn depth causes needless surgery or increased hospital accommodation costs [4.5]. This brings an additional medical significance to this work to decrease the time required to detect the need of surgery.

Burn assessment researchers have developed many invasive and non-invasive techniques to detect burn depths. Invasive techniques are accompanied with either pain or risk of bacterial infection. VACUETTE [4.19] venous blood sampling device is an invasive device that uses blood perfusion samples to detect burns. Non-invasive techniques range from visual inspection to the use of any of the existing imaging techniques such as thermography (IR), ultrasonography (USG), laser Doppler imaging (LDI) and indocyanine green fluorescence (ICG) [4.6]. However, none of these techniques has been broadly accepted as a standard diagnostic tool for burns [4.6]. Non-invasive medical diagnostic methods to predict burn depths are designed to use either information about temperature distribution or the presence of blood perfusion in the burnt area [4.5-4.10]. Non-invasive methods such as, radioactive isotopes, or indocyanine green fluorescence (ICG) requires injecting the patient intravenously with radioactive phosphorus [4.5, 4.20]. The process requires repeatedly imaging the uptake and clearance of the dye-marker from the burnt region [4.20]. The vital dye substance such as tetracycline illuminates the burnt area with ultraviolet light, which helps to detect the presence of the dye at specific depths [4.5]. Thermography or IR thermal imaging techniques are either static or dynamic. In the static IR method, temperature measurements cannot reflect perfusion because it is operating at steady state [4.5, 4.6], while the dynamic method involves introducing a thermal event (external thermal excitation) followed by measurements of transient temperature on the burnt surface. The

temperature distribution from the dynamic IR method helps to create an image which describes blood perfusion in the burnt area [4.6]. IR methods are still under research and blood perfusion values are not connected to heat flux from the burnt surface. LDI methods operates on the principle that laser light reflected by the skin undergoes a frequency shift that is correlated by the movement of red cells [4.21].

Detecting the histology of a burn using any of the imaging techniques beside, Ultrasound and laser Doppler Imaging are expensive and have risks of developing cancer, since pre-injured regions are more common to receive mutation. Most of the imaging techniques collect data to map blood perfusion distribution through a burnt tissue. Only LDI [4.8] can characterize burns closer to the surface, other imaging techniques detect perfusion in deeper layers only.

Penetration of the used energy waveform reflects the burn depth. The strength of the reflected portion of the energy source indicates sophisticate information about blood perfusion [4.5-4.10]. Imaging methods are accomplished with receiving the reflected energy after the attenuation made by blood perfusion and different tissue layers. Using additional substance to either defuse through burnt region or penetrating energy with specific wavelength to defuse through damaged tissue might disturb the healing process. There are no quantification and calibrating results from imaging measurements or vital dye method, they have risk factor and require extra clinical judgment.

The usage of heat flux measurements in burn assessments is a new method to diagnose a burnt area, where blood perfusion information could be estimated from the perfusion probe [4.15-4.17]. Since burn degree effects perfusion which results in changes in temperature and heat transfer through burnt tissue. Using thermal measurement, we built analytical model uses thermal measurements to monitor and detect burnt area. In our previous publication, we proved the sensitivity and repeatability of the thermal measurements using perfusion-thermal resistance probe "phantom tissue" in characterizing simulated burns, the model successfully was able to classify thicknesses and thermal properties of different layers of Kapton and Lexan [4.2]. Transportation of heat and perfusion were modeled mathematically using 1D bioheat equation by thermal resistance and blood perfusion.

This work is to quantify different burns on two pigs. The hypotheses of this experiment are to detect the third degree burn from four different burn times, to connect blood perfusion and thermal resistance of the burnt tissue to better illustrate the healing direction, and to minimize the diagnostic time of self-healing.

4.3 Experimental Method

The general study design of this project is a common one used for evaluation of burn injury and has frequently been used for studies in our laboratory. Swine are used since their skin is similar to humans. By exposing the animals skin to brass cylinders of known temperature for a given time period, the depth of burn may be controlled. Four different depths of burn will be evaluated to determine the ability of the different devices to evaluate burn depth and to determine whether it is better than clinical evaluation to predict an endpoint of healing at two weeks.

Eight areas for wounds will be drawn on each side of the anesthetized animal (8 total wounds per pig and 8 control sites) that measure approximately 3 cm diameter. Marked sites will be assigned to one of four treatment groups (i.e. two test groups per

animal) or as a control adjacent to the burn site with an intervening 4 cm gap of normal skin. Wounds will be made in the marked areas with a brass cylinder heated to 100 degrees Centigrade. Four different contact times will allow for four different depths of wounds. Contact times will be 3 seconds, (superficial partial thickness), 12 second (intermediate partial thickness), 20 second deep partial thickness, and 75 second (full thickness). Within the first 10 minutes after injuring, standardized digital photos, B-mode high resolution ultrasonography, heat flux blood perfusion, scanning laser doppler and Periodic camera photos will be obtained. All measurements will be repeated at 1 hour and at 24, 72, and 120 hours. Subsequent photographic evaluations only will be obtained at 7 days and 14 days. Each wound will be covered with Acticoat® (Westaim Laboratories, Edmonton, Alberta) dressing material and an occlusive dressing placed on top. The pigs will then be wrapped to prevent the dressings from falling or being rubbed off by the animal using a technique previously developed in our lab. The animals will be examined once daily for overall condition. Dressings will be changed with each early evaluation or when standardized digital photos are obtained. At 2 weeks animals will be euthanized by lethal overdose with pentobarbital after collecting the last data point.

4.4 Measurement Method & Mathematical Model

A combined heat flux and temperature sensor (CHFT) is used to collect temperature and heat flux measurements [4.1] at the tissue surface. The heat flux is measured with a BF-02 heat flux gauge from Vatell Corp. It produces a voltage signal directly proportional to the heat flux using a nickel-copper differential thermopile between the CHFT chip faces with a calibration factor of 2.1 mV/(W/cm^2). The temperature sensor on the CHFT is a type-K foil thermocouple mounted on the sensor surface next to the tissue. The top face of the CHFT is exposed to a compressed air source which produces cooling from nine air jets exiting from 0.37 mm holes. Figure 4.1 illustrates the CHFT sitting above the tissue surface under the air jets. The measurement begins with the sensor sitting at thermal equilibrium on the tissue. The thermal event begins when the jets are activated causing a large change in the heat flux.

Three CHFT sensors were used to simultaneously collect temperature and heat flux measurements. One of the three sensors was used as a control by attaching it to the unburned surface next to the burns. Amplifiers and a DAQ system were used to collect data with 10 samples per second. Results were averaged for each second. A mathematical model is used to estimate the core temperature, blood perfusion and thermal resistance from the steady state and transient data.

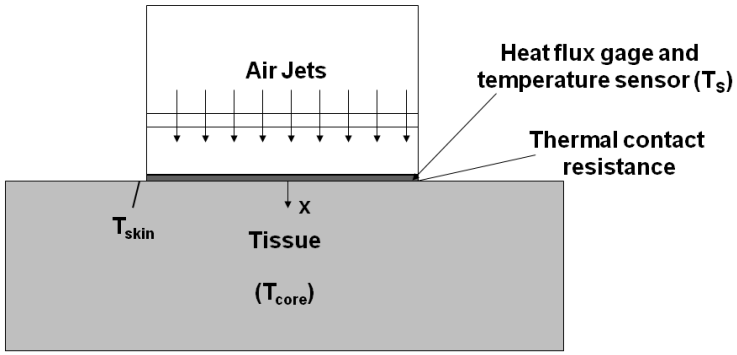

Figure 4.1 CHFT mounted on the tissue

The Pennes equation [4.11] is used to model the conduction heat transfer process and the effects of perfusion in the tissue.

$$(\boldsymbol{\rho c})_t \frac{\partial \boldsymbol{\theta}}{\partial \boldsymbol{t}} = \boldsymbol{k_t} \frac{\partial^2 \boldsymbol{\theta}}{\partial \boldsymbol{x^2}} - (\boldsymbol{\rho c w})_b \boldsymbol{\theta} \tag{4.1}$$

where $\theta(x,t) = T(x,t) - T_{core}$ is the temperature difference between tissue and the entering blood at the core temperature. Subscript b is for blood properties while subscript t represents the tissue properties. The assumption is that ρ, c and k, which are the density, thermal capacity and thermal conductivity of both tissue and blood are assumed to have the same average values k = 0.5 W/m-K, ρ = 1050 kg/m^3, and c = 3800 J/kg-K. The blood perfusion is w_b .

The process of developing the analytical solution was described in detail in reference [4.1]. Temperature measurements are used at the surface boundary (equation 4.2), while the boundary in the tissue is specified using equation 4.3

$$-\boldsymbol{k} \frac{\partial \boldsymbol{\theta}}{\partial \boldsymbol{x}}|_{\boldsymbol{x=0}} = \frac{\mathbf{1}}{\boldsymbol{R''}} \left(\boldsymbol{\theta_S(t)} - \boldsymbol{\theta(0,t)}\right) \tag{4.2}$$

$$\frac{\partial \boldsymbol{\theta}}{\partial \boldsymbol{x}}|_{\boldsymbol{x\to\infty}} = \mathbf{0} \tag{4.3}$$

where R'' is the thermal resistance between the sensor and tissue, and the s-subscript stands for the sensor. The complete analytical solution is developed from the combination of the steady-state solution before the thermal event and the transient solution during the thermal event.

The measured sensor temperature profile is modeled as a series of steps, where H(t) is the step function which is defined as

$$\boldsymbol{H(t-t_n)} = \begin{bmatrix} \mathbf{0}, & \boldsymbol{t < t_n} \\ \mathbf{1}, & \boldsymbol{t \geq t_n} \end{bmatrix} \tag{4.4}$$

where each step corresponds to a temperature in the digital series

$$\boldsymbol{\theta_S(t)} = \boldsymbol{\theta_S(0)} + \sum_{\boldsymbol{n=1}}^{\boldsymbol{N_{max}}} \Delta \boldsymbol{\theta_{S,n}} \,.\, \boldsymbol{H(t-t_n)} \tag{4.5}$$

and $\theta_{S,n}$ represents the steady-state temperature difference between the sensor and core at any n-step, while $\theta_{S,0}$ is before the thermal event is initiated. The solution for the transient heat flux was developed using the Green's function approach.

$$\boldsymbol{\theta_T(0,t)} = \frac{\mathbf{1}}{\boldsymbol{\rho c}} \int_{\boldsymbol{t_0=0}}^{\boldsymbol{t}} \frac{\mathbf{1}}{\boldsymbol{R''}} \left(\boldsymbol{\theta_S(t_0)} - \boldsymbol{\theta_{S,0}}\right) \boldsymbol{G(0,t|0,t_0)} \boldsymbol{dt_0} \tag{4.6}$$

$$\boldsymbol{q_T} = \frac{\boldsymbol{\theta_T(0,t)} - \boldsymbol{\theta_S(t)}}{\boldsymbol{R''}} \tag{4.7}$$

The Green's function at the surface is

$$G(0,t|0,t_0) = \frac{2\,e^{-w_b(t-t_0)}}{\sqrt{4\pi\alpha(t-t_0)}} - \frac{erfc\left(\frac{\sqrt{\alpha(t-t_0)}}{k\,R''}\right) e^{\left(\frac{1}{(k\,R'')^2}\alpha - w_b\right)(t-t_0)}}{k\,R''} \quad (4.8)$$

The initial heat flux was developed using the steady state version of equation 4.1. The initial heat flux is used to estimate the core temperature in $\theta_{S,0}$ [1].

$$q_i = -k\,\theta_{S,0}\left[\frac{\sqrt{w_b/\alpha}}{1 + R''k\sqrt{w_b/\alpha}}\right] \quad (4.9)$$

By superposing the initial and transient solutions

$$q_a = q_i + q_T \quad (4.10)$$

The analytical solution was validated versus 1D finite difference and 2D cylindrical coordinate finite difference solutions [4.1]. Figure 4.2 illustrates typical measurements and fit between analytical and measured heat flux. The difference between the sensor and skin temperatures represents the thermal contact resistance between the sensor and skin. The thermal resistance will appear to be higher when burned tissue is present.

Core temperature, thermal resistance, and blood perfusion are the three unknown parameters which are obtained by fitting measured and analytical heat fluxes. The search uses closed predetermined domains for all possible values of both blood perfusion and thermal resistance. The search inside the two domains is done by alternating the search direction and narrowing the search around both domains. Each set of two parameters applied to the initial analytical heat flux with the steady-state solution to evaluate the core temperature. The transient analytical solution is then compared to the measured heat flux during the thermal event. The difference between the measured and analytical values is used to form the average square root of the squared residual. The minimum value of this quantity specifies the best fit and the optimum set of parameters [4.1].

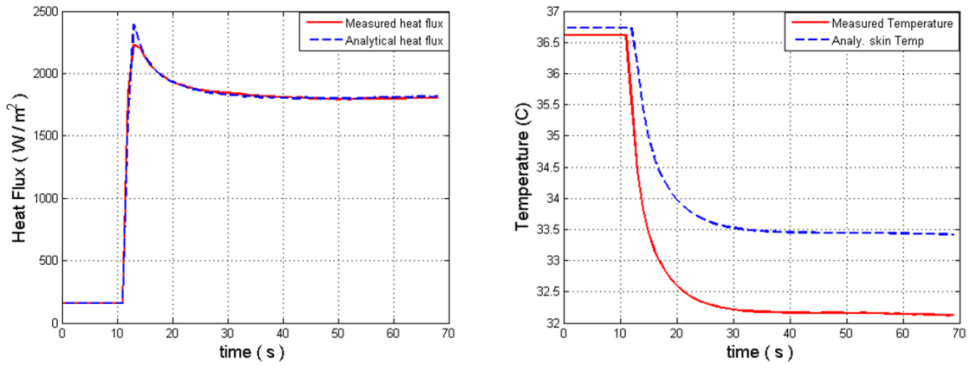

Figure 4.2 fitting analytical and measured heat fluxes

4.5. Quantifying the degree of damage to the tissue (damage function)

A finite difference model to calculate temperature distribution, which is resulted from burning the pig tissue using the brass cylinder at 100C^{o} for each burn time, was created to calculate the penetration depth of damages through tissue for each burn time. A damage function was developed by Moritz and Henriques [4.4], where thermal damage is approximated using a temperature-dependent rate process, similar to other chemical kinetic processes. An Arrhenius equation is used to quantify this process

$$\frac{d\Omega(x,t_{burn})}{dt} = A\exp(-\frac{G}{R\,T(x,t)}) \qquad (4.11)$$

where:
$\Omega(x,t)$ = a damage function
G = an activation energy for the reaction (G = 62,700 J/mol)
T(x,t) = absolute temperature of a local tissue (calculated from the heat equation at the basal layer)
R = Gas constant (8.36 J/°C/mol)
A = Constant (3.1×10^{98} sec^{-1})

The total thermal damage over the time interval from t_o to t_{burn} is

$$\Omega(x,t_{burn}) = \int_{t_0}^{t_{burn}} A\, e^{-G/R\,T(x,t)}\, dt \qquad (4.12)$$

A finite-difference solution uses an initial temperature of 35°C followed by applying the burn from a cylinder brass at 100^{o}C at the surface which has the averaged estimated values at rest of blood perfusion, thermal resistance and core temperature of, $w_b = 0.003$ ml ml^{-1}s^{-1}, R″ $= 0.003$ m^{2}K/W and $T_{core} = 38$ ℃ respectively.

The resulting tissue temperature distribution T(x,t_{burn}) from the finite-difference solution for each of the four burns was used to evaluate the damage function from equation 4.12. The Matlab function Trapz was used to evaluate the integral. A damage function value of 10^4 was used as the criteria for a third degree burn [4.3]. Figure 4.3 illustrates the results of the damage function on the Y-axis versus the corresponding depth L_t (mm). It is clear that burn times of 3 and 12 seconds are not a third degree burn. However, burn times of 20 and 75 seconds are third degree burns. The corresponding calculated burn depths for 20 and 75 seconds were $L_{20} = 0.14$ mm and $L_{75} = 1.3$ mm repspectively.

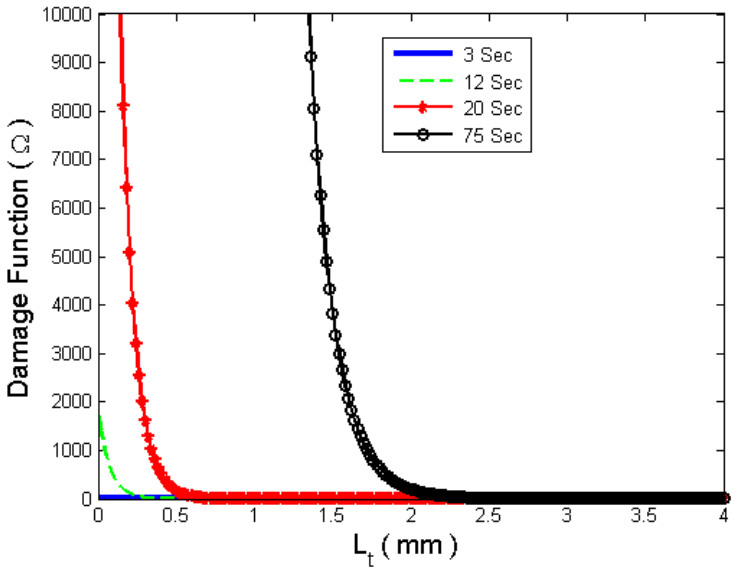

Figure 4.3 Damage function versus burn depth

4.6 Results

A total of 390 tests were collected on the two pigs. One out of every six tests was a control taken on normal tissue beside the burn. After parameter estimation was performed some of the tests were discarded because one of the estimated values of blood perfusion, thermal contact resistance or core temperature was outside the limits of reasonable values. Usually this was because of a problem in the process of manually placing the probe on the tissue or electrical noise in the data acquisition. A total of 342 tests were used for the final burn evaluations.

Blood perfusion w_b and thermal resistance R'' are the two estimated parameters used to characterize and quantify burn severity. Average of the core temperature was around 38℃. Figure 4.4 illustrates the average results of blood perfusion (a) and thermal resistance (b) as a function of the implemented burn time (burn severity). Zero burn time represents the control with no burn. The time after the burn is shown as four different symbols and lines, representing one hour, 24 hours, 72 hours and 120 hours after the burn. To demonstrate the deviation of blood perfusion and thermal resistance from the average values, a ninety-five percent confidence interval is shown with each value in the figure. One hour following the burn the blood perfusion has decreased and the thermal resistance has increased for all of the burns except for the lightest, 3 second burn. After 24 hours, however, the blood perfusion has increased and the thermal resistance has dropped, indicating that the blood is flowing near the surface. The highest blood perfusion is for the 3 second case, showing the strongest inflammation response.

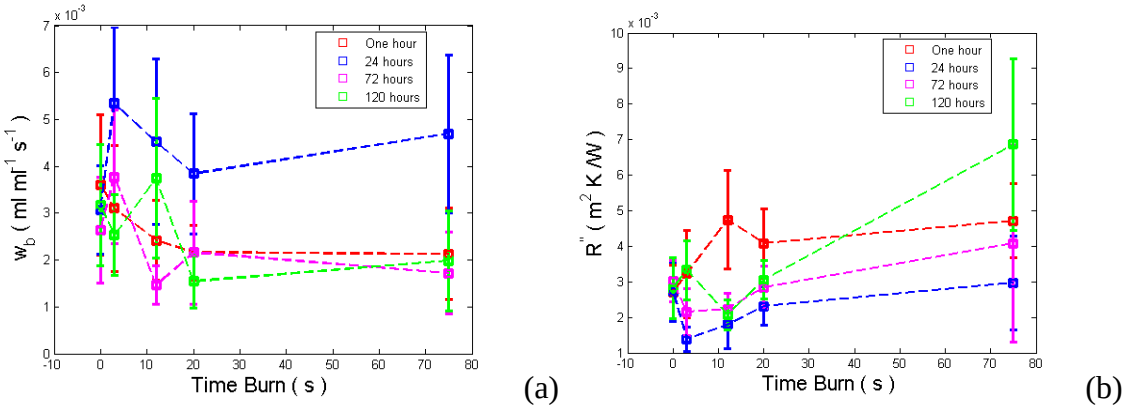

Figure 4.4 Blood perfusion and thermal resistance averaged values versus burn time

To better visualize the changes with time after the burn, Figure 4.5 shows only a portion of the results as a function of the time after the burn, with the severity of the burn indicated by three different symbols and lines. Only the values for the undamaged control, 3 second burns and 75 second burns are shown. The control value of blood perfusion (a) and thermal resistance (b) remain nearly constant. The blood perfusion increases at 24 hours and then decreases. The thermal resistance does the opposite. The blood perfusion values for the 75 second burn are always less than the 3 second burn, while the thermal resistance values are always higher for the 75 second burn. The trends are clear. After 120 hours the 3 second burn is within the uncertainty of the control tissue (no burn). As would be expected of tissue with a layer of dead material on top, the 75 second burn has lower blood perfusion and higher thermal resistance.

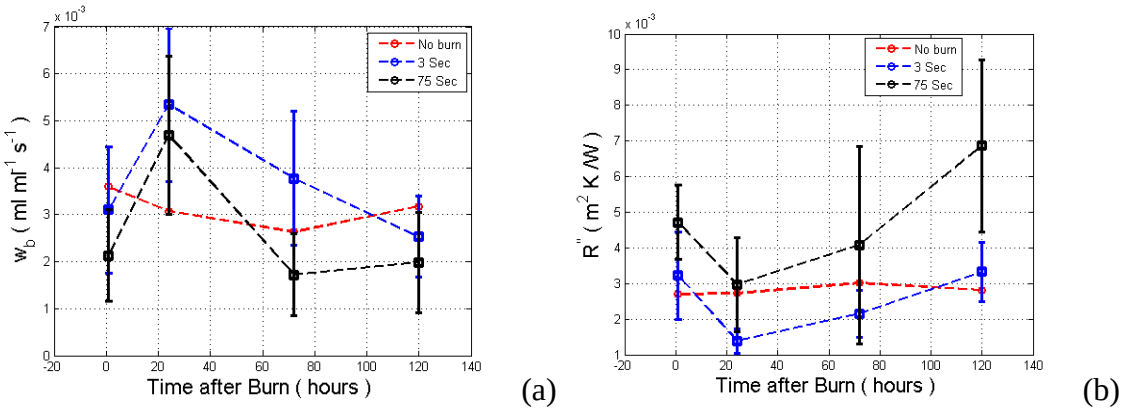

Figure 4.5 Blood perfusion and thermal resistance averaged values versus burn time

The thermal resistance is in general composed of two resistances in series. The first is the contact resistance between the CHFT sensor and the surface of the tissue, R_0''. The second is the resistance of a non-perfused layer, L/k, where L is the tissue thickness and k is the tissue thermal conductivity [4.2].

$$R''(L) = R_0'' + \frac{L}{k} \tag{4.13}$$

If it is assumed that severely burned tissue does not have any perfusion, measurements of the thermal resistance can be used to estimate the thickness of this layer.

$$\boldsymbol{L = k * \left(R'' - R_0''\right)} \qquad \textbf{(4.14)}$$

A previous study [4.2] has shown the validity of this approach using plastic layers to simulate non-perfused tissue. The perfusion and thermal resistance sensor was successfully used to estimate the thickness of the non-perfused layer based on the thermal measurements with the CHFT. The value of R_0'' is assumed to be equal to the thermal resistance for the healthy control tissue. The thickness of the burned tissue can then be estimated from equation 4.15 using the corresponding thermal resistance values for that tissue as a function of time after the burn.

Figure 4.6 illustrates the estimated burn depth from thermal measurements using the averaged thermal resistance. The burn times have been converted to the corresponding depth causing third degree burn $\Omega = 10^4$ from Figure 4.3. Each thickness is plotted on a separate axis. Notice, there are no corresponding depth for burn times of 3 and 12 seconds, because there is no third degree burn. The predicted thickness is between that measured thermally at 72 and 120 hours.

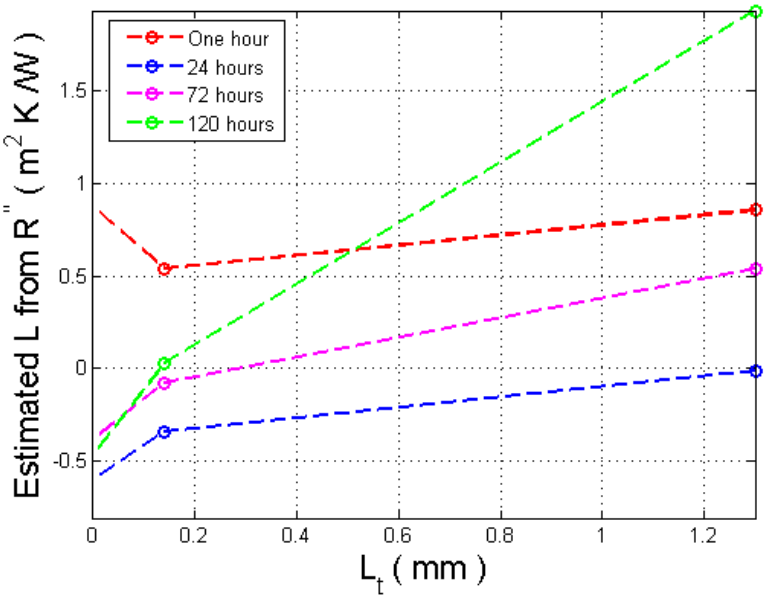

Figure 4.6 Estimated burn depth at each monitored time

To combine the effects shown by changes in both the blood perfusion and the thermal resistance, the burn factor is introduced to better describe the simultaneous changes in both variables

$$BF = \left[\frac{w_{b,0}}{w_{b,burn}}\right] \times \left[\frac{R''_{burn}}{R_0''}\right] \qquad (4.15)$$

where $w_{b,0}$ is the local blood perfusion of a healthy tissue with no burn imposed, $w_{b,burn}$ is the local blood perfusion of the burned tissue, $R_0^{"}$ is the local thermal resistance of a healthy tissue with no burn imposed, and $R_{burn}^{"}$ is the local thermal resistance of the burned tissue. Because the blood perfusion for burned tissue decreases and the apparent thermal resistance increases as shown in Figures 4.4 and 4.5, the values change in opposite directions. The burn factor therefore uses the inverse of the blood perfusion ratio, which combines these effects to increase for burned tissue.

Figure 4.7 shows the calculated values of the burn factor. It is plotted versus the burn times in Fig. 4.7a and versus the time after burn in Fig. 4.7b. The signal for the 20s and 75s burns is very strong at the 1 hour and 120 hour times after burn. It appears that there is a healing response of the tissue at 24 hours post burn for all of the burn severities. The 20s and 75s burns then become progressively worse, indicating that they are not healing. Therefore, burn factor *BF* appears to be a good indicator of the direction of the tissue response. Notice that for any reversible damage, there will be not a large effect of the thermal resistance and the ratio of blood perfusion will reflect the activation of the inflammatory system to pump more blood to the tissue. Conversely, with severe burns the blood perfusion ratio will be deactivated and the thermal resistance ratio increases. The 12s burn as seen in Fig. 4.7b does not have a clear signal and may actually be healing at longer times. Burn times below 20 seconds have values of burn factor closer to one with some deviation related to responses to the inflammatory system.

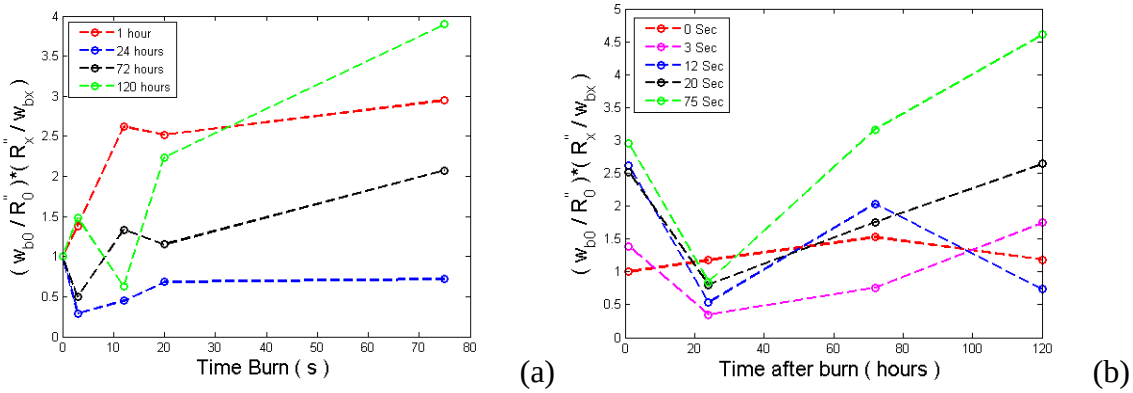

Figure 4.7 Burn factor for different burn times and time after burn

To further illustrate the value of the burn factor, it was applied to a set of experiments using a simulation of burns using a phantom tissue system. Dead tissue was simulated with a layer of plastic over a perfused porous media simulating healthy tissue. Three different flow rates were used for the perfusion and a range of plastic thicknesses. The results are shown in Figure 4.8 with the burn factor as a function of the layer thickness for the three flow rates. The flow rate has little influence on the results, but the burn factor shows a strong function of the layer thickness. Values are comparable to those in this paper for the pig burns. The thickness values are smaller, but the thermal conductivity of the plastic is about one-half that of tissue. In addition, there is a sharp demarcation from the plastic layer with zero perfusion to the fully perfusion phantom tissue. In real tissue there would not be such a sharp demarcation.

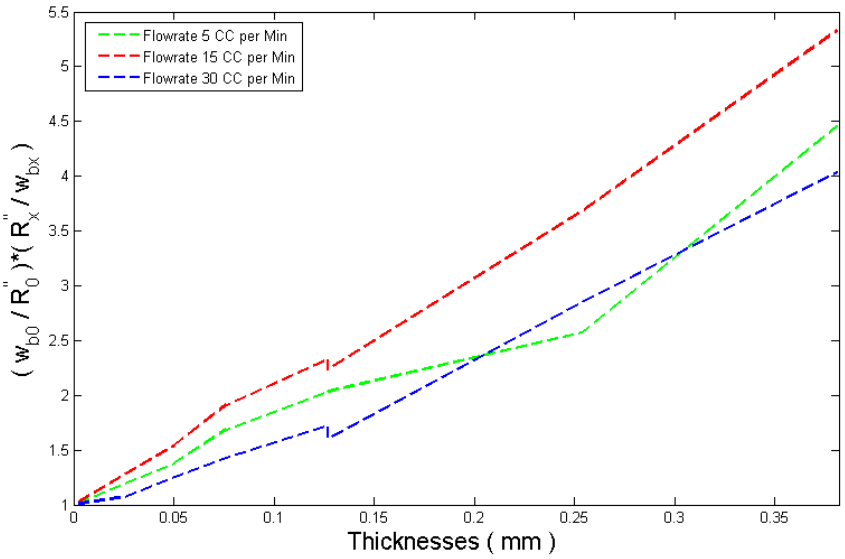

Figure 4.8 Burn factor applied to phantom tissue experiments

4.7 Conclusions

The pig experiment burn results support the ability of the new perfusion-thermal resistance system to predict burn depth from thermal measurements. Four different burn times were implemented on the animal skin to give a range of burn severity. Results illustrate the ability of the method to quantify burns at each implemented burn time, using averaged estimated values of thermal resistance and blood perfusion. Burn depths were quantified from the thermal resistance measurements on healthy and burned tissue. The values gave a reasonable match with the predicted burn depths from estimates of the damage factor and laboratory measured thicknesses of 20 and 75 burn times from the surgeon with values of 0.3 mm and 2 mm, respectively. The surgery was done without shaving the pig's hair, which might explain why the control value of thermal resistance was slightly higher than human values. The burn factor was introduced as a more sensitive quantitative indicator of the tissue damage and healing responses. Values of the bun factor showed that the model is sensitive to the different burn severity and the corresponding inflammatory responses.

4.8 References

[4.1] Alkhwaji, A., Vick, B., and Diller, T., "New mathematical model to estimate tissue blood perfusion, thermal contact resistance and core temperature," *Journal of Biomechanical Engineering*, Vol.134, 2012, 081004, pp. 1-8.

[4.2] Abdusalam Alkhwaji, Brian Vick, Tom Diller, "Modelling and Estimating Simulated Burn Depth Using the Perfusion and Thermal Resistance Probe," Journal of Medical Device, under review.

[4.3] Diller, K.R., Modeling of Bioheat Transfer Processes at High and Low Temperatures, Advances in Heat Transfer 22, 1992, 157-357.

[4.4] Moritz, A. R., Henriques F. C., Jr., "Studies of thermal injury: II. The relative importance of time and surface temperature in the causation of cutaneous burns." American Journal of Pathology, 1947, 23: 695-720.

[4.5] Jaskille, A. D., Shupp, J., Jordan, M., and Jeng, J. C., "Critical Review of Burn depth Assessment Techniques: Part I. Historical Review," 2009, *Journal of Burn Care & Research*, Vol. 30, pp. 937-947.

[4.6] Renkelska, A., Nowakowski, A., Kaczmarek, M., and Ruminski, J., 2006, "Burn Depths Evaluation Based on Active Dynamic IR Thermal Imaging – A Preliminary Study," *Burns*, Vol. 32, pp. 867-878.

[4.7] Mileski, W. J. L. Atiles, G. Purdue, R. Kagan, J. R. Saffle, D. N. Herndon, D. Heimbach, A. Luterman, R. Yurt, C. Goodwin, J. L. Hunt, 2003, "Serial Measurements Increase the Accuracy of Laser Doppler Assessment of Burn Wounds," *Journal of Burn Care & Rehabilitation*, Vol. 24, pp. 187-191.

[4.8] Jeng, J. C., Bridgeman, A., Shivnan, L, Thornton, P., Alam, H., Clarke, T., Jablonski, K., and Jordan, M., 2003, "Laser Doppler Imaging Determines Need for Excision and Grafting in Advance of Clinical Judgment: A Prospective Blinded Trial," *Burns*, Vol. 29, pp. 665-670.

[4.9] Stewart, C. J., R. Frank, K.R. Forrester, J. Tulip, R. Lindsay, R.C. Bray, 2005, "A comparison of two laser-based methods for determination of burn scar perfusion: Laser Doppler versus laser speckle imaging." *Journal of Burns*, Vol. 31, pp. 744-752.

[4.10] Jaskille, A. D., Ramella-Roman, J., Shupp, J., Jordan, M., and Jeng, J. C., "Critical Review of Burn Depth Assessment Techniques: Part II. Review of Laser Doppler Technology," 20010, Vol. 31, pp. 151-157.

[4.11] Pennes, H. H., 1948, "Analysis of Tissue and Arterial Blood Temperatures in the Resting Human Forearm," *J. Appl. Physiol.*, Vol. 1, pp. 93-122.

[4.12] Vajkoczy, P., H. Roth, P. Horn, T. Lucke, C. Taumé, U. Hubner, G.T. Martin, C. Zappletal, E. Klar, L. Schilling, P. Schmiedek, 2000, "Continuous Monitoring of Regional Cerebral Blood Flow: Experimental and Clinical Validation of a Novel Thermal Diffusion Microprobe," *Journal of Neurosurgery*," Vol. 93, pp. 265-274.

[4.13] Khot. M. B., P. K. M. Maitz, B. R. Phillips, H. F. Bowman, J. J. Pribaz, D. P. Orgill, 2005, "Thermal Diffusion Probe Analysis of Perfusion Changes in Vascular Occlusions of Rabbit Pedicle Flaps," *Plastic Reconstructive Surgery.*, Vol. 115, No. 4, pp. 1103-1109.

[4.14] Maitz, Peter K. M, M. B. Khot, H. F. Mayer, G. T. Martin, J. J. Pribaz, H. F. Bowman, D. P. Orgill, 2005, "Continuous and Real-Time Blood Perfusion

Monitoring in Prefabricated Flaps," *Journal of Reconstructive Microsurgery.* Vol. 20, No. 1, pp. 35-41.

[4.15] Ricketts, P. L., Mudaliar, A. V., Ellis, B. E., Pullins, C. A., Meyers, L. A., Lanz, O. I., Scott, E. P., and Diller, T. E., 2008, "Non-Invasive Blood Perfusion Measurements Using a Combined Temperature and Heat Flux Probe," *International Journal of Heat and Mass Transfer*, Vol. 51, pp. 5740-5748.

[4.16] Mudaliar, A. V., Ellis, B. E., Ricketts, P. L., Lanz, O. I., Scott, E. P., and Diller, T. E., 2008, "A Phantom Tissue System for the Calibration of Perfusion Measurements," *ASME Journal of Biomechanical Engineering*, Vol. 130, No. 051002.

[4.17] Mudaliar, A. V., Ellis, B. E., Ricketts, P. L., Lanz, O. I., Lee, C. Y., Diller, T. E., and Scott, E. P., 2008, "Non-invasive Blood Perfusion Measurements of an Isolated Rat Liver and Anesthetized Rat Kidney," *ASME Journal of Biomechanical Engineering*, Vol. 130, No. 061013.

[4.18] Jacquot, A., Lenoir, B., Dauscher, A., Stölzer, M., and Meusel J. , "Numerical simulation of the 3w method for measuring the thermal conductivity," Journal of Applied Physics, Vol. 91, 2002, pp. 4733-38.

[4.19] Muhammad Javed, Kayvan Shokrollahi, "VACUETTE for burn depth assessment – A simple and novel alternative use for a ubiquitous phlebotomy device," Burns, 38, 2012, 1084-1085

[4.20] J. M. Still, E.J. Law, K. G. Klavuhn, T.C. Island, J. Z. Holtz, "Diagnosis of burn depth using laser-induced indocyanine green fluorescence: a preliminary clinical trial," Burns, 27, 2001, 364-371

[4.21] Khanh Nguyen, Diane Ward, Lawrence Lam, Andrew J. A. Holland, "Laser Doppler Imaging prediction of burn wound outcome in children: Is it possible before 48 h?," Burns, 36, 2010, 793-798

Chapter 5 Conclusions and Recommendations

5.1 Conclusions

The new mathematical model that uses thermal measurements to estimate burn severities gave promising results which match very well with the clinical evaluations. The method combines perfusion and thermal resistance signals to better predict burn severities. This study demonstrates that the method is useful in monitoring the healing process and for discovering the inflammation process associated with the healing process, which was detected clearly after 24 hours. The burn factor is a new concept to study inflammation associated with burn on an animal model was introduced. The experimental and computational results match with measured third degree burn thicknesses. The method is not expensive; therefore, this method could be transferred to portable devices useful for burn detection. Overall the method was shown to be useful in evaluating burn severity

5.2 Recommendation

More evaluation time is required to detect burn severities earlier. The time after burns was evaluated at 24, 72, and 120 hours. The time required to detect third degree burn around 72 hours after the burn. Therefore, I suggest more measurements between 24 hours and 72 hours. Measurement is very sensitive to the sensor sitting; therefore, I suggest using intermediate liquid to insure perfect attachment between sensor and skin.

Appendixes

Appendix A – Finite Difference

Finite difference solutions of the 1D-Cartesian coordinate and 2D-cylindrical coordinate of the Bioheat equation were used in this research to demonstrate that the 1D-analytical model gives a very good match. The 1D finite-difference model was also used to demonstrate the validity of ignoring thermal capacity in the resistance layer in the analytical model.

(A-1) 1D Finite Difference Derivation

$$k\frac{\partial^2 T}{\partial x^2} - \rho_b C_b w_b (T - T_{core}) = \rho C \frac{\partial T}{\partial t}$$

$\theta = (T - T_{core})$;

$$\frac{\overbrace{k}^{\alpha}}{\rho_b C_b}\frac{\partial^2 \theta}{\partial x^2} - w_b\theta = \frac{\partial \theta}{\partial t}$$

$$\frac{\partial \theta}{\partial t} = \alpha\frac{\partial^2 \theta}{\partial x^2} - w_b\theta$$

Using Crank Nicolson scheme with the assumption that tissue and blood properties are same

$$\frac{\theta_i^{p+1} - \theta_i^p}{\Delta t} = \alpha\left[\frac{\theta_{i+1}^{p+1} - 2\theta_i^{p+1} + \theta_{i-1}^{p+1} + \theta_{i+1}^{p} - 2\theta_i^{p} + \theta_{i-1}^{p}}{2\Delta x^2}\right] - w_b\left(\frac{\theta_i^{p+1} + \theta_i^p}{2}\right)$$

$$\frac{\overbrace{2\Delta x^2}^{\vartheta}}{\alpha\,\Delta t}\left(\theta_i^{p+1} - \theta_i^p\right)$$

$$= \theta_{i+1}^{p+1} - 2\theta_i^{p+1} + \theta_{i-1}^{p+1} + \theta_{i+1}^{p} - 2\theta_i^{p} + \theta_{i-1}^{p} - \frac{\overbrace{\Delta x^2}^{\beta}}{\alpha}w_b\left(\theta_i^{p+1} + \theta_i^p\right)$$

$$(2 - \vartheta + \beta)\theta_i^p - \theta_{i+1}^p - \theta_{i-1}^p = \theta_{i+1}^{p+1} - (2 + \vartheta + \beta)\theta_i^{p+1} + \theta_{i-1}^{p+1}$$

Solving the above equation at both the interior region ($\mathbf{2 \le i \le imax - 1}$) and at the two boundary conditions ($\mathbf{i = 1}$ & $imax$). Thomas algorithm is used to solve the diagonal matrix [b d c].

$$d_i = (2 - \vartheta + \beta)\theta_i^p - \theta_{i+1}^p - \theta_{i-1}^p$$
$$a_i = 1$$
$$b_i = -(2 + \vartheta + \beta)$$
$$c_i = 1$$

(A-2)- 1D Finite difference code

The first-order finite-difference code was used to prove the analytical solution. The above discretization is made for the boundary conditions at i = 1 and i = imax, and solved for the rest of the interior nodes using Thomas algorithm. To use the finite-difference solution, a set of simulated or real temperature data is required to produce temperature distribution of tissue throughout the run time. The important output of the finite-difference model is skin temperature and skin heat flux. Initial temperature is solved using steady-state solution of the 1D-bioheat equation.

```
function 1D_FD()
clear all; close all; clc;

format long
%Transient Bioheat Equation - Finite Difference (FD) Solution
% Maximum space and time step numbers
 imax=120
 load Data.txt;
 y=Data;
 % Tissue Properties
 Ta0=36.61; wb =4.1e-2; Rth0=0.00052;
 u=zeros(imax,nmax); dt=tmax/(nmax-1); t=0:dt:tmax;
 ro=1000; cb=4e3; k=0.5; Gama=k/ro/cb; beta =wb;
%% Non-Dimention Temperature
      um=T0(:)-Ta0;    %  The Skin Non-Dim temp.



%% Initial Solution
for ih=1:imax
   u(ih,1)=um(1)*(1/(1+Rth*k*sqrt(beta/Gama)))*exp(-sqrt(beta/Gama)*LL(ih));
end

 for n=1:nmax-1
%%%%%%%%%%%%%%%%%%%%%%%%%%%%%%%%%%%%%%%%%%%%%%%%%%%%%%%%%%%%%%%%%%%%%%%%%%%%%%%%
% Finite differences
  dL2=dL*dL; dL2dt=dL2/dt;
  %%%%%%%%%%%%%%%%%%%%%%%%%%%%%%%%%%%%%%%%%%%%%%%%%%%%%%%%%%%%%%%%%%%%%%%%%%%%%%%
        b(1)=(2*ro*cb*dL/dt)  + (k/dL) + (1/Rth) ;
        c(1)=-k/dL;
        d(1)=( 2*ro*cb*dL/dt )*u(1,n) + (1/Rth )*um(n+1) +( k/dL )*(u(2,n)-u(1,n))-
B_3*(u(1,n)-um(n));
    for i=2:imax-2
        a(i)=1;
        b(i)=-2 – (2*dL2dt/Gama) - dL2*wb/Gama;
        c(i)=1;
        d(i)=-u(i-1,n)+ (2 – 2*dL2dt/Gama + dL2*wb/Gama )*u(i,n) - u(i+1,n);
```

```
    end
      a(imax-1)=1;
      b(imax-1)=-( 2 + 2*dL2dt/Gama + dL2*wb/Gama);
      d(imax-1)=(2-2*dL2dt/Gama + dL2*wb/Gama)*u(imax-1,n)-u(imax-2,n)-
2*u(imax,n);
%% Soln. by Thomas Algorithm
       ba(1)=b(1);
       ga(1)=d(1)/b(1);
    for i=2:imax-1
       ba(i)=b(i)-a(i)*c(i-1)/ba(i-1);
       ga(i)=(d(i)-a(i)*ga(i-1))/ba(i);
    end
%% Back substitution step
       u(imax-1,n+1)=ga(imax-1);
    for i=imax-2:-1:1
       u(i,n+1)=ga(i)-c(i)*u(i+1,n+1)/ba(i);
    end
%% Heat flux computationa
     qn(n)=((T0(n)-Ta0)-u(1,n))/Rth;

 end
```

(A-3) 2D cylindrical Finite Difference Derivation

Discretizing of the cylindrical form of the 2D bioheat equation is provided in this section to better illustrate the problem. The 2D finite-difference solution was developed to demonstrate the heat flux from the 2D-model is very close to the 1D-analytical solution for typical experimental condition.

$$\frac{\theta_{i,j}^{n+1}-\theta_{i,j}^{n}}{\Delta t}=\alpha\left(\frac{\theta_{i+1,j}^{n}-2\,\theta_{i,j}^{n}+\theta_{i-1,j}^{n}}{\Delta r^{2}}\right)+\alpha\frac{1}{r_i}\left(\frac{\theta_{i+1,j}^{n}-\theta_{i-1,j}^{n}}{2\Delta r}\right)+\alpha\left(\frac{\theta_{i,j+1}^{n}-2\,\theta_{i,j}^{n}+\theta_{i,j-1}^{n}}{\Delta z^{2}}\right)-w\,\theta_{i,j}^{n}$$

$$\theta_{i,j}^{n+1}-\theta_{i,j}^{n}=\frac{\alpha\Delta t}{\Delta r^{2}}\left(\theta_{i+1,j}^{n}-2\,\theta_{i,j}^{n}+\theta_{i-1,j}^{n}\right)+\frac{\alpha\Delta t}{r_i}\left(\frac{\theta_{i+1,j}^{n}-\theta_{i-1,j}^{n}}{2\Delta r}\right)+\frac{\alpha\Delta t}{\Delta z^{2}}\left(\theta_{i,j+1}^{n}-2\,\theta_{i,j}^{n}+\theta_{i,j-1}^{n}\right)-\Delta t w\,\theta_{i,j}^{n}$$

$$\theta_{i,j}^{n+1}-\theta_{i,j}^{n}=\frac{\alpha\Delta t}{\Delta r^{2}}\left(\theta_{i+1,j}^{n}-2\,\theta_{i,j}^{n}+\theta_{i-1,j}^{n}\right)+\frac{\alpha\Delta t}{r_i}\left(\frac{\theta_{i+1,j}^{n}-\theta_{i-1,j}^{n}}{2\Delta r}\right)+\frac{\alpha\Delta t}{\Delta z^{2}}\left(\theta_{i,j+1}^{n}-2\,\theta_{i,j}^{n}+\theta_{i,j-1}^{n}\right)-w\,\theta_{i,j}^{n}$$

$$\theta_{i,j}^{n+1}=\left[\frac{\alpha\Delta t}{2r_i\Delta r}+\frac{\alpha\Delta t}{\Delta r^{2}}\right]\theta_{i+1,j}^{n}+\frac{\alpha\Delta t}{\Delta r^{2}}\,\theta_{i-1,j}^{n}-\frac{\alpha\Delta t}{2r_i\Delta r}\,\theta_{i-1,j}^{n}+\frac{\alpha\Delta t}{\Delta z^{2}}\left(\theta_{i,j+1}^{n}+\theta_{i,j-1}^{n}\right)+\left[1-w-2\frac{\alpha\Delta t}{\Delta r^{2}}-2\frac{\alpha\Delta t}{\Delta z^{2}}\right]\theta_{i,j}^{n}$$

Boundary conditions are

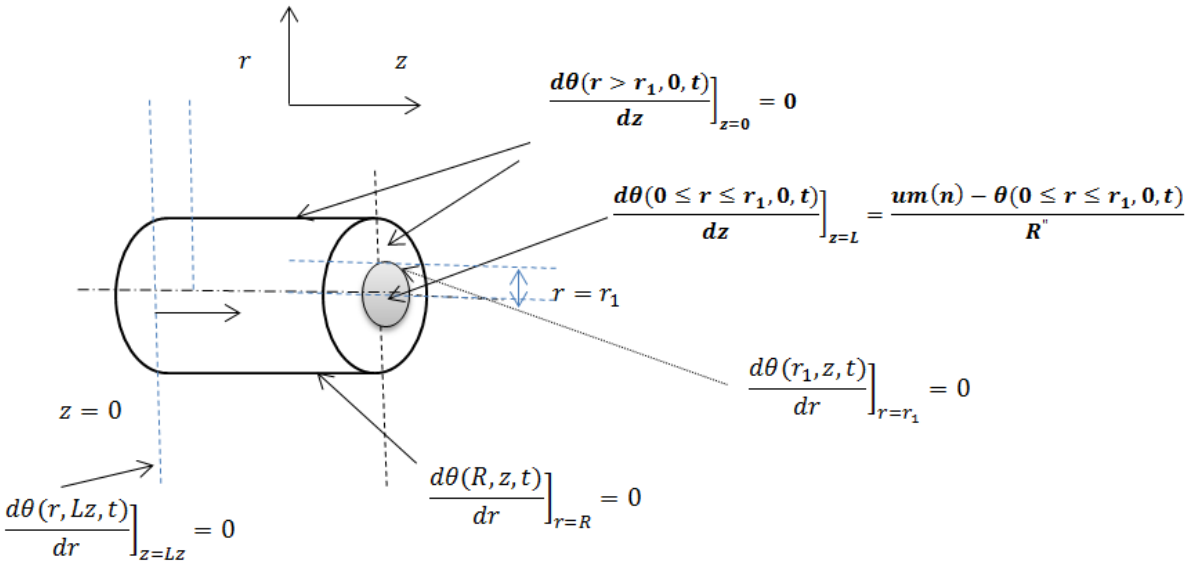

Figure A.3.1 2D finite-difference model

$$\theta_{i,j}^{n+1} - \theta_{i,j}^{n} = \frac{\alpha\Delta t}{\Delta r^2}\left(\theta_{i+1,j}^{n} - 2\,\theta_{i,j}^{n} + \theta_{i-1,j}^{n}\right) + \frac{\alpha\Delta t}{r_i}\left(\overbrace{\frac{\theta_{i+1,j}^{n} - \theta_{i,j}^{n} + \theta_{i,j}^{n} - \theta_{i-1,j}^{n}}{2\Delta r}}^{=\frac{\theta_{i+1,j}^{n} - \theta_{i-1,j}^{n}}{2\Delta r}}\right)$$

$$+ \frac{\alpha\Delta t}{\Delta z^2}\left(\theta_{i,j+1}^{n} - 2\,\theta_{i,j}^{n} + \theta_{i,j-1}^{n}\right) - w\,\theta_{i,j}^{n}$$

$$\theta_{i,j}^{n+1} - \theta_{i,j}^{n} = \frac{\alpha\Delta t}{\Delta r^2}\left(\theta_{i+1,j}^{n} - 2\,\theta_{i,j}^{n} + \theta_{i-1,j}^{n}\right) + \frac{\alpha\Delta t}{2\Delta r\; r_i}\left(\theta_{i,j}^{n} - \theta_{i-1,j}^{n}\right)$$

$$+ \frac{\alpha\Delta t}{2\Delta r\; r_i}\left(\theta_{i+1,j}^{n} - \theta_{i,j}^{n}\right) + \frac{\alpha\Delta t}{\Delta z^2}\left(\theta_{i,j+1}^{n} - 2\,\theta_{i,j}^{n} + \theta_{i,j-1}^{n}\right) - \Delta t w\,\theta_{i,j}^{n}$$

$$\theta_{i,j}^{n+1} = \left[\frac{\alpha\Delta t}{r_i\Delta r} + \frac{\alpha\Delta t}{\Delta r^2}\right]\theta_{i+1,j}^{n} + \frac{\alpha\Delta t}{\Delta r^2}\,\theta_{i-1,j}^{n} - \frac{\alpha\Delta t}{r_i\Delta r}\,\theta_{i-1,j}^{n} + \frac{\alpha\Delta t}{\Delta z^2}\left(\theta_{i,j+1}^{n} + \theta_{i,j-1}^{n}\right)$$

$$+ \left[1 - w\Delta t - 2\frac{\alpha\Delta t}{\Delta r^2} - 2\frac{\alpha\Delta t}{\Delta z^2}\right]\theta_{i,j}^{n}$$

At any node (i, j)

$$\theta_{i,j}^{n+1} - \theta_{i,j}^{n} = \frac{\alpha\Delta t}{\Delta r^2}\left(\theta_{i+1,j}^{n} - 2\,\theta_{i,j}^{n} + \theta_{i-1,j}^{n}\right) + \frac{\alpha\Delta t}{2\Delta r\; r_i}\left(\theta_{i+1,j}^{n} - \theta_{i-1,j}^{n}\right)$$

$$+ \frac{\alpha\Delta t}{\Delta z^2}\left(\theta_{i,j+1}^{n} - 2\,\theta_{i,j}^{n} + \theta_{i,j-1}^{n}\right) - \Delta t w\,\theta_{i,j}^{n}$$

Boundary condition

$$\left(\frac{\partial\theta}{\partial r}\right)_{i=1,j=1} = 0 \quad \rightarrow \quad \theta_{0,1}^{n} = \theta_{2,1}^{n}$$

$$\left(\frac{\partial\theta}{\partial z}\right)_{i=1,j=1} = 0 \quad \rightarrow \theta_{1,0}^{n} = \theta_{1,2}^{n}$$

$$\left(\frac{\partial\theta}{\partial r}\right)_{i=1,j=nz} = 0 \quad \rightarrow \quad \theta_{0,nz}^{n} = \theta_{2,nz}^{n}$$

$$\left(\frac{\partial\theta}{\partial z}\right)_{i=nr,j=1} = 0 \quad \rightarrow \theta_{nr,0}^{n} = \theta_{nr,2}^{n}$$

At skin surface where z=0 and where (j=1)

$$\left[k_p\,\frac{\theta_{i,2}^{n} - \theta_{i,0}^{n}}{2\Delta z}\right] = \left[\frac{\theta_{i,1}^{n} - \theta_{m}^{n}}{R_0^{"}}\right]$$

$$\theta_{i,1}^{n+1} - \theta_{i,1}^{n} = \frac{\alpha\Delta t}{\Delta r^2}\left(\theta_{i+1,1}^{n} - 2\,\theta_{i,1}^{n} + \theta_{i-1,1}^{n}\right) + \frac{\alpha\Delta t}{2\Delta r\, r_i}\left(\theta_{i+1,1}^{n} - \theta_{i-1,1}^{n}\right) + \frac{\alpha\Delta t}{\Delta z^2}\left(\theta_{i,2}^{n} - 2\,\theta_{i,1}^{n} + \theta_{i,0}^{n}\right) - \Delta t w\,\theta_{i,1}^{n}$$

$$\theta_{i,0}^{n} = \theta_{i,2}^{n} - \frac{2\Delta z}{R_0^{"}\,k}\left[\theta_{i,1}^{n} - \theta_{m}^{n}\right]$$

$$\theta_{i,1}^{n+1} = \theta_{i,1}^{n} + \frac{\alpha\Delta t}{\Delta r^2}\left(\theta_{i+1,1}^{n} - 2\,\theta_{i,1}^{n} + \theta_{i-1,1}^{n}\right) + \frac{\alpha\Delta t}{2\Delta r\, r_i}\left(\theta_{i+1,1}^{n} - \theta_{i-1,1}^{n}\right) + \frac{\alpha\Delta t}{\Delta z^2}\left(\theta_{i,2}^{n} - 2\,\theta_{i,1}^{n} + \theta_{i,2}^{n} - \frac{2\Delta z}{R_0^{"}\,k}\left[\theta_{i,1}^{n} - \theta_{m}^{n}\right]\right) - \Delta t w\,\theta_{i,1}^{n}$$

At the first corner: (i=1, j=1) and bellow the sensor (r <= r_1)

$$\left.\frac{\partial\theta}{\partial r}\right]_{1,1} = \frac{\theta_{2,1}^{n} - \theta_{0,1}^{n}}{2\,\Delta r} = 0 \rightarrow\ \theta_{2,1}^{n} = \theta_{0,1}^{n}$$

$$\theta_{1,1}^{n+1} = \theta_{1,1}^{n} + \frac{\alpha\Delta t}{\Delta r^2}\left(\theta_{2,1}^{n} - 2\,\theta_{1,1}^{n} + \theta_{2,1}^{n}\right) + \frac{\alpha\Delta t}{2\Delta r\, r_1}\left(\theta_{2,1}^{n} - \theta_{2,1}^{n}\right) + \frac{\alpha\Delta t}{\Delta z^2}\left(\theta_{1,2}^{n} - 2\,\theta_{1,1}^{n} + \theta_{1,2}^{n} - \frac{2\,\Delta z}{R_0^{"}\,k}\left[\theta_{1,1}^{n} - \theta_{m}^{n}\right]\right) - \Delta t w\,\theta_{1,1}^{n}$$

The end corner of the sensor ($i_s, j = 1$) and no sensor (r > r1) and no convection (h=0)
$r > r_1$

$$\left[k_p\,\frac{\theta_{i_s,2}^{n} - \theta_{i_s,0}^{n}}{2\Delta z}\right] = \frac{\left[\theta_{i_s,1}^{n} - \theta_{m}^{n}\right]}{R_0^{"}}$$

$$\left[k\,\frac{\theta_{i_s+1,1}^{n} - \theta_{i_s-1,1}^{n}}{2\Delta r}\right] = 0 \quad \rightarrow \quad \theta_{i_s+1,1}^{n} = \theta_{i_s-1,1}^{n}$$

$$\theta_{i_s,1}^{n+1} - \theta_{i_s,1}^{n} = \frac{\alpha\Delta t}{\Delta r^2}\left(\overbrace{\theta_{i_s-1,1}^{n}}^{\theta_{i_s+1,1}^{n}} - 2\,\theta_{i_s,1}^{n} + \theta_{i_s-1,1}^{n}\right) + \frac{\alpha\Delta t}{2\Delta r\, r_{i_s}}\left(\overbrace{\overbrace{\theta_{i_s-1,1}^{n}}^{\theta_{i_s+1,1}^{n}} - \theta_{i_s-1,1}^{n}}^{0}\right) + \frac{\alpha\Delta t}{\Delta z^2}\left(\theta_{i_s,2}^{n} - 2\,\theta_{i_s,1}^{n} + \theta_{i_s,0}^{n}\right) - \Delta t w\,\theta_{i_s,1}^{n}$$

$$\theta_{i_s,0}^{n} = \theta_{i_s,2}^{n} - \frac{2\Delta z}{R_0^{"}}\left[\theta_{i_s,1}^{n} - \theta_{m}^{n}\right]$$

$$\theta_{i_s,1}^{n+1} = \theta_{i_s,1}^{n} + \frac{\alpha\Delta t}{\Delta r^2}\left(2\,\theta_{i_s-1,1}^{n} - 2\,\theta_{i_s,1}^{n}\right) + \frac{\alpha\Delta t}{\Delta z^2}\left(2\,\theta_{i_s,2}^{n} - 2\,\theta_{i_s,1}^{n} - \frac{2\Delta z}{R_0^{"}}\left[\theta_{i_s,1}^{n} - \theta_{m}^{n}\right]\right) - \Delta t w\,\theta_{i_s,1}^{n}$$

At (j=1). The skin surface at z=0, where no sensor. The first corner: (i, j=1) and no sensor (r > r1) and no convection (h=0)

$$r > r_1$$

$$\left[k_p \frac{\theta_{i,2}^n - \theta_{i,0}^n}{2\Delta z}\right] = h\left[\theta_{i,1}^n - \theta_{air}^n\right]$$

$$\theta_{i,1}^{n+1} - \theta_{i,1}^n = \frac{\alpha\Delta t}{\Delta r^2}\left(\theta_{i+1,1}^n - 2\,\theta_{i,1}^n + \theta_{i-1,1}^n\right) + \frac{\alpha\Delta t}{2\Delta r\, r_i}\left(\theta_{i+1,1}^n - \theta_{i-1,1}^n\right) + \frac{\alpha\Delta t}{\Delta z^2}\left(\theta_{i,2}^n - 2\,\theta_{i,1}^n + \theta_{i,0}^n\right) - \Delta t w\,\theta_{i,1}^n$$

$$\theta_{i,0}^n = \theta_{i,2}^n - \overbrace{\frac{2\,h\,\Delta z}{k}\left[\theta_{i,1}^n - \theta_{air}^n\right]}^{0} = \theta_{i,2}^n$$

$$\theta_{i,1}^{n+1} = \theta_{i,1}^n + \frac{\alpha\Delta t}{\Delta r^2}\left(\theta_{i+1,1}^n - 2\,\theta_{i,1}^n + \theta_{i-1,1}^n\right) + \frac{\alpha\Delta t}{2\Delta r\, r_i}\left(\theta_{i+1,1}^n - \theta_{i-1,1}^n\right) + \frac{\alpha\Delta t}{\Delta z^2}\left(\theta_{i,2}^n - 2\,\theta_{i,1}^n + \theta_{i,2}^n - \overbrace{\frac{2\,h\,\Delta z}{k}\left[\theta_{i,1}^n - \theta_{air}^n\right]}^{0}\right) - \Delta t w\,\theta_{i,1}^n$$

At the corner where (i=nr, j=1)

$$\theta_{nr,1}^{n+1} = \theta_{nr,1}^n + \frac{\alpha\Delta t}{\Delta r^2}\left(\theta_{nr-1,1}^n - 2\,\theta_{nr,1}^n + \theta_{nr-1,1}^n\right) + \frac{\alpha\Delta t}{2\Delta r\, r_{nr}}\overbrace{\left(\theta_{nr-1,1}^n - \theta_{nr-1,1}^n\right)}^{0} + \frac{\alpha\Delta t}{\Delta z^2}\left(\theta_{nr,2}^n - 2\,\theta_{nr,1}^n + \theta_{nr,2}^n - \overbrace{\frac{2\,h\,\Delta z}{k}\left[\theta_{nr,1}^n - \theta_{air}^n\right]}^{0}\right) - \Delta t w\,\theta_{nr,1}^n$$

The left edge (r=0) $\{i = 1\},\ \{j = 2 \rightarrow nz - 1\}$;

$$\left.\frac{\partial\theta}{\partial r}\right]_{1,j} = \frac{\theta_{2,j}^n - \theta_{0,j}^n}{2\,\Delta r} = 0 \rightarrow\ \theta_{2,j}^n = \theta_{0,j}^n$$

$$\theta_{1,j}^{n+1} - \theta_{1,j}^n = \frac{\alpha\Delta t}{\Delta r^2}\left(\theta_{2,j}^n - 2\,\theta_{1,j}^n + \overbrace{\theta_{0,j}^n}^{\theta_{2,j}^n}\right) + \frac{\alpha\Delta t}{2\Delta r\, r_1}\left(\overbrace{\theta_{2,j}^n - \theta_{0,j}^n}^{0}\right) + \frac{\alpha\Delta t}{\Delta z^2}\left(\theta_{1,j+1}^n - 2\,\theta_{1,j}^n + \theta_{1,j-1}^n\right) - \Delta t w\,\theta_{1,j}^n$$

$$\theta_{1,j}^{n+1} - \theta_{1,j}^n = \frac{\alpha\Delta t}{\Delta r^2}\left(2\theta_{2,j}^n - 2\,\theta_{1,j}^n\right) + \frac{\alpha\Delta t}{\Delta z^2}\left(\theta_{1,j+1}^n - 2\,\theta_{1,j}^n + \theta_{1,j-1}^n\right) - \Delta t w\,\theta_{1,j}^n$$

The left edge (r=0) $\{i = 1\},\ \{j = nz\}$;

$$\left.\frac{\partial\theta}{\partial r}\right]_{1,nz} = \frac{\theta_{2,nz}^n - \theta_{0,nz}^n}{2\,\Delta r} = 0 \rightarrow\ \theta_{2,nz}^n = \theta_{0,nz}^n$$

$$\left.\frac{\partial\theta}{\partial z}\right]_{1,nz} = \frac{\theta^n_{2,nz+1} - \theta^n_{0,nz-1}}{2\,\Delta z} = 0 \rightarrow\ \theta^n_{2,nz+1} = \theta^n_{0,nz-1}$$

$$\theta^{n+1}_{1,nz} - \theta^{n}_{1,nz} = \frac{\alpha\Delta t}{\Delta r^2}\left(\theta^{n}_{2,nz} - 2\,\theta^{n}_{1,nz} + \overbrace{\theta^{n}_{0,nz}}^{\theta^{n}_{2,nz}}\right) + \frac{\alpha\Delta t}{2\Delta r\, r_1}\left(\overbrace{\theta^{n}_{2,nz} - \theta^{n}_{0,nz}}^{0}\right) + \frac{\alpha\Delta t}{\Delta z^2}\left(\overbrace{\theta^{n}_{1,nz+1}}^{\theta^{n}_{1,nz-1}} - 2\,\theta^{n}_{1,nz} + \theta^{n}_{1,nz-1}\right) - \Delta tw\,\theta^{n}_{1,nz}$$

$$\theta^{n+1}_{1,nz} - \theta^{n}_{1,nz} = \frac{\alpha\Delta t}{\Delta r^2}\left(2\theta^{n}_{2,nz} - 2\,\theta^{n}_{1,nz}\right) + \frac{\alpha\Delta t}{\Delta z^2}\left(2\,\theta^{n}_{1,nz-1} - 2\,\theta^{n}_{1,nz}\right) - \Delta tw\,\theta^{n}_{1,nz}$$

The end corner at ($i = nr, j = nz$)

$$\left.\frac{\partial\theta}{\partial r}\right]_{nr,nz} = \frac{\theta^n_{nr+1,nz} - \theta^n_{nr-1,nz}}{2\,\Delta r} = 0 \rightarrow\ \theta^n_{nr+1,nz} = \theta^n_{nr-1,nz}$$

$$\left.\frac{\partial\theta}{\partial z}\right]_{nr,nz} = \frac{\theta^n_{nr,nz+1} - \theta^n_{nr,nz-1}}{2\,\Delta z} = 0 \rightarrow\ \theta^n_{nr,nz+1} = \theta^n_{nr,nz-1}$$

$$\theta^{n+1}_{i,j} - \theta^{n}_{i,j} = \frac{\alpha\Delta t}{\Delta r^2}\left(\theta^{n}_{i+1,j} - 2\,\theta^{n}_{i,j} + \theta^{n}_{i-1,j}\right) + \frac{\alpha\Delta t}{2\Delta r\, r_i}\left(\theta^{n}_{i+1,j} - \theta^{n}_{i-1,j}\right) + \frac{\alpha\Delta t}{\Delta z^2}\left(\theta^{n}_{i,j+1} - 2\,\theta^{n}_{i,j} + \theta^{n}_{i,j-1}\right) - \Delta tw\,\theta^{n}_{i,j}$$

$$\theta^{n+1}_{nr,nz} - \theta^{n}_{nr,nz} = \frac{\alpha\Delta t}{\Delta r^2}\left(\overbrace{\theta^{n}_{nr+1,nz}}^{\theta^{n}_{nr-1,nz}} - 2\,\theta^{n}_{nr,nz} + \theta^{n}_{nr-1,nz}\right) + \overbrace{\frac{\alpha\Delta t}{2\Delta r\, r_{nr}}\left(\theta^{n}_{nr+1,nz} - \theta^{n}_{nr-1,nz}\right)}^{0} + \frac{\alpha\Delta t}{\Delta z^2}\left(\overbrace{\theta^{n}_{nr,nz+1}}^{\theta^{n}_{nr,nz-1}} - 2\,\theta^{n}_{nr,nz} + \theta^{n}_{nr,nz-1}\right) - \Delta tw\,\theta^{n}_{nr,nz}$$

$$\theta^{n+1}_{nr,nz} - \theta^{n}_{nr,nz} = \frac{\alpha\Delta t}{\Delta r^2}\left(2\theta^{n}_{nr-1,nz} - 2\,\theta^{n}_{nr,nz}\right) + \frac{\alpha\Delta t}{\Delta z^2}\left(2\,\theta^{n}_{nr,nz-1} - 2\,\theta^{n}_{nr,nz}\right) - \Delta tw\,\theta^{n}_{nr,nz}$$

The interior region ($i, j = \{2 \rightarrow nr-1\}, \{2 \rightarrow nz-1\}$)

$$\theta^{n+1}_{i,j} = \left[\frac{\alpha\Delta t}{r_i\Delta r} + \frac{\alpha\Delta t}{\Delta r^2}\right]\theta^{n}_{i+1,j} + \left[\frac{\alpha\Delta t}{\Delta r^2} - \frac{\alpha\Delta t}{r_i\Delta r}\right]\theta^{n}_{i-1,j} + \frac{\alpha\Delta t}{\Delta z^2}\left(\theta^{n}_{i,j+1} + \theta^{n}_{i,j-1}\right) + \left[1 - w - 2\frac{\alpha\Delta t}{\Delta r^2} - 2\frac{\alpha\Delta t}{\Delta z^2}\right]\theta^{n}_{i,j}$$

(A-4)- The 2D cylindrical coordinate code

The two-dimensional-cylindrical-coordinate-transient-explicit finite difference solution was used to prove that the 1D-analytical solution gives the same result. Initial temperature was calculated using the 1D steady state solution; therefore, I ran the solution first to correct the initial tissue temperature over loop 100 times before starting the solution over the run time. The function "FuncStepAnaly_FD_V" is used to generate the analytical solution to compare it with the 2D finite difference solution. The 2D-cylinderical finite difference solution code coupled together with analytical 1D-solution to demonstrate the convergence of the two heat flux results using simulated measured temperature. The simulated measured temperature is generated automatically inside the code, and the output is the surface heat fluxes from the 2D and 1D solutions.

```
%heat2D_explicit.m
format long e;
% Solves the 2D heat equation with an explicit finite difference scheme
clear all; close all; clc;
%Physical parameters
R=0.02; ro=1200; k=0.5; cb=3600; kappa = k/ro/cb; w=0.04; h=0; Rth=0.002; Tcore=37;
Tair=24-Tcore; Tskin=32;
nr = 71; % # gridpoints in x-direction              nr=101
nz=71;   % # gridpoints in x-direction              nz=101
nt = 345; % Number of timesteps to compute          nt=705;
Lr=R; r1=0.0056; Lz=0.045;
iq=15;
% Compute stable timestep
nr_s=round((nr*r1)/Lr)
r01=linspace(0,r1,nr_s);
r02=linspace(r1,Lr,nr-nr_s);
r=[r01 r02];

 dz = Lz/(nz-1)       % Spacing of grid in z-direction
 dr=Lr/(length(r)-1); % Spacing of grid in z-direction
% dt = min([dr,dz])^2/kappa/4
dt=60/(nt-1);        % Spacing of grid in z-direction
z=0:dz:Lz
Tmax=dt*(nt-1)       % Maximum run time

%% Time grids in second
for n=1:nt
t(n)=(n-1)*dt;
end

Tstep=2; Ta0=Tcore;
time = 0;

%% Creating simulated measured sensor temperature
```

```
  for m=1:nt

          T0(m)=Tskin-Tstep*(t(m)-10 >= 0)...
          -Tstep*(t(m)-20 >= 0)...
          -Tstep*(t(m)-30 >= 0)...
          -Tstep*(t(m)-40 >= 0)...
          -Tstep*(t(m)-50 >= 0)...
          -Tstep*(t(m)-60 >= 0);
        um(m)=(T0(m)-Ta0); %The Skin Non-Dim temperature um(m)=(T0(m)-Ta0);
end
%% Initial tissue temperature from the 1D steady state solution
  for ih=1:nz
  u(ih,1)=um(1)*(1.0/(1.0+Rth*k*sqrt(w/kappa)))*exp(-sqrt(w/kappa)*z(ih));
  end

for i=1:nr
   for j=1:nz
T(i,j)=u(j,1); end; end; ui=T(iq,1);

%% Plot the simulated measured temperature
figure(1);
plot(t,um+Tcore,'linewidth',2);
xlabel('t ( sec )','FontSize',14);
ylabel('Measured temperature ','FontSize',14);
%% Parameters for finite difference solution
dr2=dr*dr; dz2=dz*dz;

%%%%%%%%%%%%%%%%%%%%%%%%%%%%%
%%This loop to correct the initial tissue temperature from 1D to 2D %cylindrical
coordinates

for nSteady=1:100
% Compute new temperature
sr = kappa*dt/dr^2;
sz = kappa*dt/dz^2;
  % Loops over all nodes in r- and z- directions except boundaries
    for j=2:nz-1
    for i=2:nr-1
      %%%%%%%%%%%%%%%%%%%%
      % Equations to solve
    if ( i <= nr_s)
     Tnew(1,1)=T(1,1)+(kappa*dt/dr2)*(T(2,1)-2*T(1,1)+T(2,1) ) + (0.5*kappa*dt/dr2)*(
T(2,1) - T(2,1) ) + (kappa*dt/dz2)*( T(1,2) - 2*T(1,1) +T(1,2) + (-2*dz/(Rth*k))*( T(1,1)
-um(1) ) )-dt*w*T(1,1);
     if i == nr_s
```

```
    Tnew(nr_s,1)=T(nr_s,1)+(kappa*dt/dr2)*(T(nr_s-1,1)-2*T(nr_s,1)+T(nr_s-1,1) ) +
(0.5*kappa*dt/(dr*r(nr_s)))*( T(nr_s-1,1) - T(nr_s-1,1) ) + (kappa*dt/dz2)*( T(nr_s,2) -
2*T(nr_s,1) +T(nr_s,2) + (-2*dz/(Rth*k))*( T(nr_s,1) -um(1) ) )-dt*w*T(nr_s,1);
    end
    if (i < nr_s)
    Tnew(i,1)=T(i,1)+(kappa*dt/dr2)*(T(i+1,1)-2*T(i,1)+T(i-1,1) ) +
(0.5*kappa*dt/(dr*r(i)))*( T(i+1,1) - T(i-1,1) ) + (kappa*dt/dz2)*( T(i,2) - 2*T(i,1)
+T(i,2) + (-2*dz/(Rth*k))*( T(i,1) -um(1) )) -dt*w*T(i,1);
    end

    else

Tnew(nr,1)=T(nr,1)+(kappa*dt/dr2)*(T(nr-1,1)-2*T(nr,1)+T(nr-1,1) ) +
(0.5*kappa*dt/(dr*r(nr)))*( T(nr-1,1) - T(nr-1,1) ) + (kappa*dt/dz2)*( T(nr,2) - 2*T(nr,1)
+T(nr,2) + (-(2*h*dz)/k)*( T(nr,1) -Tair )) -dt*w*T(nr,1);
     Tnew(i,1)=T(i,1)+(kappa*dt/dr2)*(T(i+1,1)-2*T(i,1)+T(i-1,1) ) +
(0.5*kappa*dt/(dr*r(i)))*( T(i+1,1) - T(i-1,1) ) + (kappa*dt/dz2)*( T(i,2) - 2*T(i,1)
+T(i,2) + (-(2*h*dz)/k)*( T(i,1) -Tair )) -dt*w*T(i,1);

        end


      Tnew(1,j) = sr*( 1.0 + ( 0.5*dr/dr) )*T(2,j) + sr*( 1.0 - (0.5*dr/dr) )*T(2,j) +
sz*(T(1,j+1) + T(1,j-1))...
      +(1-dt*w-2*sr-2*sz)*T(1,j);

      Tnew(i,j) = sr*( 1.0 + ( 0.5*dr/r(i)))*T(i+1,j) + sr*(1.0 - (0.5*dr/r(i)) )*T(i-1,j) +
sz*(T(i,j+1) + T(i,j-1))...
      +(1-dt*w-2*sr-2*sz)*T(i,j);


   Tnew(i,nz) = sr*( 1.0 + ( 0.5*dr/r(i) ) )*T(i+1,nz) + sr*( 1.0 - (0.5*dr/r(i)) )*T(i-1,nz)
+ sz*(T(i,nz-1) + T(i,nz-1))...
      +(1-dt*w-2*sr-2*sz)*T(i,nz);


   Tnew(1,nz) = sr*( 1.0 + 0.5*dr/dr)*T(2,nz) + sr*( 1.0 - (0.5*dr/dr) )*T(2,nz) +
sz*(T(1,nz-1) + T(1,nz-1))...
      +(1-dt*w-2*sr-2*sz)*T(1,nz);
   %%%%%%%%%%%%%%%%

      Tnew(nr,j) = sr*( 1.0 + 0.5*dr/r(nr))*T(nr-1,j) + sr*(1.0 - (0.5*dr/r(nr)) )*T(nr-1,j)
+ sz*(T(nr,j+1) + T(nr,j-1))...
      +(1.0 - dt*w-2*sr-2*sz)*T(nr,j);
```

```
      Tnew(nr,nz) = sr*( 1.0 + 0.5*dr/r(nr))*T(nr-1,nz) + sr*( 1.0 - (0.5*dr/r(nr)) )*T(nr-
1,nz) + sz*(T(nr,nz-1) + T(nr,nz-1))...
      +(1-dt*w-2*sr-2*sz)*T(nr,nz);

  end


end

T = Tnew;
end

%%Plot the correct initial tissue temperature for the cylindrical coordinate
figure(2);
for j=1:nr
plot(z,T(j,:)+Tcore,'linewidth',2);
hold on;
end
hold off;
xlabel('z ( m )','FontSize',14);
ylabel('T ','FontSize',14);
%%%%%%%%%%%%%%%%%%%%%%%%%%
ui=T(iq,1)
%%%%%%%%%%%%%%%%%%%%%%%%%%%%%%%%%%%%%%%%%%%%%%%%%
%
%%Solving for the run time

for n=1:nt
% Compute new temperature
t(n)=(n-1)*dt;

sr = kappa*dt/dr^2;
sz = kappa*dt/dz^2;
%% Initial heat flux
qn(1)=-(ui-um(1))/Rth;
%% Loops around the two spaces (r,z)
  for j=2:nz-1
  for i=2:nr-1
%%%%%%%%%%%%%%%%%%%%%%%%%%%%%%%%%%%%%%%%%%%%%%%%%
%%%%%%%%%%
%% Equations to solve
    if ( i <= nr_s)
    Tnew(1,1)=T(1,1)+(kappa*dt/dr2)*(T(2,1)-2*T(1,1)+T(2,1) ) + (0.5*kappa*dt/dr2)*(
T(2,1) - T(2,1) ) + (kappa*dt/dz2)*( T(1,2) - 2*T(1,1) +T(1,2) + (-2*dz/(Rth*k))*( T(1,1)
-um(n) ) )-dt*w*T(1,1);
    if i == nr_s
```

```
    Tnew(nr_s,1)=T(nr_s,1)+(kappa*dt/dr2)*(T(nr_s-1,1)-2*T(nr_s,1)+T(nr_s-1,1) ) +
(0.5*kappa*dt/(dr*r(nr_s)))*( T(nr_s-1,1) - T(nr_s-1,1) ) + (kappa*dt/dz2)*( T(nr_s,2) -
2*T(nr_s,1) +T(nr_s,2) + (-2*dz/(Rth*k))*( T(nr_s,1) -um(n) ) )-dt*w*T(nr_s,1);
    end
    if (i < nr_s)
    Tnew(i,1)=T(i,1)+(kappa*dt/dr2)*(T(i+1,1)-2*T(i,1)+T(i-1,1) ) +
(0.5*kappa*dt/(dr*r(i)))*( T(i+1,1) - T(i-1,1) ) + (kappa*dt/dz2)*( T(i,2) - 2*T(i,1)
+T(i,2) + (-2*dz/(Rth*k))*( T(i,1) -um(n) )) -dt*w*T(i,1);
    end

        else
     Tnew(nr,1)=T(nr,1)+(kappa*dt/dr2)*(T(nr-1,1)-2*T(nr,1)+T(nr-1,1) ) +
(0.5*kappa*dt/(dr*r(nr)))*( T(nr-1,1) - T(nr-1,1) ) + (kappa*dt/dz2)*( T(nr,2) - 2*T(nr,1)
+T(nr,2) + (-(2*h*dz)/k)*( T(nr,1) -Tair )) -dt*w*T(nr,1);
     Tnew(i,1)=T(i,1)+(kappa*dt/dr2)*(T(i+1,1)-2*T(i,1)+T(i-1,1) ) +
(0.5*kappa*dt/(dr*r(i)))*( T(i+1,1) - T(i-1,1) ) + (kappa*dt/dz2)*( T(i,2) - 2*T(i,1)
+T(i,2) + (-(2*h*dz)/k)*( T(i,1) -Tair )) -dt*w*T(i,1);

        end

     Tnew(1,j) = sr*( 1.0 + ( 0.5*dr/dr) )*T(2,j) + sr*( 1.0 - (0.5*dr/dr) )*T(2,j) +
sz*(T(1,j+1) + T(1,j-1))...
     +(1-dt*w-2*sr-2*sz)*T(1,j);

     Tnew(i,j) = sr*( 1.0 + ( 0.5*dr/r(i)))*T(i+1,j) + sr*(1.0 - (0.5*dr/r(i)) )*T(i-1,j) +
sz*(T(i,j+1) + T(i,j-1))...
     +(1-dt*w-2*sr-2*sz)*T(i,j);


  Tnew(i,nz) = sr*( 1.0 + ( 0.5*dr/r(i) ) )*T(i+1,nz) + sr*( 1.0 - (0.5*dr/r(i)) )*T(i-1,nz)
+ sz*(T(i,nz-1) + T(i,nz-1))...
     +(1-dt*w-2*sr-2*sz)*T(i,nz);

      Tnew(1,nz) = sr*( 1.0 + 0.5*dr/dr)*T(2,nz) + sr*( 1.0 - (0.5*dr/dr) )*T(2,nz) +
sz*(T(1,nz-1) + T(1,nz-1))...
     +(1-dt*w-2*sr-2*sz)*T(1,nz);

%%%%%%%%%%%%%%%%%%%%%%%%%%%%%%%%%%%%%%%%%%%
%%%%%%%%%%%%%%


      Tnew(nr,j) = sr*( 1.0 + 0.5*dr/r(nr))*T(nr-1,j) + sr*(1.0 - (0.5*dr/r(nr)) )*T(nr-1,j)
+ sz*(T(nr,j+1) + T(nr,j-1))...
     +(1.0 - dt*w-2*sr-2*sz)*T(nr,j);
```

```
        Tnew(nr,nz) = sr*( 1.0 + 0.5*dr/r(nr))*T(nr-1,nz) + sr*( 1.0 - (0.5*dr/r(nr)) )*T(nr-
1,nz) + sz*(T(nr,nz-1) + T(nr,nz-1))...
       +(1-dt*w-2*sr-2*sz)*T(nr,nz);

  end
end
%%Temperature solution at time tn
T = Tnew;
%% Heat flux qn at time tn
qn(n)=-(T(iq,1)-um(n))/Rth;
%% Skin temperature from the 2D cylindrical finite difference
TnSkin(n)=T(iq,1);
 for ir=1:nr
    Trn(ir,n)=Tnew(ir,1);
 end
time = time+dt;
%% 2D cylindrical FD temperature in two dimension over all time
figure(3);
mesh(r,z,T+Tcore,'linewidth',2);
   xlabel('r ( m )','FontSize',14);
   ylabel('z ( m )','FontSize',14);
   zlabel('T(r,z,t) - ( C^0 )','FontSize',14);
hold on;
end
hold off
%% Analytical Solution
[qAnaly, SkinTemp] = FuncStepAnaly_FD_V(
ui,um+Tcore,Tcore,t,w,kappa,k,Rth,ro,cb,nt);
[qn' qAnaly']
%% Plot 2D cylindrical finite difference versus analytical solution
figure(4);
plot(t,qn,'r',t,qAnaly,'b','linewidth',2);
h1 = legend('FD Heat Flux','Analytical Heat Flux',2);
  set(h1,'Interpreter','none');
xlabel('t ( sec )','FontSize',14);
ylabel('q_h ( W/m^2 )','FontSize',14);
%% Plot skin temperature of the cylindrical FD and analytical solutions
figure(5);
plot(t,TnSkin(n)+Tcore,'b',t,SkinTemp(n)+Tcore,'r','linewidth',2);
h2 = legend('FD Skinn Temp','Analytical skin Temp',3);
  set(h2,'Interpreter','none');
xlabel('t ( sec )','FontSize',14);
ylabel('T ( C^0 )','FontSize',14);

%%Error between 2D cylindrical finite difference and analytical heat fluxes
ErrSum=0;
```

```
for kt=1:nt
  err(kt)= (( um(kt) - TnSkin(kt) )/Rth )-qAnaly(kt) ;
end

plot(t,err,'linewidth',2);
xlabel('t ( sec )','FontSize',14);
ylabel('err =  q_F_D - q_a_n_a_l_y ','FontSize',14);
```

Function to create the analytical solution to compare it with the 2D cylindrical coordinate is:

```
function [qAnaly, SkinTemp] = FuncStepAnaly_FD_V(
u1,T0,Ta0,t,beta,Gama,k,Rth,ro,cb,nmax)
      SStep=0;
 for n=1:nmax

if n>1
     if ( T0(n) - T0(n-1)<0.0001)    % Test the step measured temperature
        SStep=SStep+1;         % Counter for how many steps
        tsp(SStep)=t(n);

   uold(SStep)=T0(n-1); unew(SStep)=T0(n);

     end
 end


  qSt=0;
  if SStep > 0
for Step=1:SStep
    %---     G -> Evaluate the Green's function integration    ---%
HeatStep(Step)=G(t(n),tsp(Step),cb,uold(Step),unew(Step),beta,Gama,k,Rth,ro);
qSt=HeatStep(Step)+qSt;
end
  end

SkinTemp(n)=qSt;

          %------  Total analytical heat flux  -----%

qAnaly(n)= ((T0(n)-Ta0)-(SkinTemp(n)+u1))/Rth;


end
         %----------   End of the time Loop   -------%
```

%--%

Plot for the result:

Results of comparing the 2D cylindrical finite difference solution to the 1D-analytical solution is illustrated using simulated measured temperature. The output is the finite difference heat flux versus analytical heat flux.

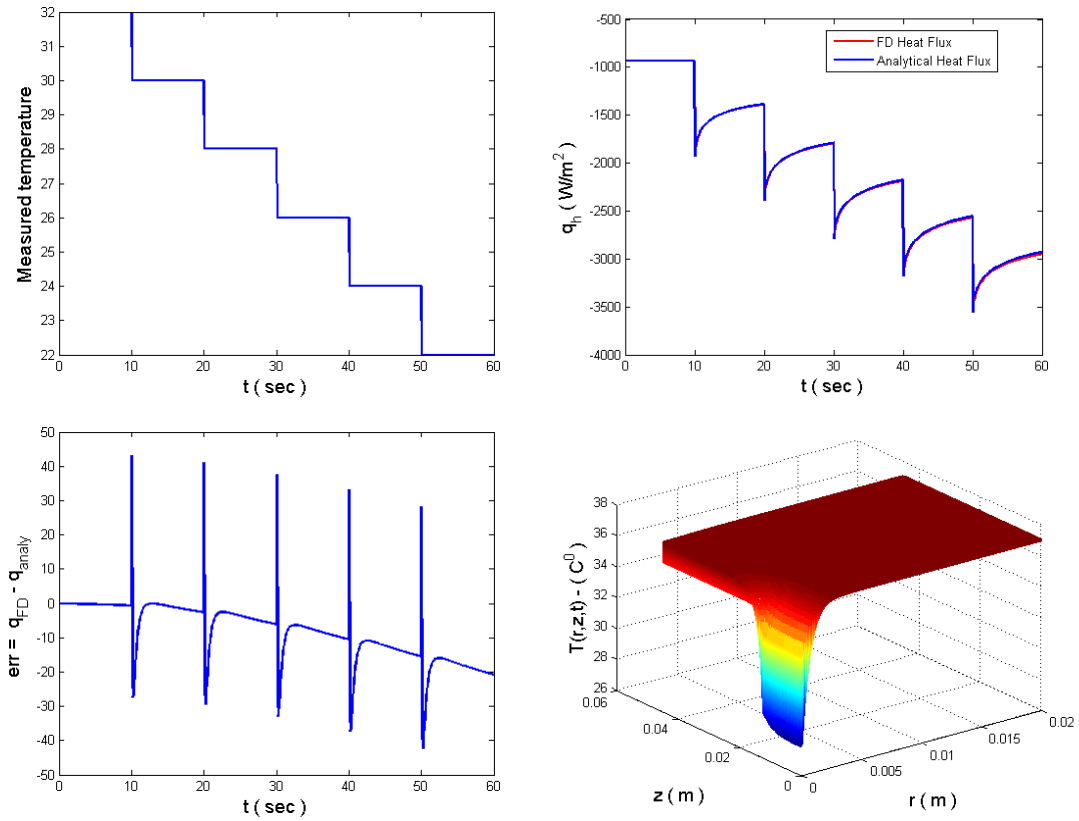

Figure A.4.1 Temperature, heat flux and error plots from 2D finite-difference versus Analytical solution

Dimension and material properties were used to evaluate the 2D finite difference model

ro=1200; k=0.5; cb=3600; kappa = k/ro/cb; w=0.04; h=0; Rth=0.002; Tcore=37;
Tair=24-Tcore; Tskin=32;

Lr=0.02; % # Maximum radius
r_sensor=0.0056; % # Sensor radius
nr = 101; % # gridpoints in r-direction
nz=101; ; % # gridpoints in z-direction
nt = 705; % Number of timesteps to compute
Lz=0.045; % # Depth of tissue in z-direction

For steady state soln:
I use the 1D steady state as an initial guess
for ih=1:nz

```
u(ih,1)=um(1)*(1.0/(1.0+Rth*k*sqrt(w/kappa)))*exp(sqrt(w/kappa)*z(ih);
end
```

I ran this solution through the 2D finite difference equations throughout 100 loops, to get to the right initial temperature distribution through tissue in r- and z-direction, because the above steady state soln. is just for 1D

Appendix B – The analytical model

This solution is developed during this research in the first time to simplify the use of thermal measurements in solving many biological problems where perfusion and heat through tissue take place. We prove the simplicity and stability and consistency of the model among 1D and 2D finite difference solutions. Moreover, a new technique to estimate three parameters was developed during this research to give faster, stable and repeatable results.

(B-1)- Green's function based solution

Details of the derivation of the analytical model are giving in this section and organize in the following tables. The Green's function solution is coded in a function called "G"

Table B.1.1 Mathematical Formulation of the Bioheat Model

	Governing Equations	Variable shift: $\theta(x,t) = T(x,t) - T_{core}$ $\alpha = \frac{k}{\rho c}$, $\beta = \frac{(\rho c w)_b}{\rho c} \cong w$
PDE	$\rho c \frac{\partial T}{\partial t} = k \frac{\partial^2 T}{\partial x^2} - (\rho c w)_b (T(x,t) - T_{core})$	$\frac{\partial \theta}{\partial t} = \alpha \frac{\partial^2 \theta}{\partial x^2} - \beta \cdot \theta$
BC's	$-k \frac{\partial T}{\partial x} = \frac{1}{R''} (T_s(t) - T)$, $x = 0$ $\frac{\partial T}{\partial x} \to 0$, $x \to \infty$	$-k \frac{\partial \theta}{\partial x} = \frac{1}{R''} (\theta_s(t) - \theta)$, $x = 0$ $\frac{\partial \theta}{\partial x} \to 0$, $x \to \infty$
IC	$T = T_i(x)$, $t = 0$	$\theta = \theta_i(x)$

Sensor Temp	$T_s(t) = T_{s,0} + \sum_{n=1}^{Nmax} \Delta T_{s,n} \cdot H(t - t_n)$ $\Delta T_{s,n} = T_{s,n} - T_{s,n-1}$	$\theta_s(t) = T_s(t) - T_{core}$ $= \theta_{s,0} + \sum_{n=1}^{Nmax} \Delta \theta_{s,n} \cdot H(t - t_n)$ $\Delta \theta_{s,n} = \Delta T_{s,n} = T_{s,n} - T_{s,n-1}$

Determination of IC

PDE	$0 = k\frac{d^2T_i}{dx^2} - (\rho cw)_b(T_i - T_{core})$	$0 = \alpha\frac{d^2\theta_i}{dx^2} - \beta \cdot \theta_i$
BC's	$-k\frac{dT_i}{dx} = \frac{1}{R''}(T_{s,0} - T_i), \quad x = 0$ $\frac{dT_i}{dx} \to 0, \quad x \to \infty$	$-k\frac{d\theta_i}{dx} = \frac{1}{R''}(\theta_{s,0} - \theta_i), \quad x = 0$ $\frac{d\theta_i}{dx} \to 0, \quad x \to \infty$
Solution		$\theta_i(x) = \theta_{s,0}\left(\frac{1}{1 + R''k\sqrt{\beta/\alpha}}\right)e^{-\sqrt{\frac{\beta}{\alpha}}x}$ $q_i = k\theta_{s,0}\left(\frac{1}{1 + R''k\sqrt{\beta/\alpha}}\right)\sqrt{\frac{\beta}{\alpha}}$

Surface Temperature

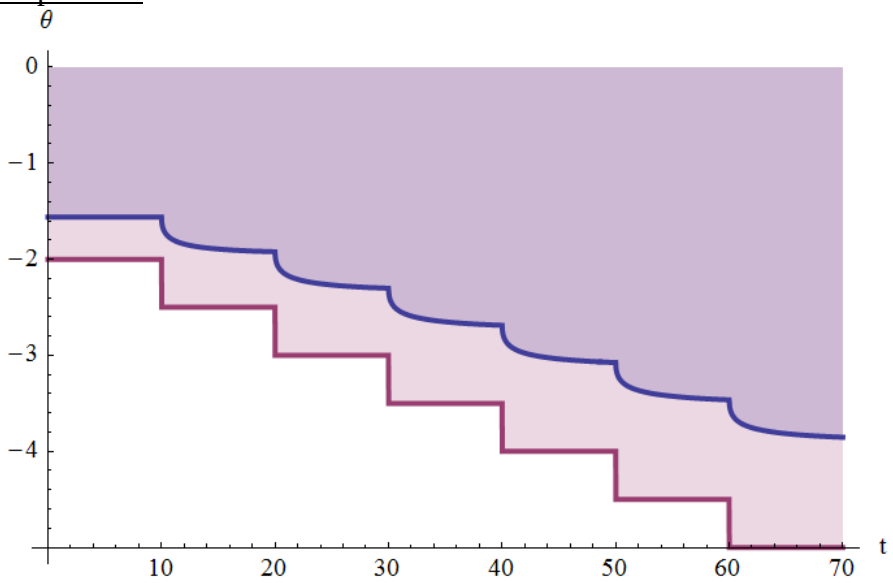

Figure B.1.1 Simulated surface and measured temperature from analytical model using Mathematica.

$$\theta_s(t) = T_s(t) - T_{core} = \theta_{s,0} + \sum_{n=1}^{Nmax} \Delta\theta_{s,n} \cdot H(t - t_n)$$

$$\Delta\theta_{s,n} = \Delta T_{s,n} = T_{s,n} - T_{s,n-1}$$

Table B.1.2 Analysis: Green's Function Method

Superposition $\boldsymbol{\theta(x,t) = \theta_i(x) + \theta_T(x,t)}$	Green's Function Formulation
$\frac{\partial \theta_T}{\partial t} = \alpha \frac{\partial^2 \theta_T}{\partial x^2} - \beta \cdot \theta_T$	$\frac{\partial G}{\partial t} = \alpha \frac{\partial^2 G}{\partial x^2} - \beta G + \delta(x - x_o)\delta(t - t_o)$
$-k\frac{\partial \theta_T}{\partial x} = \frac{1}{R''}\left(\theta_s(t) - \theta_{s,0} - \theta_T\right), \quad x = 0$ $\frac{\partial \theta_T}{\partial x} \to 0\,, \quad x \to \infty$	$-k\frac{\partial G}{\partial x} = \frac{1}{R''}(-G), \quad x = 0$ $\frac{\partial G}{\partial x} \to 0\,, \quad x \to \infty$
$\theta_T = 0 \quad , \quad t = 0$	$G = 0 \quad , \quad t \le t_o$

Table B.1.3 Solution in Terms of the GF

$$\theta_T(x,t) = \frac{1}{\rho c}\int_{t_o=0}^{t} \frac{1}{R''}\left(\theta_s(t_o) - \theta_{s,0}\right) G(x,t|0,t_o)dt_o$$

$$\theta_T(x,t) = \frac{1}{\rho c}\int_{t_o=0}^{t} \frac{1}{R''}\sum_{n=1}^{Nmax} \Delta\theta_{s,n} \cdot H(t_o - t_n)\, G(x,t|0,t_o)dt_o$$

$$\theta_T(x,t) = \frac{1}{\rho c}\frac{1}{R''}\sum_{n=1}^{Nmax} \Delta\theta_{s,n} \int_{t_o=0}^{t} H(t_o - t_n)\, G(x,t|0,t_o)dt_o$$

Green's Function

$$G(x,t\,|\,x_o,t_o) = Exp\left(-\beta(t-t_o)\right)\frac{1}{\sqrt{4\pi\alpha(t-t_o)}}\left(Exp\left(-\frac{(x-x_o)^2}{4\alpha(t-t_o)}\right) + Exp\left(-\frac{(x+x_o)^2}{4\alpha(t-t_o)}\right)\right)$$

$$- Exp\left(-\beta(t-t_o)\right)\frac{1}{kR''}\cdot Exp\left(\left(\frac{1}{k^2R''^2}\alpha\right)(t-t_o) + \frac{1}{kR''}(x+x_o)\right) Erfc\left(\frac{x+x_o}{\sqrt{4\alpha(t-t_o)}} + \frac{1}{kR''}\sqrt{\alpha(t-t_o)}\right)$$

$$G(0,t|0,t_o) = \mathrm{Exp}(-\beta(t-to))\left(\frac{2}{\sqrt{4\pi\alpha(t-to)}} - \frac{1}{k\cdot R_{th}}\mathrm{Exp}\left(\frac{\alpha(t-to)}{k^2\,{R_{th}}^2}\right)\mathrm{Erfc}\left(\frac{\sqrt{\alpha(t-to)}}{k\cdot R_{th}}\right)\right)$$

(B-2) - Parameter estimation routine

Parameter estimation routine was first created during this research. The coming figure illustrates the simplicity and efficiency of the routine. This routine was coupled with the analytical solution to estimate three parameters which are blood perfusion, thermal resistance and core temperature. The parameter estimation routine uses a zooming technique, which built in function called "Meshing_PE", to zoom around the optimal solution of blood perfusion and thermal resistance to give more and more accurate solution. A function for calculating the error, called "FuncStep_SDOR", was used to direct the search for the optimal blood perfusion and thermal resistance values which give the minimum error.

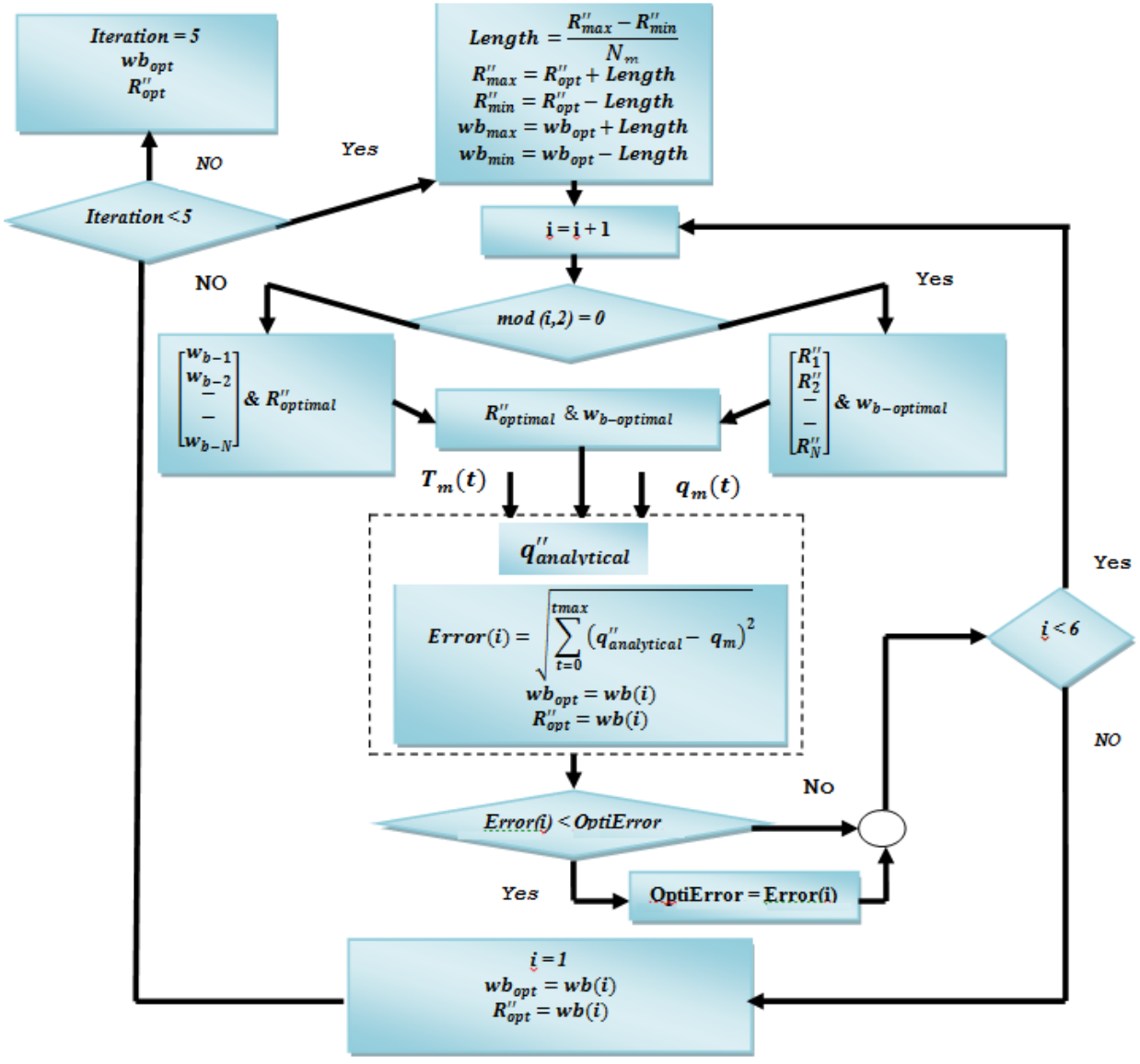

Figure B.2.1 Schematic diagram of the parameter estimation routine

(B-3)- Analytical Solution code

Analytical model contains both analytical solution and parameter estimation routine.

Data format must be arranged as the following table

Format of the input file in the code is "dat" but you can change it. Please provide your date as

Table B.3.1 Data format

Time (seconds)	Heat flux (μV)	Measured temperature (C^0)
1	-0.0001835062118213863	26.023304914788064
2	-0.00018977980299502486	25.9639886490167
3	-0.0001819040923085419	26.002753781320745
4	-0.0001816593423749251	25.992133094731756
5	-0.00018099089423248457	26.008418708858528
6	-0.00018662851959442696	25.97762484108121

The Driver program

This is the mean driver program from which loading data and converting units and calling other functions take place. Running the code requires data which must be arranged in the same manner as the above table. All values of tissue properties are indicated in SI-unites. The program is splatted to functions as:-

(1)- The driver program from which the mathematical model is called "DriverProgramD_15Aug"
(2)- Calculating SDOR using function which called "FuncStep_SDOR"
(3)- Function to calculate analytical temperature and heat flux which called "FuncStepAnaly"
(4)- The Zooming Function to provide new meshes for contact resistance and blood perfusion around the optimal values which called "Meshing_PE"
(5)- Plotting analytical results using two functions, "PlotSolutionHF" and "PlotSolutionTemperature"
(6)- The Green's function which is "G"

```
function DriverProgramD_15Aug()
% Abdusalam Alkhwaji
%Transient Bioheat Equation -
% Maximum space and time step numbers
clear all; clc;
format long e;
tic;
%% Loading measurement
% load try30_24MarchOld.txt;
% y=try30_24MarchOld;
  load SimulatedData_3.dat;
  y=SimulatedData_3;
% maximum=21; iteration=15; maximum2=21;  ratio=15;
maximum=31; iteration=5; maximum2=31;  ratio=10; oo_max=5;
```

```
%% Domain for blood perfusion and contact resistances
% Blood perfusion
W_min=0.0000000000000011111; W_max=0.111111111111111111111;
% Contact resistance
R_min=0.00000000000000001111111111111; R_max=0.111111111111111111111;

factor1=0;   % factor to avoid zooming to the negative direction of blood perfusion or
contact resistance
%% Calibration's factors
      %% Making sure that the heat flux sign is in the right direction, because switching
the 2 wires of HF sensor change the sign of HF
         if y(2,2)>0
           SignHF=-1;
         else SignHF=1;
         end
            Constant=10000000;
            Calibration_HF=SignHF*2.1;
 %% Total samples available from the measurement
    nmax=length(y(1:end,1));
 %% The whole data of 70 seconds
    Qm = y(:,2); T0=y(:,3); t=y(:,1);  start=1;
    nmax=length(y(start:end,1)); stop=nmax;
  %% Plot for the whole temperature and heat flux during the 70 seconds
  %% Cutting the first set of steady state values of measurement: around ~ 10 sec
    % After the cut
    for ii=2:nmax
       if Qm(ii)/Qm(ii-1) >2 % condition to cut the offsie
         start1=ii;         % ii is he starting poin o the transient problem
       end
    end

    if start1>1 % Constant to stop at the initial temperature measurement
    stop1=1;
    else
       stop1=0;
    end
 %% If you want to take all time from 0 untill 70 then start=1 and stop=70
    start=1; %stop=70; %nmax=stop-start;

%%% -----      Average of the initial measured temperature       -----%%%
    Tii=y(1:start1-stop1,3); Ti=mean(Tii);

%%% -----      Average of the initial measured heat flux         -----%%%
    QmOff= (10000000/Calibration_HF)*y(1:start1-stop1,2); Qmi=mean(QmOff);

    %% Make sure the output of the termocouple and heat flux sensor is staple
```

```
    Qm = (Constant/Calibration_HF)*y(start:stop,2); % Heat flux;
     %-----------------------------------------------------------------%
    %% PLOT for Measurd Heat flux and temperature
     t=y(start:stop,1)-start; T0=y(start:stop,3); i=1:start1-stop1; T0(i)=Ti; i=1:start1-stop1;
Qm(i)=Qmi;
    plot(t,T0,'b','linewidth',3);
    xlabel('time sec','FontSize',14);
    ylabel('Measured Temperature','FontSize',14);
    title('Measured temperature distribution','FontSize',12);

    figure(2);
    plot(t,-Qm,'b','linewidth',3);
    xlabel('time sec','FontSize',14);
    ylabel('Measured HF','FontSize',14);
    title('Measured heat flux','FontSize',12);

     %----------------------  Tissue Properties     ---------------------%
     ro=1050;   % Density of tissue kg/m^3
     cb=3.8e3;  % Specific heat of tissue J-kg/k
     k=.5;      % Thermal conductivity of tissue W/m-k
     imax=211;  % Number of x meshes - We do not need it here
     Lmax=.02;  % Length of tissue (m) - We do not need it here
     u=zeros(imax,1);     % Teatha -> The shifting skin temperature
    %-----------------------------------------------------------------%

%% Starting solution
% initial global minimum error
       GSDOR=1000;

%% Zooming around the optimal values of wbj and Rthi by "nmn" Iterations
wbmin=W_min; Rthmin=R_min;
for nmn=1:iteration   % iteration for zooming

Rth_range = elm_line3 (R_min,R_max,maximum,ratio); wb_range = elm_line3
(W_min,W_max,maximum,ratio);
length_wb=(W_max-W_min)/maximum;     length_Rth=(R_max-R_min)/maximum;

jjj=1; nRth=1; nwb=1;

 oo=1;
while (jjj<maximum+1 && oo < oo_max) % && start_Rth<ma7ximum &&
start_wb<maximum)
     qAnaly=zeros(1,nmax);


    if mod(oo,2) == 0   % wb= wbmin -> wbmax
```

```
        nnRth=0;
       nnwb=1;
        Rth=Rth_range(jjj);
        wb=wbmin;
        if jjj==maximum
           oo=oo+1;
           jjj=1; Rth=Rthmin; end
    else
       nnRth=1;
       nnwb=0;
       Rth=Rthmin;
       wb=wb_range(jjj);

        if jjj==maximum
           oo=oo+1;
          jjj=1; wb=wbmin; end
    end

        beta=wb; Gama=k/ro/cb;
%------------   Solving for each wb, Rth and zooming (nmn)   -------------%

%% Estimating the core temperature ->
       Ta0=Ti-Qmi/(k*sqrt(beta/Gama)/(1+Rth*k*sqrt(beta/Gama)));
% Initial temperature at the skin  u(x=0, t=0) = ->
      u(1,1)=(Ti-Ta0)*(1/(1+Rth*k*sqrt(beta/Gama)));
          %%%%%%% Calculating SDOR  %%%%%%%%
  %%%-----------------------------------------------%%%
[SDOR] = FuncStep_SDOR( u(1,1),T0,Ta0,t,beta,Gama,k,Rth,ro,cb,nmax,Qm );
         %----------   End of the time Loop   -------%
       %-----------------------------------------------%

%*-----------------  LOOKING FOR THE MINIMUM ERROR -------------------*%
%% Summation of the sqrt of the errors for each wbj, Rthi and zoomin "nmn"
 errTRth(jjj)=SDOR;
 wbb(jjj,oo,nmn)=wb;Rthh(jjj,oo,nmn)=Rth; errTRthh(jjj,oo,nmn)=errTRth(jjj);
 if ( errTRth(jjj) < GSDOR  )

 if nnwb==1     %nnwb=1    -> nnRth=0 ->  wb=wbmin  -> Rth=Rth1(jjj);

     nwb=jjj;
          Rthmin=Rth;                % Minimum Contact Resistance
          wbmin=wb;                  % Minimum Blood perfusion
          Ta0_opt=Ta0;               % Optimal Tcore
 end
 if nnRth==1      %nnRth=1    -> nnwb=0 ->  Rth=Rthmin  -> wb=wb1(jjj);
   % nRth=njjj;
```

```
   nRth=jjj;
         Rthmin=Rth;                % Minimum Contact Resistance
         wbmin=wb;                  % Minimum Blood perfusion
         Ta0_opt=Ta0;               % Optimal Tcore
 end

GSDOR=errTRth(jjj);
 end

 jjj=jjj+1;
oo;

end

    %*-----------------        ZOOMING         ------------------*%
  %   Zooming to look for more accurate result around the optimal value %

%% Meshing arround the optimal solution
[ R_min, R_max, W_min,W_max  ] = Meshing_PE( Rthmin,length_Rth,
wbmin,length_wb, factor1  );
   maximum=maximum2;
% End the N iteration
end

%% The optimal result are:
Rth = Rthmin
wb  = wbmin
Ta0 = Ta0_opt
GSDOR
%**************************************************************************
*%
%---   Evaluating the optimal result agin in the mathematical model  ---%

Gama=k/ro/cb; beta=wb;   % Constants for the new solution

%% Initial temperature of the skin:
u(1,1)=(Ti-Ta0)*(1/(1+Rth*k*sqrt(beta/Gama))); %*exp(-sqrt(beta/Gama)*L(ih));
%%%%%%%%%%%%%%%%%%%%%%%%%%%%%%%%%%%%%%%%%%%%%%%%%%%%%%%%%%%%%%%%%%%%%%%
%%%%%%%%%%%%%%%%%%%%%%%%%%%%%%%%%%%%%%%%%%%%%%%%%%%%%%%%%%%%%%%%%%%%%%%
  %%%%%% Evaluating the analytical solution with optmal EP  %%%%%%%

 [qAnaly, SkinTemp] = FuncStepAnaly( u(1,1),T0,Ta0,t,beta,Gama,k,Rth,ro,cb,nmax );
%-----------------%%%%%%%%%%%%%%%%%%%%%%%%%%%%%%%%%%%%%%%%%%%%%%%%%%%%%%%%
-------%
 %% Plot Transient against Measured
```

```
figure(3);
subplot(2, 1, 1)
PlotSolutionTemperature(nmax,Ta0,T0,SkinTemp,u(1,1),t);
subplot(2, 1, 2)
PlotSolutionHF(nmax,qAnaly,t,Qm);
figure(5);
plot(t,Ta0);


%----- save every think to file ResultSimulatedData_3.mat ----%
savefile = 'ResultSimulatedData_3.mat';
%savefile = 'Resulttry30_24MarchOld.mat';
save(savefile, 'wbb','oo_max','oo','Rthh','errTRthh','iteration')
toc
```

Functions for calculating the SDOR

```
function [SDOR] = FuncStep_SDOR( u1,T0,Ta0,t,beta,Gama,k,Rth,ro,cb,nmax,Qm )
SStep=0;ErrSum=0;
 for n=1:nmax

if n>1
      if ( T0(n) ~= T0(n-1))    % Test the step measured temperature
         SStep=SStep+1;         % Counter for how many steps
         tsp(SStep)=t(n);

   uold(SStep)=T0(n-1); unew(SStep)=T0(n);

      end
 end


  qSt=0;
  if SStep > 0
for Step=1:SStep
    %---     G -> Evaluate the Green's function integration    ---%
HeatStep(Step)=G(t(n),tsp(Step),cb,uold(Step),unew(Step),beta,Gama,k,Rth,ro);
qSt=HeatStep(Step)+qSt;
end
  end

SkinTemp(n)=qSt;

          %------  Total analytical heat flux  -----%

qAnaly(n)=((T0(n)-Ta0)-(SkinTemp(n)+u1))/Rth;
```

```
          %-----------------------------------------%

          %----------  Calculating the error  -------%

err(n)=(Qm(n)-qAnaly(n)).^2;
ErrSum=err(n)+ErrSum;
 end
SDOR=sqrt(ErrSum/nmax);
          %----------   End of the time Loop   -------%
        %-------------------------------------------------%
```

Function for calculating the analytical temperature and heat flux:

```
function [qAnaly, SkinTemp] = FuncStepAnaly(
u1,T0,Ta0,t,beta,Gama,k,Rth,ro,cb,nmax )
       SStep=0;
 for n=1:nmax

if n>1
      if ( T0(n) ~= T0(n-1))    % Test the step measured temperature
        SStep=SStep+1;         % Counter for how many steps
        tsp(SStep)=t(n);

   uold(SStep)=T0(n-1); unew(SStep)=T0(n);

      end
 end

  qSt=0;
  if SStep > 0
for Step=1:SStep
    %---     G -> Evaluate the Green's function integration    ---%
HeatStep(Step)=G(t(n),tsp(Step),cb,uold(Step),unew(Step),beta,Gama,k,Rth,ro);
qSt=HeatStep(Step)+qSt;
end
  end

SkinTemp(n)=qSt;

          %------  Total analytical heat flux  -----%

qAnaly(n)=((T0(n)-Ta0)-(SkinTemp(n)+u1))/Rth;

end
          %----------   End of the time Loop   -------%
        %-------------------------------------------------%
```

Function for Zooming to provide new meshes for contact resistance and blood perfusion:

```
function [ R_min, R_max, W_min,W_max  ] = Meshing_PE( Rthmin,length_Rth,
wbmin,length_wb, factor1  )

   R_min=Rthmin-length_Rth;  W_min=wbmin-length_wb; % The minimum of the new
range
  % T1=Ta0min-length_Ta;
        if  W_min < 0       % Avoid having minimum blood perfusion
          W_min=wbmin-length_wb*factor1;
        end
        if  R_min < 0       % Avoid having minimum contact resistance
          R_min=Rthmin-length_Rth*factor1;
        end

   R_max=Rthmin+length_Rth;
   W_max=wbmin+length_wb;

end
```

Function to plot temperatures:

```
function PlotSolutionTemperature(nmax,Ta0,T0,SkinTemp,u1,t)

i=1:nmax;
plot(t(i),T0(i),'r',t(i),u1+SkinTemp(i)+Ta0,'b','linewidth',2);
  h = legend('Measured Temperature','Analy. skin Temp',2);
  set(h,'Interpreter','none')
  xlabel('time - sec','FontSize',14);
  ylabel('Measured Temperature','FontSize',14);
  title('Measured temperature distribution versus Anly temp','FontSize',12);
```

Function to plot heat flux:

```
function PlotSolutionHF(nmax,qTotal,t,Qm)
  jj=1:nmax-1;
  plot(t(jj),-qTotal(jj),'g',t(jj),-Qm(jj),'r','linewidth',2);
  h = legend('Analytical heat flux','Measured heat flux',2);
  set(h,'Interpreter','none')
  xlabel('time sec ','FontSize',14);
  ylabel('Heat Flux W/m2','FontSize',14);
  title('Analytical and Measured heat flux of the phantiom tissue','FontSize',12);
```

The Green's function:

```
function Temp = G(tn,tm,cb,uold,unew,beta,Gama,k,Rth,ro)
```

```
%realmax = 1.7977e+900;
ty1=(tn-tm);
a1=1/sqrt(Gama)/(-Gama+beta*k*k*Rth*Rth);
a2=k*Rth;
a3=a2*a2*sqrt(beta)*erf(sqrt(ty1*beta));
a4=erfcx(sqrt(ty1*Gama)/a2)*exp(-ty1*beta);
a5=a2*(-1+a4)*sqrt(Gama);

Temp=(1/cb/ro/Rth)*(unew-uold)*a1*(a3+a5);
```

Appendix C – Experiments

(C-1) - Instrumentation

1- Heat flux sensor

A combined temperature heat flux sensor was used to provide measurement data to the mathematical model. The sensitivity of the sensor plays major role in the satisfaction of the result. The sensor is very sensitive and accurate. The accuracy of the model might be increasing using multi array sensor to allow scanning wide area of the burn, instead of using three points sensor.

2- Data Acquisition

Data acquisition was used in this research is the USB-2416 which is configurable for voltage and thermocouples. The DAQ has 9 programmable input range from ∓ 0.078 V to ± 20 V, 24-bit resolution, and 8 digital I/O. For more technique detail, please visit Measurement Computing company website.
http://www.mccdaq.com/usb-data-acquisition/USB-2416.aspx?utm_campaign=bazaarvoice&utm_medium=Default&utm_source=RatingsAndReviews&utm_content=Default
(Accessed March 26, 2013) Figure C. 1 used under faire use.

Figure C. 1 USB-2416

(C-2)- Phantom Tissue Model

Phantom tissue was proved previously to simulate perfusion through tissue. The use of phantom tissue was helpful to minimize the use of animal and to test the reliability of thermal measurements in detecting different non-perfused layers. Different plastic layers were tested at three different flow rates to check the repeatability of the model.

(C-3)- The Pig Model

Based on the result from the phantom tissue, the model works perfectly in detecting the non-perfused layers. The medical significant of this research is to help doctor make the right decision to the third degree burn which requires skin grafting. As we proved from the phantom tissue results, we analysis thermal measurements which were done on two sides of two pigs to illustrate the ability of the model in detecting third degree burn and study behavior of blood perfusion and thermal resistance. The burn factor is also was developed in the first time to relate blood perfusion to thermal resistance.